Study on the Characteristics of Electrochemically Prepared Copper Oxide Photovoltaic Devices

(電気化学的に形成した酸化銅光電変換素子の特性に関する研究)

January, 2019

Doctor of Philosophy (Engineering)

Pei Loon Khoo

Toyohashi University of Technology

別紙４－１（課程博士（英文））

Date of Submission（month day，year）：　January 07, 2019

Department Mechanical Engineering	Student ID Number	D 145108	Supervisors	Masanobu Izaki
Applicant's name	Pei Loon Khoo			Seiji Yokoyama

Abstract（Doctor）

Title of Thesis	Study on the Characteristics of Electrochemically Prepared Copper Oxide Photovoltaic Devices（電気化学的に形成した酸化銅光電変換素子の特性に関する研究）

Approx. 800 words

Solar cells, or photovoltaics (PV), which converts light into electricity using semiconductor materials, are proving to be essential and indispensable for a sustainable society. Numerous kinds of solar cells have been the focus of research interest of late, and thin solid films of metal oxide (MO) semiconductors, such as copper oxide based photovoltaics (PV) has always been considered a material suitable for the realization of low-cost solar cells. Cuprous Oxide (Cu_2O) and Cupric Oxide (CuO) are stable forms of copper oxides, at the same time being intrinsically p-type semiconductors with 2.1 eV and 1.4 eV respectively. Attractive points of these oxides originate from their non-toxicity, abundance, and low cost. Also, one main aspect of interest to be noted is the preparation process, which can be achieved by electrochemical preparation. Electrochemically-prepared ZnO/Cu_2O PV had been reported to achieve 1.28%, however, the theoretical limit is approximately 20% according to the Shockley-Queisser Efficiency Limit, based on the bandgap energy. The main objective of this research is to further investigate the limiting factors of copper oxide based electrochemically-prepared photovoltaics and methods to further increase the PCE, based on close studies on the properties of its solid state physics.

In this thesis, in Chapter 1, the introduction, background, review, and purpose of this study are discussed. Latest climate researches are briefly concluded and the urgency of addressing global warming by switching to renewable energy, and the importance of solar energy is discussed. Metal Oxide (MO) PVs has the criteria of a high-potential candidate as cheap, and widespread. Among these MOs, Copper Oxides possess unique preferable properties such as ideal bandgap energies, at the same time being able to be fabricated by simple methods like the electrochemical preparation. It is then necessary to investigate the electrochemically-prepared copper oxides from its solid state physics. The definition of power conversion efficiency (PCE) is proportional to the short-circuit current density (J_{SC}) and open-circuit voltage (V_{OC}) of a PV. However, the independent variables of preparations are wide and complex, and insufficient information calls for the detailed study of determining the affecting factor during preparations. Also, a strategy using multiple bandgaps (using both copper oxide) as the light-absorbing layer is discussed.

In Chapter 2, we report the fabrication of basic Cu_2O-only (GZO/ZnO/Cu_2O) PV, and the successful increase in J_{SC} along with external quantum efficiency (EQE) and carrier mobility (μ), by annealing in vacuum using a rapid thermal annealer (RTA). The optimum annealing temperature was found to be 423 K. The effect of annealing during preparation is further

studied in detail, which includes its microstructural, optical and electrical properties. The mechanism is discussed, and the elucidation of the mechanism concludes a contributing factor of increased carrier mobility due to decreased scattering defects. Also, the relationship between the interface structure and V_{OC} is discussed.

In Chapter 3, we report the photovoltaic properties of CuO-only (CuO/Polysiloxane/GZO) successfully fabricated by electrodeposition from a basic aqueous solution containing copper acetate hydrate and ammonia with highly resistive polysiloxane layer insertion as the buffer layer. This study indicates the ability of CuO to function as a PV, which validates the strategy of using both Cu_2O and CuO as the light absorbing layer to increase the light-absorption width.

In Chapter 4, we report the fabrication of directly stacked (GZO/Cu_2O/CuO) photoactive layer prepared by electrodeposition and annealing. A decrease in EQE due to the formation of nanopores and voids was observed. However, the EQE was studied in detail and showed an expansion of absorption width which originates from the charge collection of both the Cu_2O and CuO layer, with a two-way carrier transport. When a low reverse biased voltage was applied, the charge collection corresponding to the absorption edge originating from the CuO layer could be clearly observed due to improved carrier control. However, there is a necessity for an in-depth investigation into the energy states and the band alignment of the Cu-oxide PV.

Chapter 5 reports on the study of chemical and energy states, along with the band alignment study of the copper oxides. X-ray photoelectron spectroscopy (XPS) evaluation was carried out in detail. Methods to accurately ascertain the type of oxides were explored which includes the Auger Parameter and the Wagner Plot. The band alignments were calculated based on the XPS results, and correspond to the results of the study in the previous chapter, explaining the two-way flow of carrier transport. An improved band alignment is proposed to further increase the PCE of the Cu-oxide PV.

In Chapter 6, the results obtained in this study are summarized. Limiting factors, such as scattering defects like grain boundaries and nanopores, the condition of heterointerfaces, crystal qualities, and semiconductor qualities were identified. However, the viability of multi-bandgap Copper-based PV is proved based on these results as a sound strategy to further increase the PCE. A proposal to realize further improvement is discussed. The experimental results obtained here will support further improvements in the electrochemically-prepared copper oxide based photoactive layers.

CONTENTS

CHAPTER 1: Introduction

CHAPTER 2: Fabrication of Basic Cu_2O-only (GZO/ZnO/Cu_2O) PV and the Effects of Annealing on the EQE and PV Performances

CHAPTER 3: Fabrication of Basic CuO PV with Polysiloxane as a Buffer Layer

CHAPTER 4: Characterization of Directly Stacked (GZO/Cu_2O/CuO) Prepared by Electrodeposition and Low-Temperature Annealing in Air

CHAPTER 5: The X-ray Photoelectron Spectroscopic Analysis and the Band Alignment Study of Directly Stacked Copper Oxide PV (GZO/Cu_2O/CuO)

CHAPTER 6: Summary

CHAPTER 1

Introduction

1.1 Introduction and Study Background

1.1.1 The Urgency of Global Warming and Solar Energy

The Intergovernmental Panel on Climate Change (IPCC), established by the United Nations Environment Program (UNEP) and the World Meteorological Organization (WMO)

reported that since the industrial revolution, the ocean has soaked up almost half of all man-made carbon dioxide (CO_2) emissions.[1] Shockingly, Galen McKinley *et al.* also suggested that the ocean's ability to absorb atmospheric CO_2 might be declining.[2] This first evidence of climate damping the ocean's ability to take up carbon from the atmosphere demonstrates the urgent need to cut down on the main man-made greenhouse gases.

The Paris Climate Agreement in 2015 by 175 Parties set a target of no more than 2 °C global warming above pre-industrial temperatures, and also an aspirational target of no more than 1.5 °C.[3] The threats and risks of global warming above 2 °C, like crop losses, water shortages, dangerous heatwaves[4], plants and animal extinctions[5], and flooding of many vulnerable near-to-sea-level cities[6], were highlighted with a note of urgency. This is further emphasized in a study reporting the unlikeliness of global warming lesser than 2 °C by the year 2100.[7]

The above reasons propel the need for us to more rapidly switch to renewable energies such as geothermal, bioenergy, hydropower, wind power, and solar energy. Most renewable energies have deployment limitations due to their nature of being location-dependent. Solar energy, on the other hand, is significantly less location-dependent, which is further evidenced by the emergence of floating solar farms such as the largest floating solar farm on a mine lake in Anhui province in China. Also, aside from geothermal energy, most renewable energy technically originates from the energy of the sun. For example, the crops used for bioenergy absorb energy from the sun, the rain that brings water to higher grounds used for hydropower comes from evaporation due to the sun, and the wind is produced by uneven heating of the Earth's surface by the sun. On top of that, these renewable energies consist of turbines to convert energies, which may lead to noise pollution and high maintenance costs. As such, it is arguably more efficient to directly harvest solar energy to cater to the need of civilization.

Many advances in recent years have shown progress towards harvesting more solar energy. In fact, it is plentiful and widely distributed. The average density of solar radiation is 100-300 W/m^2, and the solar energy potential is thought to be more than sufficient to meet current and projected energy uses well beyond 2100.[8] Photovoltaics (PV) or solar cells are semiconductor devices that contain light-absorbing layers, which converts photon directly into electron-hall pairs by excitation of electrons or other charge carriers to a higher-energy state. First applications of photovoltaics were to power satellites orbiting Earth and other spacecraft.

Huge advances can be seen in the efficiency and growth of solar energy especially in the last two decades, mainly through the development of photovoltaic devices (PV). The International Energy Agency (IEA) highlights the long-term global benefits of the development of affordable, inexhaustible and clean solar energy technologies. It will increase countries' energy security, enhance sustainability, reduce pollution, lower the costs of mitigating global warming, and keep fossil fuel prices lower than otherwise.[9]

There has been a very dramatic increase in the use of photovoltaic modules for grid-connected power generation. In 2016, China became the world's largest producer of photovoltaic power, overtaking Germany. The latest cumulative installed solar PV generation capacity in Gigawatts is shown in **Figure 1.1.1**. [10]

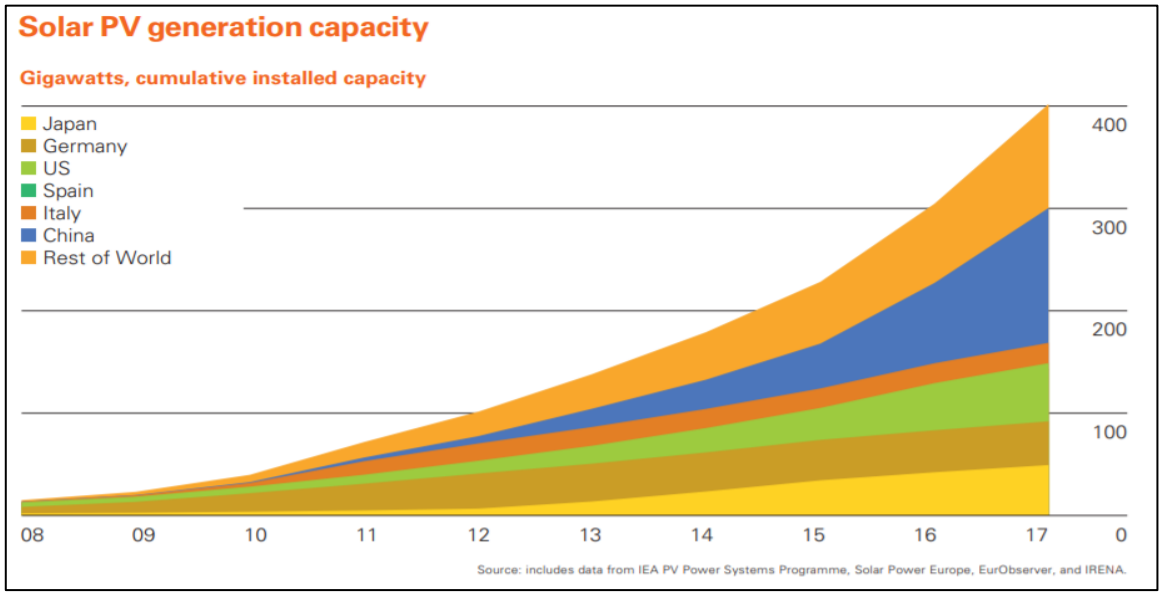

Figure 1.1.1 Top countries with cumulative installed capacity of PVs by Year.[10]

However, the potential of solar energy is still far from being optimized although it is proven to be the essential key to a sustainable society.

1.1.2 Metal Oxide Photovoltaics

Photovoltaic power generation uses solar panels, consisting a number of solar cells containing a photovoltaic material. The most common presently used photovoltaic materials include monocrystalline silicon, polycrystalline silicon, amorphous silicon, cadmium telluride (CdTe), and copper indium gallium selenide/sulfide (CIGS). In addition, there are many emerging PVs in recent years. PV performances of various kinds have been explored, and the improvements of best research-cells and the aggressive competition in recent years can be seen in **Figure 1.1.2**.[11]

However, it is known that even though the PV industry is booming, PV-generated electricity is still inferior to conventionally generated electricity in terms of cost and its dependence on subsidies, depending on the country.[12]

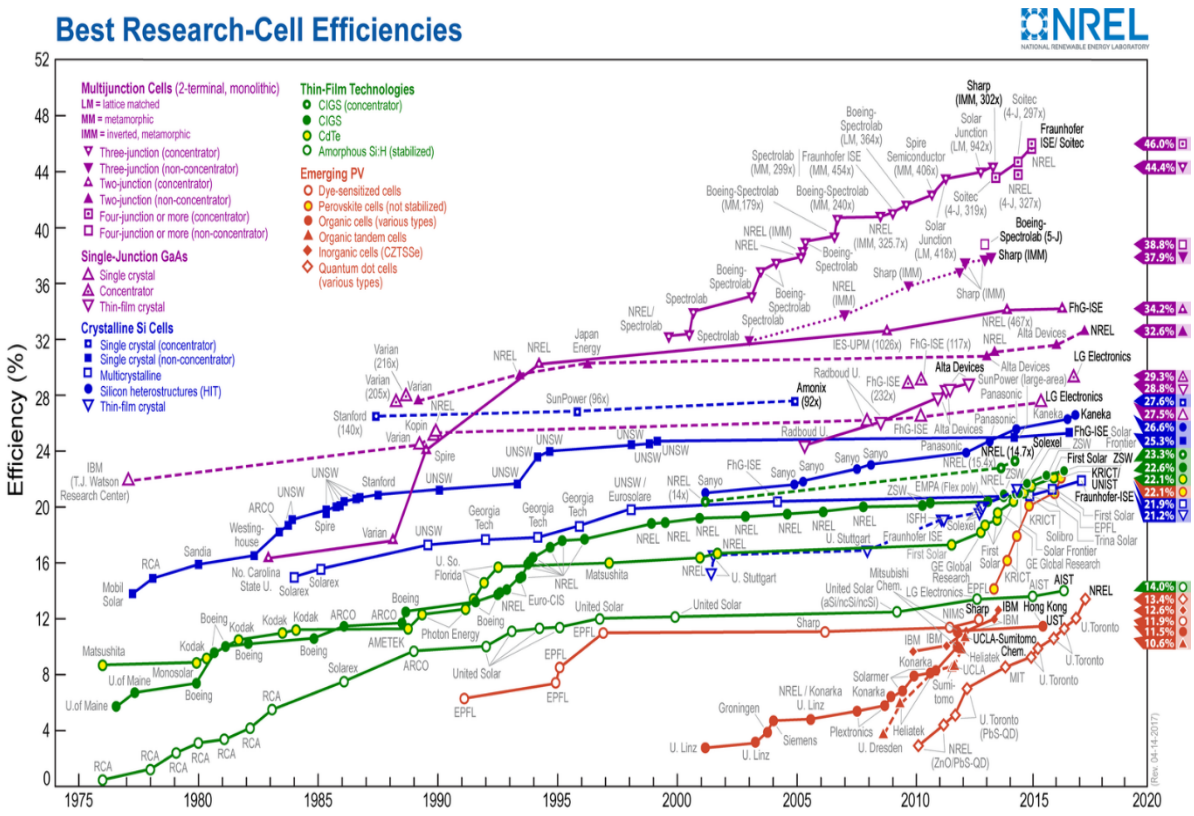

Figure 1.1.2 Best research-cell efficiencies for the past 40 years, reported by National Renewable Energy Laboratory (NREL).[11]

In Japan, the New Energy and Industrial Technology Development Organization (NEDO) presented a roadmap for technological development of PV power generation toward a PV system target of supplying 10% of the annual total electricity consumed in the country by 2030. The cumulative installed capacity was targeted at 54 GW by the year 2030 (PV2030).[13] A modified roadmap called PV2030^{+} with a goal to cover 5 to 10% of domestic primary energy demand with PV power generation by 2050 was also set by NEDO (NEDO website).[14]

One ultimate goal of designing an ideal PV is to reduce the costs of energy generation comparable to conventionally generated electricity, or called grid parity. Grid parity and further popularization in developing countries are achievable only if two key aspects of the PV systems are prioritized, which are the investigations on novel, cheaper (abundant) PV materials (material-wise) and a low-cost fabrication method (production-wise). The cost is usually accompanied by the strict requirement for fabricating high purity materials such as silicon and

GaAs, or the use of rare-earth elements, such as in the fabrication of CIGS. The presence of Indium is rare and expensive and can be easily depleted, which might affect the future of such PVs.

Recently, cadmium telluride (CdTe) thin-film photovoltaics has gained momentum in the PV market such as in South-Eastern countries. However, the high toxicity of the heavy metal cadmium is a serious environmental concern.[15,16] Chronic cadmium exposure produces a wide variety of acute and chronic effects in humans.[17,18] On top of that, cadmium is a rare-earth element, which means the supply is limited, consequently causing a higher price with higher demand in the future.

Organic-materials-based PV with high-efficiency solar cells with lower costs have also shown potentials, such as the halide perovskite solar cells[19] and dye-sensitized solar cells (DSSC) [20,21]. However, Organic-materials-based PVs have short life-spans as the nature of the materials, such as thermal instability[22] or issues of electrolyte-based instability[23].

As such, a particularly appealing new field of PV devices utilizing metal oxide (MO) semiconductors has emerged.[24] Thin film MO are generally chemically stable and can be manufactured in low-cost, ambient conditions. Being abundant, many metal oxides are also nontoxic, and a variety of them could be deposited electrochemically.

Furthermore, MO is already widely used today as components in PV cells and modules, for example, transparent conducting oxides (TCO). In fact, MO plays an important role in the TCO of most common PV devices aforementioned, like indium tin oxide (ITO), aluminum-doped zinc oxide (AZO), and fluorine-doped tin oxide (FTO). On top of that, promising next-generation PV cells such as extreme thin absorber cells (ETA)[25], quantum dot solar cells (QDSC)[26,27], and dye-sensitized solar cells (DSSC)[20,21] are based on MO electrodes.[24] In short, MO semiconductors are promising candidates for being environmentally friendly, stable and ultra-low-cost PV materials.

1.2 p-n Thin Film Copper Oxides PV

MO PV cells using Cu_2O, Co_3O_4, Fe_2O_3, and $BiFeO_3$ light-absorbing layers have been realized.[24,28,29] Among them, Copper Oxide based PV fabricated has achieved the most promising PV performance and was most researched.

There are two principal and stable forms of Copper Oxides. One is Copper (I) Oxide or Cuprous Oxide (Cu_2O) and another is Copper (II) Oxide or Cupric Oxide (CuO).

Cu_2O is described as brownish-red, or yellow when the film is thin. It is also an intrinsically p-type semiconductor, due to the possession of Cu vacancies and O interstitials.[30,31] Other than the general properties of being terrestrial abundant and low-toxic, it has a bandgap energy of 2.1 eV, with the approximate corresponding light-absorption edge at 650 nm. CuO is described as blackish in color. It is also a p-type semiconductor with several reported bandgap energies from 1.32 to 1.56 eV [32–34], with a corresponding light-absorption edge above 800 nm. By combining with suitable n-type semiconductors such as n-ZnO, these materials can form photovoltaics.

Copper Oxide photovoltaics has a long history. In fact, one of the first copper oxide solar cell was described in 1917, when Kennard *et al.* reported the change of the surface potential of a plate of Cuprous Oxide by about 25 mV under illumination.[35] However, focus on silicon and germanium PVs since their discoveries in the 1950s caused a decline in attention for the Copper Oxide PVs. However, only recently Copper Oxide PVs have gained increasing attention and breakthroughs. The Cu_2O layer can be fabricated by various physical and chemical methods such as thermal oxidation[36–38], Atomic Layer Deposition (ALD) [39,40], Pulsed Laser Deposition (PLD)[41,42], electron beam evaporation[43], metal organic chemical vapor deposition (MOCVD)[44,45], sputtering[46–49], successive ionic layer adsorption and reaction

(SILAR)[50,51], and activated reactive evaporation[52]. **Figure 1.2.1** shows the classification of these methods.

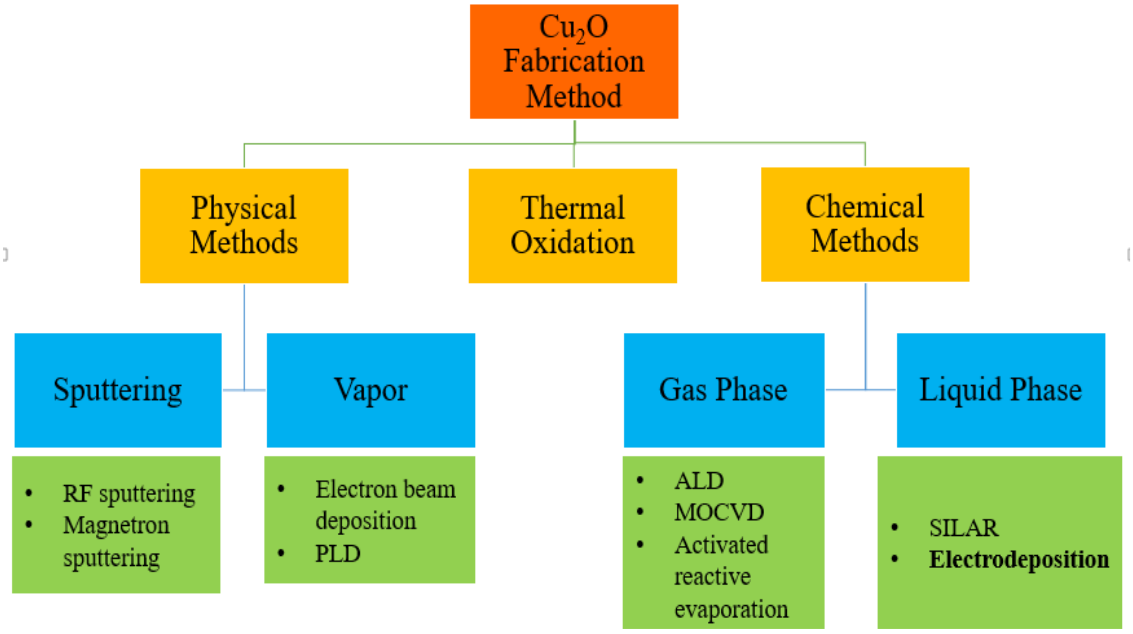

Figure 1.2.1 Classification of fabrication method categorized into thermal, physical and chemical methods.

For all of the fabrication methods shown here, except for the liquid phase chemical methods, sophisticated and special equipment are used, which often leads to difficulty in scalability of fabrication, and a higher cost. Also, the majority of these methods uses high vacuum or gas chambers, besides requiring specific precursors and expensive targets to fabricate the Cu_2O. Additionally, complications arise when techniques such as RF sputtering lead to the inclusion of CuO and Cu_2O simultaneously[53].

Regarding the Cu_2O PVs, many have taken the approach of constructing a p-n heterojunction structure with other n-type transparent conducting oxide (TCO) such as ZnO. One reason is that other types of PV such as metal-Cu_2O Schottky solar cells[54] cannot be much improved. Again, various methods such as PLD[36], ALD[38,55] and sputtering were being deployed to fabricate the heteroepitaxial n-semiconductor (window layer) of the PV. Similar to the fabrication of the light-absorbing p-Cu_2O mentioned earlier, energy-intensive

methods of fabrication should be minimized or avoided for realizing an ultra-low-cost PV. Comparatively, all-liquid-phase-chemical methods only require simple and low-cost experiment setups, at the same time easy to scale-up. While SILAR is an emerging technique used for fabrication of Cu_2O, electrodeposition is already quite established as a method to fabricate thin film metal oxides.

As discussed in the previous section, the two important aspects of the condition of an ultra-low-cost copper oxide PV are the material and fabrication method. Ievskaya *et al.* discussed the advantage of n-ZnO/p-Cu_2O PV fabrication in atmospheric conditions using ALD.[38] But in comparison, fabrication of PVs in atmospheric conditions electrochemically requires lesser energy in terms of machinery and equipment, and thus cheaper. Thus, we maintained the favorable fabrication method of electrochemical deposition and low-temperature annealing in our research, which is overwhelmingly cost-effective compared to other methods which either involve very-high-temperatures during oxidation of copper sheets (usually more than 1273 K) or high-vacuum condition during deposition or when forming the p-n heterojunction. We do however propose facile, low-temperature treatment/fabrication techniques as an attempt to improve the overall performance, as will be discussed later on.

1.2.1 Solid-state Physics for Improvements in Copper Oxide PV

To build a strategy to further increase the performance of the copper oxide based PV, fundamental review from the solid-state physics of this kind of photovoltaic mechanism is necessary.

The energy alignment of a p-n junction is as follows in **Figure 1.2.1.1.** E_c and E_v are conduction and valence band levels respectively, E_g the bandgap energy and E_f the Fermi level. P-type semiconductors are characterized by having deficiencies of valence electrons, or holes, and is the light-absorbing layer in a PV. The Fermi level is closer to E_v in such semiconductors.

N-type semiconductors have an excess of negative electron charge carriers. At thermal equilibrium, a space charge region forms when electrons and holes in the vicinity of the junction diffuse and recombine with each other. This leads to the formation of a space-charge region without any mobile charge carriers, shown in the diagram, which is also called the depletion region. At thermal equilibrium, the Fermi levels align, and there is no net current flowing.

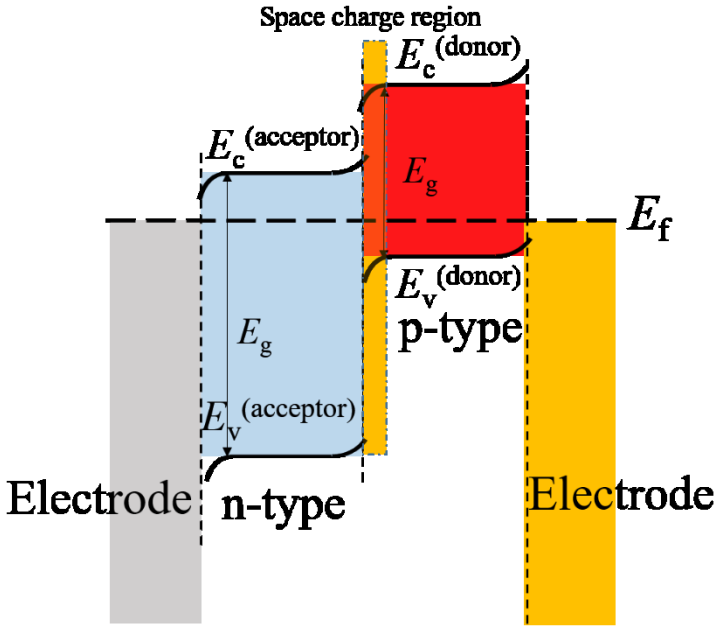

Figure 1.2.1.1 Energy band diagram for a p-n junction PV

When light as photons reach the light-absorbing layer (p-type semiconductor), part of the light is absorbed. Sunlight that reaches Earth consists of a wide span of wavelengths, including infrared (700 nm and above), visible light (400 to 700 nm) and ultraviolet (10 to 400 nm). The spectral irradiance similar to the standard AM 1.5G (sun at 45° above the horizon) is shown in **Figure 1.2.1.2**[56], with high irradiance especially from around 300 to 1000 nm. The portion of absorption at each wavelength corresponds to the properties of the material inclusive of its bandgap energy.

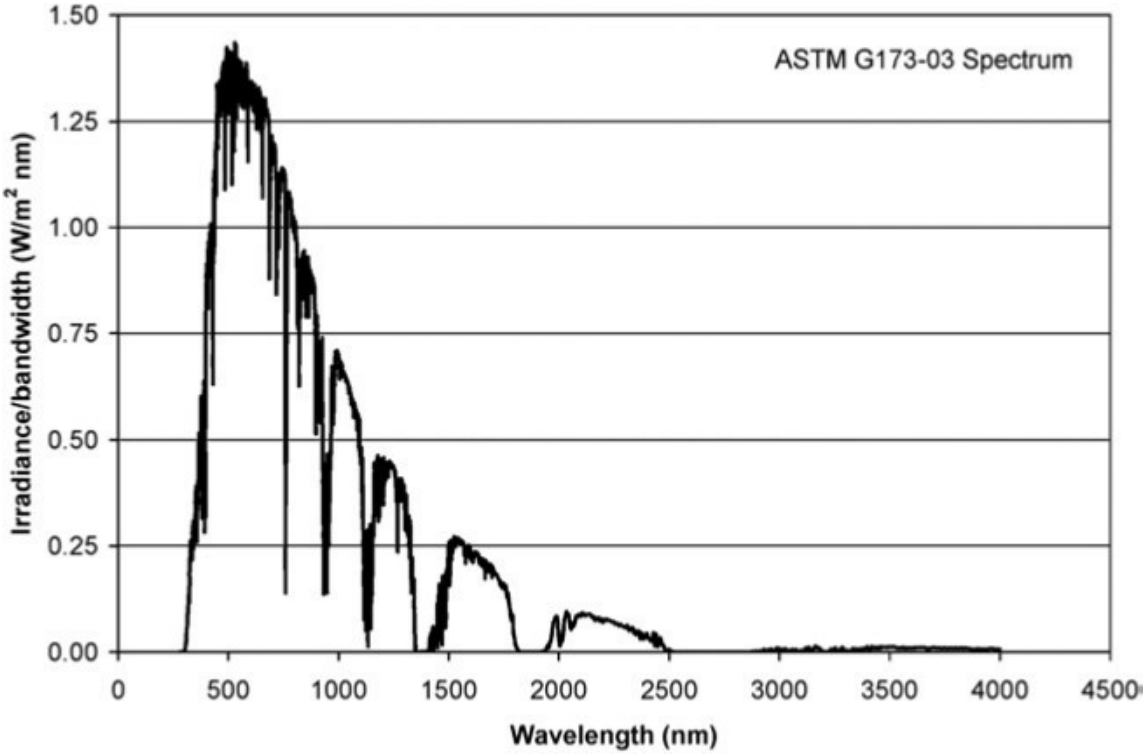

Figure 1.2.1.2 The ASTM G173-03 standard spectral irradiance, close to AM 1.5G irradiance of sunlight used for PV evaluation.

When the wavelength of the photon that was absorbed has energy higher than the bandgap of the light-absorbing layer, electrons from the valence band will be excited to the conduction band, leaving a hole at the valence band. This process of separation of electron-hole pairs and causing charge carriers to be free is known as the photovoltaic effect. Electrons move towards cathode and holes move towards anode in opposite directions, generating electricity, which can be evaluated by the I-V measurement. The charge carriers are transported by drift and diffusion

and are collected at metallic contact electrodes at either side of the p-n junction. Usually, anodic contact electrodes with high work function and close to the valence band of the p-semiconductor are used, while cathodic contact with a work function close to the conduction band of the n-semiconductor is preferable.

However, there are several complications. Recombination may occur when free electrons and holes recombine with each other as not all photoexcited carriers can be collected. Also, charge transport via diffusion can be affected by defects like impurities and scattering defects in the light-absorbing material. These are important aspects that should be considered in order to design an ideal PV.

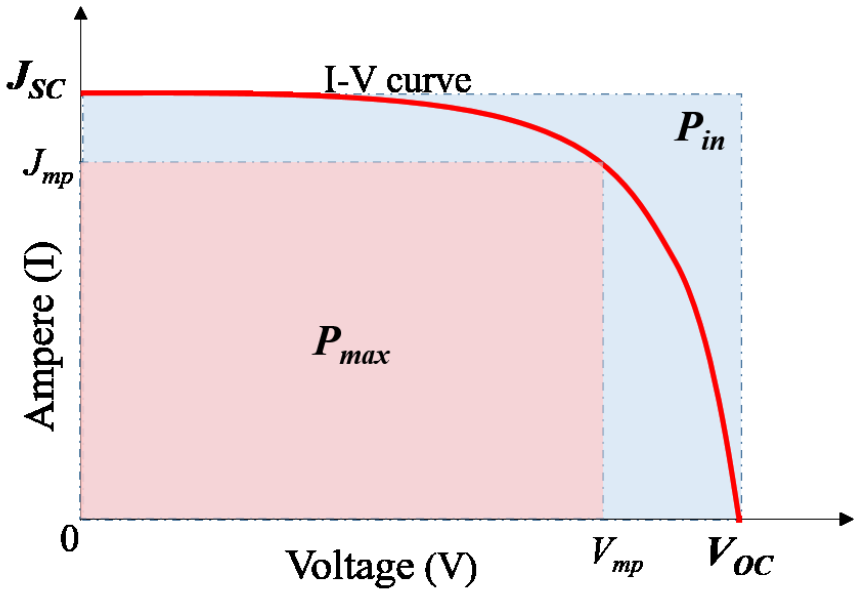

Figure 1.2.1.3. A typical I-V curve of a photovoltaic device.

Power conversion efficiency (PCE) of the p-n PV is evaluated and calculated by the I-V measurement. A typical I-V curve of a PV is shown in **Figure 1.2.1.3**. Here, the I-V curve intersects at 0 V and 0 A at the x- and y-axes, denoted as the short-circuit current (J_{SC}) and the open-circuit voltage (V_{OC}). PCE (η) is well known and generally defined as the following equation,

$$\eta = \frac{P_{max}}{P_{in}} = \frac{J_{mp}V_{mp}}{P_{in}} = \frac{J_{SC}V_{OC}FF}{P_{in}} \quad \textbf{(1.2.1)}$$

where J_{mp} and V_{mp} are values which when multiplied obtains the maximum power, P_{max}. FF is fill factor and P_{in} is the input power. Also, FF can be expressed in terms of V_{OC} as follows[57],

$$FF = \frac{V_{OC} - ln(V_{OC}+0.72)}{V_{OC}+1} \quad \textbf{(1.2.2)}$$

As such, we know that the J_{SC} and V_{OC} are important factors in improving the PCE of a photovoltaic since they are proportional in relationships.

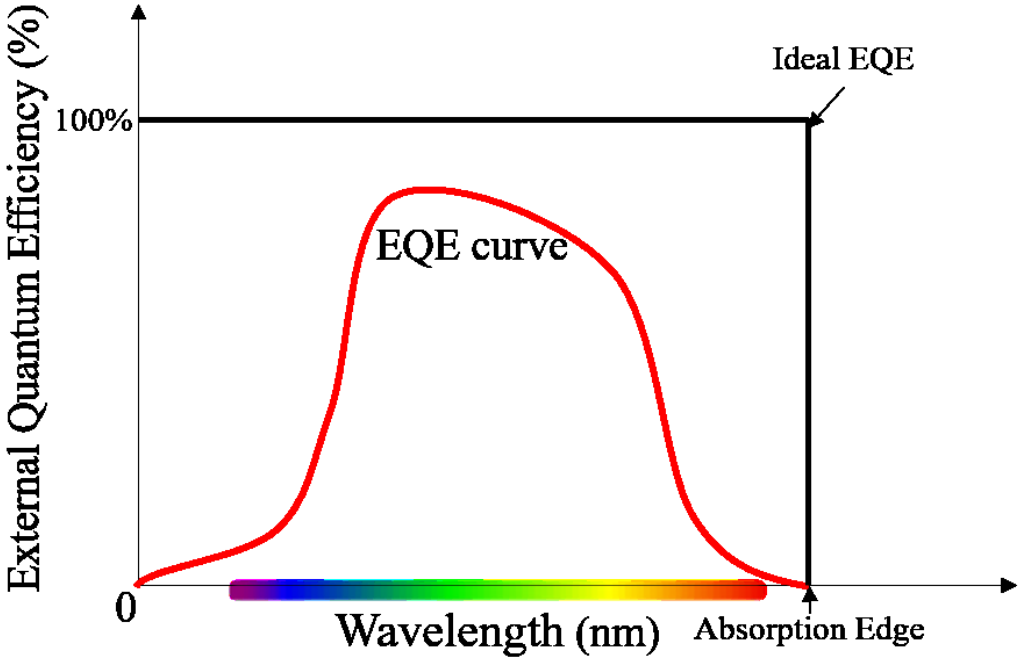

Figure 1.2.1.4. A typical EQE curve of a photovoltaic device.

Another important evaluation for photovoltaics is the external quantum efficiency (EQE). Quantum efficiency is the ratio of the number of carriers generated by the PV to the number of photons of a given energy incident on the PV. A typical EQE measurement is shown in **Figure 1.2.1.4.** An ideal curve would have 100% EQE starting from the absorption edge corresponding to the bandgap energy of the material. However, this is not possible due to several practical reasons such as charge recombination, scattered carriers, reduced absorption at long wavelengths due to low penetration depth, and low diffusion length. Since the number of

carriers collected is related to the current density of a PV, the relationship between EQE and short-circuit current can be express as[58],

$$EQE = \frac{1240}{\lambda} \times \frac{J_\lambda}{E_\lambda} \times 100 \quad \textbf{(1.2.3)}$$

where E_λ(W cm^{-2}) is the intensity of the monochromatic light and J_λ is short-circuit current density at a given monochromated light irradiation with a wavelength of λ. In other words, since EQE refers to the number of electron-hole pairs successfully collected per incident photon, it evaluates the combined efficiency of light absorption, charge transport, and charge collection. A closer measured EQE curve to the ideal EQE is preferable, which would mean a high ratio of charge collection per incident photon.

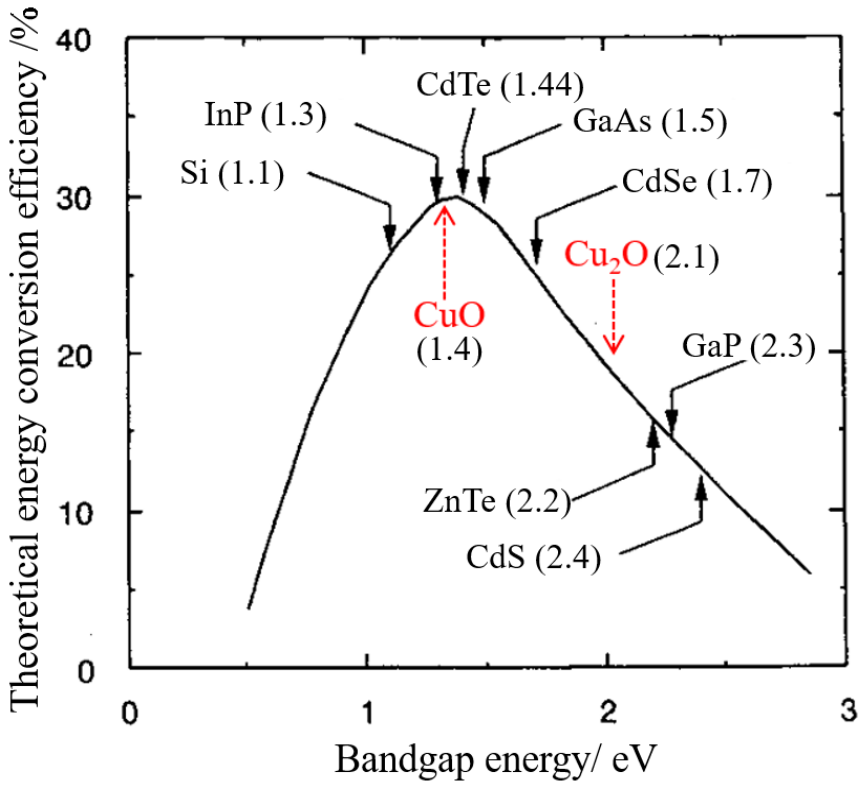

Figure 1.2.1.5 Theoretical Shockley-Queisser limit of single heterojunction PV according to bandgap energy.

In 1960, Shockley *et al.* described the detailed balance limit of efficiency of p-n junction solar cells.[59] The upper theoretical limit was then known to highly dependable on the light

absorbing layer's bandgap energy.[60] The relationship between the bandgap energy and maximum theoretical power conversion efficiency (PCE) of PVs with a single heterojunction is shown **Figure 1.2.1.5.** From this figure, both copper oxides are at favorable positions near the peak of the curve, with maximum theoretical PCE of 30% and 20% for CuO and Cu_2O respectively. This indicates the promising potential these copper oxides possess.

The current records for Cu_2O PVs are PCE of 8.1% by thermal preparation[61], and 1.28% by electrodeposition reported by Izaki *et al.*[62]. Little research regarding CuO photovoltaics has been published, with very poor PCE values[63,64]. The reasons for the low PCE are not known presently. One may argue that CuO has a preferable bandgap energy compared to Cu_2O since a low bandgap is desirable and that a single-bandgap CuO PV is sufficient. While this might be true theoretically, this is not the case practically. One single bandgap solar cell cannot properly match the broad solar spectrum. Photons with energy lesser than the bandgap are not absorbed, and photons with energy larger than the bandgap generate electron-hole pairs which immediately lose almost all energy in excess of the bandgap energy[65], leading to a high thermal energy loss consequently. Additionally, the relationship between bandgap energy E_g and open-circuit voltage V_{OC}, as shown in the following equation[66],

$$qV_{OC} \cong E_g \eta_C + \mathrm{k}T_c ln\left\{\left(\frac{\Omega_S}{\Omega_o}\right)\left(\frac{T_S}{T_c}\right)\left(\frac{\alpha_{S1}}{\alpha_{c1}}\right)\right\} \quad \textbf{(1.3)}$$

where k is Boltzmann's constant, q is the electronic charge, T_S and T_c are the sun (6000 K) and the cell (300 K) temperatures, respectively. η_C is the Carnot efficiency and α_{S1}, α_{c1} are correction terms.[67–69] And since the E_g and V_{OC} are directly related, E_g can be considered as the upper limit to the extractable voltage from the cell.[70,71] As such, a single, low bandgap light-absorbing layer would have a lower maximum achievable V_{OC}.

Thus, some solar cells utilize a strategy to harvest multiple portions of the solar spectrum which can overcome the solar cell limits by having different bandgap energies as the light-

absorbing layers. The multi-junction solar cell,[56,72,73] which contains two or more p-n junctions made of different semiconductor materials produce electric current in response to different wavelengths of light due to different bandgap energies. Another example is the quantum dot solar cell,[27] which possesses tunable bandgap energies by varying particle size and shape, and can even make infrared energy accessible[74]. Such a strategy of multiple bandgaps incorporation might be applicable for the copper oxide photovoltaic as well, which will be further discussed.

1.3 Strategy to Improve the Copper Oxide Based PV from EQE

From the fundamental understanding of the solid-state physics thus far, the respective factors can be improved by optimizing the fabrication process of the copper oxide based PV, in order to achieve the ultimate improvement in PCE. From the EQE, an overall improvement of the PV can be attempted in two ways:

1. Increase the overall values of the EQE curve.

2. Increase the absorption wavelength span, which means extending the absorption edge towards longer wavelength.

The first way can be achieved by attempting to improve the light-absorbing layer by lessening the defects and improve the electrical properties, which may lead to an improvement in charge collection. As such, morphology and microstructural characterization is important which might give insights to the quality of the light-absorbing layer, along with characterization of the electrical properties. In short, exploring ways to lessen defects and improve the semiconductor quality is the strategy to increase the overall values of the EQE. For Cu_2O, annealing is a common way to improve the layer quality for the Cu_2O. However, the extent of improvements and mechanism should be elucidated. For CuO, a large surface irregularity can occur corresponding to the increase in the heterointerface due to its morphology, and lessening the surface irregularity can improve the layer quality.

The second way can be attempted by utilizing both copper oxides, Cu_2O and CuO, with different bandgap energies. The corresponding absorption edge for Cu_2O with a 2.1 eV bandgap energy is approximately 650 nm, while a CuO layer with 1.45 eV is approximately 850 nm. As discussed earlier, combining both copper oxides with different bandgap energies is a good strategy to harvest a different portion of the sunlight spectrum. This may extend the absorption edge and subsequently increase the EQE. In fact, the strategy of having different bandgaps has been deployed in PVs to overcome the theoretical PCE such as CIGS[75,76] and quantum dots PV[27,58]. Since Cu_2O and CuO have a eutectic system, it has been demonstrated by Izaki *et*

al. that by oxidizing the topmost Cu_2O layer by annealing in air in low temperature, a directly stacked Cu_2O/CuO layer can be fabricated with a clear boundary, while retaining lattice relationship.[77] This method will allow a combination of both copper oxides as the light-absorbing layer. At the same time, when combining different light-absorbing materials, a proper investigation is needed with respect to the band alignment. Band alignment can give insight to the band offsets and charge transport mechanism[78–81], and an optimum band alignment can be proposed based on its study. This calls for an investigation for the band alignment of the combined copper oxides PV.

1.4 Research Objective

External quantum efficiency (EQE) is of high importance since it reflects on the overall photovoltaic performance in terms of absorption span of the solar spectrum and charge collection. To improve the EQE performance of the copper oxide based photovoltaics, this thesis explored methods to increase the EQE of the copper oxide PVs, in order contribute to improving the performance of copper oxide PVs as an excellent ultra-low cost Metal Oxide PV as the next-generation photovoltaics. Single Cu_2O-only PV was investigated, followed by CuO-only PV, and then directly stacked Cu_2O/CuO. The energy state of the PV was also investigated to facilitate the understanding of the copper oxide based PV. As such, the research objectives of this thesis are as follows,

- To investigate the fabrication of the Cu_2O-only PV (GZO/ZnO/Cu_2O) by electrodeposition and elucidate the effects of annealing on the microstructural, electrical and EQE properties.

- To investigate the fabrication of the CuO-only PV (CuO/Polysiloxane/GZO) by electrodeposition and IV evaluation to determine the possibility of CuO as a light absorbing layer.

- To investigate the fabrication of directly stacked copper oxides (GZO/Cu_2O/CuO) photoactive layer prepared by electrodeposition and annealing, and their EQE properties as the absorbing layer.

- To investigate the band alignment of the directly stacked copper oxide photoactive layer by XPS characterization to propose an improved band alignment

The overall objective of this thesis is to investigate methods of improving the EQE and subsequently give insights and proposals to further improve the overall performance of the copper oxide based photovoltaics and photoactive layer.

1.5 Outline of This Study

In this thesis, we study the fabrication of copper oxides (Cu_2O, CuO, and Cu_2O/CuO) photovoltaics and photoactive layer and investigate methods to increase the metal oxide PV performances, implied from its solid-state physics. The study from the fabrication of simple Cu_2O PVs by electrodeposition, then CuO PVs by electrodeposition and finally Cu_2O/CuO photoactive layer by annealing electrodeposited Cu_2O layer in air. At the same time of exploring the methods to increase the copper oxide based PV performances, this thesis studies and identifies the limiting factors and problems, which will prove useful in future advances for such ultra-low cost metal oxide thin film PVs.

Chapter 2 covers fabrication of ZnO/Cu_2O PV on transparent soda lime glass/Ga:ZnO substrate by electrodeposition. The electrodeposited devices were then annealed in RTA in different temperatures ranging from 423 K to 573 K in vacuum. The morphology and structure of the as-deposited and annealed ZnO/Cu_2O PV were characterized by field emission scanning electron microscope observation (FE-SEM) and X-ray Diffraction Pattern (XRD). The optical properties were investigated by ultraviolet-visible spectroscopy (Uv-vis), and the electrical properties were evaluated by Hall measurement, current-voltage measurement (I-V) and the external quantum efficiency (EQE). Cu_2O functions as the light-absorbing layer as expected, and an optimum increase of the maximum value of EQE to nearly 100% was achieved around 410 nm after annealing at 423 K, and the mechanism is discussed. The increase in EQE was also related to a successful improvement in PEC in terms of J_{SC}.

Chapter 3 discusses the fabrication of CuO/Polysiloxane/GZO PV on Au coated Si wafer substrate. Electrodeposition was used to fabricate the CuO and the polysiloxane layer was prepared by spin coating. Infrared spectra were recorded along with the observation of FE-SEM and I-V evaluation. PV characteristics such as $V_{OC,}$ $J_{SC,}$ and *FF* were obtained at 0.24 V, 0.067 μA cm^{-2} and 0.29 respectively and this demonstrated that CuO successfully acted as the light-

absorbing layer, although showing room for improvements. The particularly high V_{OC} was attributed the Polysiloxane buffer layer.

Chapter 4 describes the study of directly stacked copper oxides (GZO/Cu_2O/CuO) photoactive layer prepared by electrodeposition, followed by annealing in air. Similar characterization was carried out such as the investigation of the morphology and structure of the as-deposited GZO/Cu_2O and annealed GZO/Cu_2O/CuO by field emission scanning electron microscope observation (FE-SEM) and X-ray Diffraction Pattern (XRD). The optical properties were investigated by ultraviolet-visible spectroscopy (Uv-vis), followed by the external quantum efficiency (EQE). EQE of samples prepared at 523 K was further investigated under different low reversed biased voltages were also investigated to explain the directly stacked Cu_2O/CuO behavior. An extended absorption edge was achieved from 650 nm that of a Cu_2O layer to 850 nm of a CuO layer with both layers acting as the light absorbing layers under bias voltage at 523 K.

Chapter 5 describes the detailed X-ray photoelectron spectroscopy (XPS) examination of the Cu_2O-only and the directly stacked Cu_2O/CuO layer prepared under different conditions (temperatures). Characterization techniques including Auger Parameter and the Wagner Plot were deployed and the comparison to reported values of CuO and Cu_2O were made. A band diagram is drawn according to the XPS measurement and the optical bandgap calculated, and the behavior of the EQE shown in the previous chapter is explained. An improved bandgap is proposed based on the results.

And finally, **Chapter 6** summarizes the results obtained and concludes this thesis.

REFERENCES

[1] K.L. Denman, G. Brasseur, A. Chidthaisong, P. Ciais, P.M. Cox, R.E. Dickinson, D. Hauglustaine, C. Heinze, E. Holland, D. Jacob, U. Lohmann, S. Ramachandran, P.L. da S. Dias, S.C. Wofsy, X. Zhang, Chapter 7 - Couplings between changes in the climate system and biogeochemistry, Clim. Chang. 2007 Phys. Sci. Basis. (2007).

[2] G.A. McKinley, A.R. Fay, T. Takahashi, N. Metzl, Convergence of atmospheric and North Atlantic carbon dioxide trends on multidecadal timescales, Nat. Geosci. 4 (2011) 606–610. doi:10.1038/ngeo1193.

[3] UNFCCC, Paris Agreement, United Nations Framew. Conv. Clim. Chang. (2016). doi:FCCC/CP/2015/L.9.

[4] T.N. Palmer, Climate extremes and the role of dynamics, Proc. Natl. Acad. Sci. 110 (2013) 5281–5282. doi:10.1073/pnas.1303295110.

[5] A.E. Cahill, M.E. Aiello-Lammens, M.C. Fisher-Reid, X. Hua, C.J. Karanewsky, H. Yeong Ryu, G.C. Sbeglia, F. Spagnolo, J.B. Waldron, O. Warsi, J.J. Wiens, How does climate change cause extinction?, Proc. R. Soc. B Biol. Sci. 280 (2012) 20121890–20121890. doi:10.1098/rspb.2012.1890.

[6] P.P. Wong, I.J. Losada, J.P. Gattuso, J. Hinkel, A. Khattabi, K.L. McInnes, Y. Saito, A. Sallenger, R.J. Nicholls, F. Santos, S. Amez, Coastal Systems and Low-Lying Areas, in: C.B. Field, V.R. Barros, D.J. Dokken, K.J. Mach, M.D. Mastrandrea (Eds.), Clim. Chang. 2014 Impacts, Adapt. Vulnerability, Cambridge University Press, Cambridge, 2015: pp. 361–410. doi:10.1017/CBO9781107415379.010.

[7] A.E. Raftery, A. Zimmer, D.M.W. Frierson, R. Startz, P. Liu, Less than 2 °C warming by 2100 unlikely, Nat. Clim. Chang. 7 (2017) 637–641. doi:10.1038/nclimate3352.

[8] W.C. Turkenburg, J. Beurskens, A. Faaij, P. Fraenkel, I. Fridleifsson, E. Lysen, D. David Mills, J.R. Moreira, L. J. Nilsson, A. Schaap, W. C. Sinke, Renewable Energy Technologies, in: D.. Communications Development Incorporated, Washington (Ed.),

World Energy Assess. Energy Chall. Sustain., September, United Nations Development Programme Bureau for Development Policy, United States of America, 2000: pp. 219–267.

[9] C. Philibert, Solar Energy Perspectives, OECD, 2011. doi:10.1787/9789264124585-en.

[10] Bp, BP Statistical Review of World Energy 2018, 2018. https://www.bp.com/content/dam/bp/en/corporate/pdf/energy-economics/statistical-review/bp-stats-review-2018-renewable-energy.pdf.

[11] NREL, Best Research-Cell Efficiencies, 2018. doi:https://www.nrel.gov/pv/assets/pdfs/pv-efficiencies-07-17-2018.pdf.

[12] K. Branker, M.J.M. Pathak, J.M. Pearce, A review of solar photovoltaic levelized cost of electricity, Renew. Sustain. Energy Rev. 15 (2011) 4470–4482. doi:10.1016/j.rser.2011.07.104.

[13] P.J. Reddy, Solar Power Generation: Technology, New Concepts & Policy, CRC Press, 2012. https://books.google.com/books?id=9mTGmlbwyvQC&pgis=1.

[14] NEDO, PV2030+ Abstract, (2008). https://www.nedo.go.jp/content/100080327.pdf.

[15] T. Inaba, E. Kobayashi, Y. Suwazono, M. Uetani, M. Oishi, H. Nakagawa, K. Nogawa, Estimation of cumulative cadmium intake causing Itai-itai disease, Toxicol. Lett. 159 (2005) 192–201. doi:10.1016/j.toxlet.2005.05.011.

[16] H. Baba, K. Tsuneyama, M. Yazaki, K. Nagata, T. Minamisaka, T. Tsuda, K. Nomoto, S. Hayashi, S. Miwa, T. Nakajima, Y. Nakanishi, K. Aoshima, J. Imura, The liver in itai-itai disease (chronic cadmium poisoning): Pathological features and metallothionein expression, Mod. Pathol. 26 (2013) 1228–1234. doi:10.1038/modpathol.2013.62.

[17] J. Pan, J.A. Plant, N. Voulvoulis, C.J. Oates, C. Ihlenfeld, Cadmium levels in Europe: implications for human health., Environ. Geochem. Health. 32 (2010) 1–12. doi:10.1007/s10653-009-9273-2.

[18] G. Bertin, D. Averbeck, Cadmium: cellular effects, modifications of biomolecules, modulation of DNA repair and genotoxic consequences (a review), Biochimie. 88 (2006) 1549–1559. doi:10.1016/j.biochi.2006.10.001.

[19] J.S. Manser, J.A. Christians, P. V. Kamat, Intriguing Optoelectronic Properties of Metal Halide Perovskites, Chem. Rev. 116 (2016) 12956–13008. doi:10.1021/acs.chemrev.6b00136.

[20] A. Hagfeldt, G. Boschloo, L. Sun, L. Kloo, H. Pettersson, Dye-sensitized solar cells., Chem. Rev. (2010). doi:10.1002/chem.201101923.

[21] R. Ameta, S. Benjamin, S. Sharma, M. Trivedi, Dye-sensitized solar cells, in: Sol. Energy Convers. Storage Photochem. Modes, 2015. doi:10.1201/b19148.

[22] G. Divitini, S. Cacovich, F. Matteocci, L. Cinà, A. Di Carlo, C. Ducati, In situ observation of heat-induced degradation of perovskite solar cells, Nat. Energy. 1 (2016) 15012. doi:10.1038/NENERGY.2015.12.

[23] S.K. Pathak, A. Abate, T. Leijtens, D.J. Hollman, J. Teuscher, L. Pazos, P. Docampo, U. Steiner, H.J. Snaith, Towards long-term photostability of solid-state dye sensitized solar cells, Adv. Energy Mater. 4 (2014). doi:10.1002/aenm.201301667.

[24] S. Rühle, A.Y. Anderson, H.-N. Barad, B. Kupfer, Y. Bouhadana, E. Rosh-Hodesh, A. Zaban, All-Oxide Photovoltaics, J. Phys. Chem. Lett. 3 (2012) 3755–3764. doi:10.1021/jz3017039.

[25] T. Dittrich, A. Belaidi, A. Ennaoui, Concepts of inorganic solid-state nanostructured solar cells, Sol. Energy Mater. Sol. Cells. (2011). doi:10.1016/j.solmat.2010.12.034.

[26] S. Rühle, M. Shalom, A. Zaban, Quantum-dot-sensitized solar cells, ChemPhysChem. (2010). doi:10.1002/cphc.201000069.

[27] P. V Kamat, Quantum Dot Solar Cells. The Next Big Thing in Photovoltaics. doi:10.1021/jz400052e.

[28] S.Y. Yang, L.W. Martin, S.J. Byrnes, T.E. Conry, S.R. Basu, D. Paran, L. Reichertz, J. Ihlefeld, C. Adamo, A. Melville, Y.H. Chu, C.H. Yang, J.L. Musfeldt, D.G. Schlom, J.W. Ager, R. Ramesh, Photovoltaic effects in BiFeO3, Appl. Phys. Lett. (2009). doi:10.1063/1.3204695.

[29] T. Choi, S. Lee, Y.J. Choi, V. Kiryukhin, S.W. Cheong, Switchable ferroelectric diode and photovoltaic effect in BiFeO3, Science (80-.). (2009). doi:10.1126/science.1168636.

[30] H. Raebiger, S. Lany, A. Zunger, Origins of the p-type nature and cation deficiency in Cu_2O and related materials, Phys. Rev. B - Condens. Matter Mater. Phys. 76 (2007) 045209. doi:10.1103/PhysRevB.76.045209.

[31] M. Nolan, S.D. Elliott, The p-type conduction mechanism in Cu_2O: a first principles study, Phys. Chem. Chem. Phys. 8 (2006) 5350. doi:10.1039/b611969g.

[32] F.P. Koffyberg, F.A. Benko, A photoelectrochemical determination of the position of the conduction and valence band edges of p-type CuO, J. Appl. Phys. 53 (1982) 1173–1177. doi:10.1063/1.330567.

[33] K. Nakaoka, J. Ueyama, K. Ogura, Photoelectrochemical Behavior of Electrodeposited CuO and Cu_2O Thin Films on Conducting Substrates, J. Electrochem. Soc. 151 (2004) C661. doi:10.1149/1.1789155.

[34] L. Wang, K. Han, M. Tao, Effect of Substrate Etching on Electrical Properties of Electrochemically Deposited CuO, J. Electrochem. Soc. 154 (2007) D91. doi:10.1149/1.2404913.

[35] E.H. Kennard, E.O. Dieterich., An Effect of Light upon the Contact Potential of Selenium and Cuprous Oxide, Phys. Rev. 9 (1917) 58–63. doi:10.1103/PhysRev.9.58.

[36] T. Minami, Y. Nishi, T. Miyata, Heterojunction solar cell with 6% efficiency based on an n-type aluminum-gallium-oxide thin film and p-type sodium-doped Cu_2O sheet, Appl. Phys. Express. 8 (2015) 022301. doi:10.7567/APEX.8.022301.

[37] T. Minami, Y. Nishi, T. Miyata, High-Efficiency Cu_2O-Based Heterojunction Solar Cells Fabricated Using a Ga_2O_3 Thin Film as N-Type Layer, Appl. Phys. Express. 6 (2013) 044101. doi:10.7567/APEX.6.044101.

[38] Y. Ievskaya, R.L.Z. Hoye, A. Sadhanala, K.P. Musselman, J.L. MacManus-Driscoll, Fabrication of ZnO/Cu_2O heterojunctions in atmospheric conditions: Improved interface quality and solar cell performance, Sol. Energy Mater. Sol. Cells. 135 (2015) 43–48. doi:10.1016/j.solmat.2014.09.018.

[39] S.W. Lee, Y.S. Lee, J. Heo, S.C. Siah, D. Chua, R.E. Brandt, S.B. Kim, J.P. Mailoa, T. Buonassisi, R.G. Gordon, Improved Cu_2O-based solar cells using atomic layer deposition to control the Cu oxidation state at the p-n junction, Adv. Energy Mater. 4 (2014). doi:10.1002/aenm.201301916.

[40] T. Waechtler, N. Roth, R. Mothes, S. Schulze, E. Stefan, Copper Oxide ALD from a Cu(I) Beta-Diketonate: Detailed Growth Studies on SiO2 and TaN, ECS Trans. 25 (2009) 277–287. doi:10.1149/1.3205062.

[41] S.H. Wee, P.S. Huang, J.K. Lee, A. Goyal, Heteroepitaxial Cu_2O thin film solar cell on metallic substrates, Sci. Rep. 5 (2015). doi:10.1038/srep16272.

[42] C.R. Iordanescu, D. Tenciu, I.D. Feraru, A. Kiss, M. Bercu, D. Savastru, R. Notonier, C.E.A. Grigorescu, Structure and morphology of Cu-oxides films derived from PLD processes, Dig. J. Nanomater. Biostructures. 6 (2011) 863–868.

[43] C.L. Kuo, R.C. Wang, J.L. Huang, C.P. Liu, C.K. Wang, S.P. Chang, W.H. Chu, C.H. Wang, C.H. Tu, The synthesis and electrical characterization of Cu2O/Al:ZnO radial p-n junction nanowire arrays, Nanotechnology. 20 (2009). doi:10.1088/0957-4484/20/36/365603.

[44] S. Jeong, E.S. Aydil, Heteroepitaxial growth of Cu_2O thin film on ZnO by metal organic chemical vapor deposition, J. Cryst. Growth. 311 (2009) 4188–4192. doi:10.1016/j.jcrysgro.2009.07.020.

[45] S. Jeong, S.H. Song, K. Nagaich, S.A. Campbell, E.S. Aydil, An analysis of temperature dependent current–voltage characteristics of Cu_2O–ZnO heterojunction solar cells, Thin Solid Films. 519 (2011) 6613–6619. doi:10.1016/j.tsf.2011.04.241.

[46] Y.S. Lee, J. Heo, M.T. Winkler, S.C. Siah, S.B. Kim, R.G. Gordon, T. Buonassisi, Nitrogen-doped cuprous oxide as a p-type hole-transporting layer in thin-film solar cells, J. Mater. Chem. A. 1 (2013) 15416–15422. doi:10.1039/c3ta13208k.

[47] S. Noda, H. Shima, H. Akinaga, Cu2O/ZnO heterojunction solar cells fabricated by magnetron-sputter deposition method films using sintered ceramics targets, in: J. Phys. Conf. Ser., 2013. doi:10.1088/1742-6596/433/1/012027.

[48] K. Akimoto, S. Ishizuka, M. Yanagita, Y. Nawa, G.K. Paul, T. Sakurai, Thin film deposition of Cu_2O and application for solar cells, Sol. Energy. (2006). doi:10.1016/j.solener.2005.10.012.

[49] J. Gan, V. Venkatachalapathy, B.G. Svensson, E. V. Monakhov, Influence of target power on properties of CuxO thin films prepared by reactive radio frequency magnetron sputtering, in: Thin Solid Films, 2015: pp. 250–255. doi:10.1016/j.tsf.2015.05.029.

[50] A.T. Ravichandran, K. Dhanabalan, A. Vasuhi, R. Chandramohan, S. Mantha, Morphology, bandgap, and grain size tailoring in Cu_2O thin film by SILAR method, IEEE Trans. Nanotechnol. 14 (2015) 108–112. doi:10.1109/TNANO.2014.2369438.

[51] S. Chatterjee, S.K. Saha, A.J. Pal, Formation of all-oxide solar cells in atmospheric condition based on Cu_2O thin-films grown through SILAR technique, Sol. Energy Mater. Sol. Cells. 147 (2016) 17–26. doi:10.1016/j.solmat.2015.11.045.

[52] B. Balamurugan, B.R. Mehta, Optical and structural properties of nanocrystalline copper oxide thin films prepared by activated reactive evaporation, Thin Solid Films. 396 (2001) 90–96. doi:10.1016/S0040-6090(01)01216-0.

[53] A.A. Ogwu, E. Bouquerel, O. Ademosu, S. Moh, E. Crossan, F. Placido, An investigation of the surface energy and optical transmittance of copper oxide thin films prepared by reactive magnetron sputtering, Acta Mater. 53 (2005) 5151–5159. doi:10.1016/j.actamat.2005.07.035.

[54] L.C. Olsen, R.C. Bohara, M.W. Urie, Explanation for low-efficiency Cu_2O Schottky-barrier solar cells, Appl. Phys. Lett. 34 (1979) 47–49. doi:10.1063/1.90593.

[55] J. Kaur, O. Bethge, R.A. Wibowo, N. Bansal, M. Bauch, R. Hamid, E. Bertagnolli, T. Dimopoulos, All-oxide solar cells based on electrodeposited Cu_2O absorber and atomic layer deposited ZnMgO on precious-metal-free electrode, Sol. Energy Mater. Sol. Cells. 161 (2017) 449–459. doi:10.1016/j.solmat.2016.12.017.

[56] H. Cotal, C. Fetzer, J. Boisvert, G. Kinsey, R. King, P. Hebert, H. Yoon, N. Karam, III–V multijunction solar cells for concentrating photovoltaics, Energy Environ. Sci. 2 (2009) 174–192. doi:10.1039/B809257E.

[57] M.A. Green, Solar cell fill factors: General graph and empirical expressions, Solid State Electron. 24 (1981) 788–789. doi:10.1016/0038-1101(81)90062-9.

[58] I. Robel, V. Subramanian, M. Kuno, P. V. Kamat, Quantum Dot Solar Cells. Harvesting Light Energy with CdSe Nanocrystals Molecularly Linked to Mesoscopic TiO 2 Films, J. Am. Chem. Soc. 128 (2006) 2385–2393. doi:10.1021/ja056494n.

[59] W. Shockley, H.J. Queisser, Detailed balance limit of efficiency of p-n junction solar cells, J. Appl. Phys. 32 (1961) 510–519. doi:10.1063/1.1736034.

[60] S. Rühle, Tabulated values of the Shockley-Queisser limit for single junction solar cells, Sol. Energy. 130 (2016) 139–147. doi:10.1016/j.solener.2016.02.015.

[61] T. Minami, Y. Nishi, T. Miyata, Efficiency enhancement using a Zn1-xGex-O thin film as an n-type window layer in Cu_2O-based heterojunction solar cells, Appl. Phys. Express. 9 (2016). doi:10.7567/APEX.9.052301.

[62] M. Izaki, T. Shinagawa, K.-T. Mizuno, Y. Ida, M. Inaba, A. Tasaka, Electrochemically constructed p-Cu 2 O/n-ZnO heterojunction diode for photovoltaic device, J. Phys. D. Appl. Phys. 40 (2007) 3326–3329. doi:10.1088/0022-3727/40/11/010.

[63] R. Motoyoshi, T. Oku, H. Kidowaki, A. Suzuki, K. Kikuchi, S. Kikuchi, B. Jeyadevan, Structure and photovoltaic activity of cupric oxide-based thin film solar cells, J. Ceram. Soc. Japan. 118 (2010) 1021–1023. doi:10.2109/jcersj2.118.1021.

[64] H. Kidowaki, T. Oku, T. Akiyama, Fabrication and characterization of CuO/ZnO solar cells, J. Phys. Conf. Ser. 352 (2012) 012022. doi:10.1088/1742-6596/352/1/012022.

[65] C.H. Henry, Limiting efficiencies of ideal single and multiple energy gap terrestrial solar cells, J. Appl. Phys. 51 (1980) 4494–4500. doi:10.1063/1.328272.

[66] A. Niv, Z.R. Abrams, M. Gharghi, C. Gladden, X. Zhang, Overcoming the bandgap limitation on solar cell materials, Appl. Phys. Lett. 100 (2012). doi:10.1063/1.3682101.

[67] Z.R. Abrams, A. Niv, X. Zhang, Solar energy enhancement using down-converting particles: A rigorous approach, J. Appl. Phys. 109 (2011). doi:10.1063/1.3592297.

[68] T. Markvart, Solar cell as a heat engine: Energy-entropy analysis of photovoltaic conversion, Phys. Status Solidi Appl. Mater. Sci. 205 (2008) 2752–2756. doi:10.1002/pssa.200880460.

[69] W. Ruppel, P. Würfel, Upper Limit for the Conversion of Solar Energy, IEEE Trans. Electron Devices. 27 (1980) 877–882. doi:10.1109/T-ED.1980.19950.

[70] M.A. Green, Limits on the Open-Circuit Voltage and Efficiency of Silicon Solar Cells Imposed by Intrinsic Auger Processes, IEEE Trans. Electron Devices. 31 (1984) 671–678. doi:10.1109/T-ED.1984.21588.

[71] G.L. Araújo, A. Martí, Absolute limiting efficiencies for photovoltaic energy conversion, Sol. Energy Mater. Sol. Cells. 33 (1994) 213–240. doi:10.1016/0927-0248(94)90209-7.

[72] M. Yamaguchi, T. Takamoto, K. Araki, Super high-efficiency multi-junction and concentrator solar cells, Sol. Energy Mater. Sol. Cells. 90 (2006) 3068–3077. doi:10.1016/j.solmat.2006.06.028.

[73] R.R. King, D.C. Law, K.M. Edmondson, C.M. Fetzer, G.S. Kinsey, H. Yoon, R.A. Sherif, N.H. Karam, 40% efficient metamorphic GaInPGaInAsGe multijunction solar cells, Appl. Phys. Lett. 90 (2007). doi:10.1063/1.2734507.

[74] E.H. Sargent, Infrared quantum dots, Adv. Mater. 17 (2005) 515–522. doi:10.1002/adma.200401552.

[75] P. Jackson, D. Hariskos, E. Lotter, S. Paetel, R. Wuerz, R. Menner, W. Wischmann, M. Powalla, New world record efficiency for Cu(In,Ga)Se2 thin-film solar cells beyond 20%, Prog. Photovoltaics Res. Appl. 19 (2011) 894–897. doi:10.1002/pip.1078.

[76] M.A. Contreras, L.M. Mansfield, B. Egaas, J. Li, M. Romero, R. Noufi, E. Rudiger-Voigt, W. Mannstadt, Wide bandgap Cu(In,Ga)Se2solar cells with improved energy conversion efficiency, Prog. Photovoltaics Res. Appl. 20 (2012) 843–850. doi:10.1002/pip.2244.

[77] M. Izaki, K. Fukuzawa, Photovoltaic layer and the preparation process, 2017–54917, n.d.

[78] M. Yang, L. Zhu, Y. Li, L. Cao, Y. Guo, Asymmetric interface band alignments of Cu_2O/ZnO and ZnO/Cu 2O heterojunctions, J. Alloys Compd. (2013). doi:10.1016/j.jallcom.2013.05.033.

[79] S. Siol, J.C. Hellmann, S.D. Tilley, M. Graetzel, J. Morasch, J. Deuermeier, W. Jaegermann, A. Klein, Band Alignment Engineering at Cu_2O/ZnO Heterointerfaces, ACS Appl. Mater. Interfaces. 8 (2016) 21824–21831. doi:10.1021/acsami.6b07325.

[80] H. Wei, H. Gong, Y. Wang, X. Hu, L. Chen, H. Xu, P. Liu, B. Cao, Three kinds of Cu_2O/ZnO heterostructure solar cells fabricated with electrochemical deposition and their structure-related photovoltaic properties, CrystEngComm. 13 (2011) 6065–6070. doi:10.1039/c1ce05540b.

[81] Z. Kang, X. Yan, Y. Wang, Z. Bai, Y. Liu, Z. Zhang, P. Lin, X. Zhang, H. Yuan, X. Zhang, Y. Zhang, Electronic Structure Engineering of Cu 2 O Film/ZnO Nanorods Array All-Oxide p-n Heterostructure for Enhanced Photoelectrochemical Property and Self-powered Biosensing Application, Sci. Rep. 5 (2015). doi:10.1038/srep07882.

CHAPTER 2

Fabrication of basic Cu_2O-only (GZO/ZnO/Cu_2O) PV and the Effects of Annealing on the EQE and PV Performances

2.1 Introduction

2.1.1 Electrodeposition of Cu_2O and ZnO

Electrodeposition is a major synthetic tool for the production of a large variety of inorganic materials, such as oxides, hydroxides, phosphates, chalcogenides, as well as metals and metal alloys.[1,2] Not only does it offer ease of thickness and morphology control, but it is also feasible of large-scale, low-cost production.[3]

Early electrodeposition of Cu_2O from an alkaline bath was first developed by Stareck et al. in 1943[4], and the photovoltaic properties further studied in 1986 by Rakhshani et al.[5] Cu_2O can be electrodeposited from alkaline electrolyte which contains cupric ions.[6,7] Lactate is one of stabilizing agent to form soluble copper lactate complex in the electrolyte, and the predominant complex is $Cu(II)Lac_2$[8], and the formation of Cu_2O takes place in a two-step process given by the following reactions, [9]

$$Cu(II)Lac_2 + e^- \leftrightarrow Cu(I)Lac + Lac^-$$

$$2Cu(I)Lac + 2OH^- \leftrightarrow Cu_2O + H_2O + 2Lac^-$$

And electrodeposition of Cu_2O can also be carried out in weak acid without reduction to copper metal if OH^- ion from dissolved oxygen is present.[10]

In 1995, the first preparation of transparent ZnO films with characteristic optical band gap energy of 3.3 eV by electrodeposition from aqueous electrolyte was reported by Izaki *et al.*[11] And a subsequent successful heteroepitaxial electrodeposition of ZnO/Cu_2O forming a photovoltaic device by the same group has achieved 1.28% in PCE.[7] Not only did this strongly demonstrate the room for improvement for the electrodeposited Cu_2O-based PV, but it also prompted the need for a clear understanding of the factors limiting the cell performance fabricated by electrodeposition.

2.1.2 Annealing

The effects on annealing have been known to improve the qualities of a layer, and annealing in air/vacuum on the Cu_2O layers with varying results have been reported. Mahalingam *et al.* reported that the best result was obtained when sample prepared by electrodeposition at pH 9 solution was annealed in air at 623 K with the highest increase in peak height of (200) cubic phase and increase in grain size to 100 nm. [12] Liang *et al.* reported that the best photoelectrochemical current obtained was from Cu_2O film electrodeposited at pH

9 with 60 minutes of annealing at 623 K in Ar atmosphere.[13] Dimopoulos *et al.* reported that the best result was obtained when the sample prepared by electrodeposition at pH 12.5 was annealed in vacuum at 573 K, with highest open-circuit voltage (V_{OC} = 0.51 V), short-circuit current (J_{SC} = 4.67 mA cm^{-2}), and conversion efficiency (η =1.12%) respectively, but with linear I-V characteristics appearing when annealed at 623 K.[14] Hsieh *et al.* reported that the best result was obtained when the sample was prepared by DC-reactive magnetron sputtering at 473 K were annealed at 823 K with 1.2% oxygen added in the protective annealing atmosphere, possessing the lowest resistivity, but the rectifying effect of P-N junction disappeared.[15] Despite the similarity in positive results achievable after annealing, there is a discrepancy regarding the optimum temperature. Also, discussions about the disappearance of the rectifying effect after optimum annealing conditions were lacking. So the mechanisms and origin of the effects and improvements by annealing on photovoltaic devices were still obscure and the explanation insufficient. Little effort has been done to investigate the importance in microstructural change which offers insight and direct evidence to the changes of the light-absorbing Cu_2O-layer and the phase transitions when annealed.

In a previous study by Shinagawa *et al.*, significant improvements in the photoelectric performances were achieved in Cu_2O-only layer after annealing.[16] This chapter applies the similar concept in the constructed ZnO/Cu_2O device, and focus on the most important aspects of improvements while paying attention to the microstructural changes when annealed in vacuum, which offer further explanations to the discrepancy between mentioned reports, and further insight into the mechanism of annealing.

2.2 Experimental Procedures

2.2.1 Preparation of ZnO/Cu_2O PVs

ZnO was electrodeposited on conductive gallium-doped zinc oxide (GZO)-coated glass substrate. Prior to the electrodeposition, the GZO substrate was rinsed with acetone, degreased in 0.1 mol L^{-1} NaOH and rinsed with deionized water. ZnO was then deposited potentiostatically at −0.8 V referenced to an Ag/AgCl electrode in saturated KCl, [11] at an electric charge of 0.02 C cm^{-2} with a potentiostat (Hokuto Denko, HAL-3001), connected to a Coulomb meter (Hokuto Denko, HF-301) in an aqueous solution of 8 mmol L^{-1} zinc nitrate hexahydrate ($Zn(NO_3)_2 \cdot 6H_2O$, Nacalai Tesque, Inc.) at 336 K. A Pt plate was used as the counter electrode. Cu_2O was then electrodeposited on the ZnO layer from an alkaline aqueous solution (pH = 12.5) containing 0.4 mol L^{-1} copper (II) acetate monohydrate ($Cu(CH_3COO)_2 \cdot$ H2O, Nacalai Tesque, Inc.) and 3 mol L^{-1} lactic acid (Kanto Chemical, Co., Inc.). The pH was adjusted with NaOH. This electrodeposition was carried out at −0.4 V and at an electric charge of 1.7 C cm^{-2} at 313 K without stirring. All aqueous solutions used here were prepared with deionized water purified by an Elix-UV system (Millipore). The schematics of the structure of PV is shown in **Figure 2.2.1**.

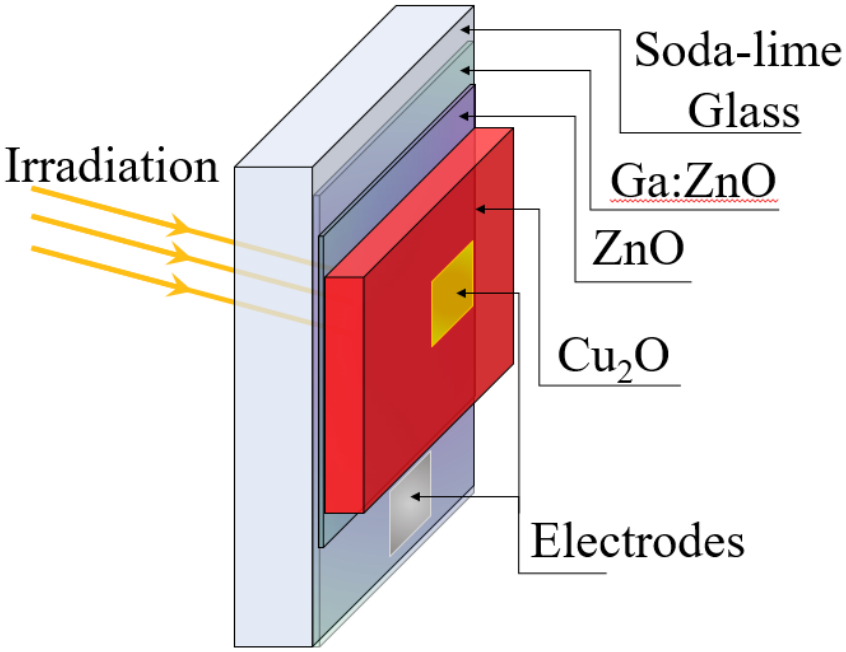

Figure 2.2.1. Schematics of the electrodeposited GZO/ZnO/Cu_2O PV.

2.2.2 Annealing of ZnO/Cu_2O PVs

Annealing of the obtained GZO/ZnO/Cu_2O samples was carried at varying temperatures of 423, 473, 523, and 573 K for 60 minutes using a Rapid Thermal Anneal (RTA) furnace (MILA 5000) at a rate of temperature increase of 10 K s^{-1} under vacuum (~10^{-3} Pa). After annealing, the samples were left to cool down to room temperature before being exposed to air.

2.2.3 Characterization of ZnO/Cu_2O PVs

The external quantum efficiency measurement was performed on the ZnO/Cu_2O PVs using a monochromator (Bunko Keiki, SM-250KB, with approximate monochromatic light intensity above 5 mW cm^{-2}). Active areas of the PV devices were defined by the area of 9 mm^2 Au electrodes deposited by thermal vapor deposition on the Cu_2O layers. The current density-voltage curves under AM1.5 illumination with 100 mW cm^{-2} power were recorded using a solar simulator (Bunko Keiki, OTENTOSUN-III) with a Keithley 2400 source meter. Structural characterizations were carried out by X-ray Diffractometer (XRD, Rigaku RINT 2500) operated at 20 kV and 10 mA using Cu Kα radiation. Observation of surface and cross-sectional morphology was carried out with a field emission scanning electron microscope (FE-SEM, Hitachi High Technology SU8000). Optical absorption spectra were recorded using a UV-Vis-NIR spectrophotometer (Hitachi High-Technology UV-4100) with an integrating sphere. The absorption coefficient was derived from an assumed constant film thickness at 2.5 μm observed via FE-SEM and transmittance spectra measured with an integrating sphere setup, with the horizontal axis as photon energy to estimate band gap energy of the Cu_2O. Electrical properties including resistivity, carrier density, and carrier mobility were evaluated by using a Hall Effect measurement system (Toyo Technica ResiTest 8310) using the van der Pauw method, [17] at room temperature under an applied magnetic field of 0.3 T in alternating current mode. For the Hall Effect measurements, Cu_2O was electrodeposited on a GZO substrate and annealed at the same condition as mentioned above. Then, the Cu_2O was transferred to an insulation resin using a mechanical splitting method. [18]

2.4 Results and Discussion

Thin-film ZnO/Cu_2O PVs were constructed electrochemically on GZO substrates and RTA annealed at 423, 473, 523, and 573 K under vacuum (~10^{-4} Pa) for 1 h. To define the active cell area, Au electrode (9 mm^2) was then thermally evaporated on the Cu_2O surface, and the photovoltaic performance was evaluated in terms of external quantum efficiency (EQE) and current-voltage curves.

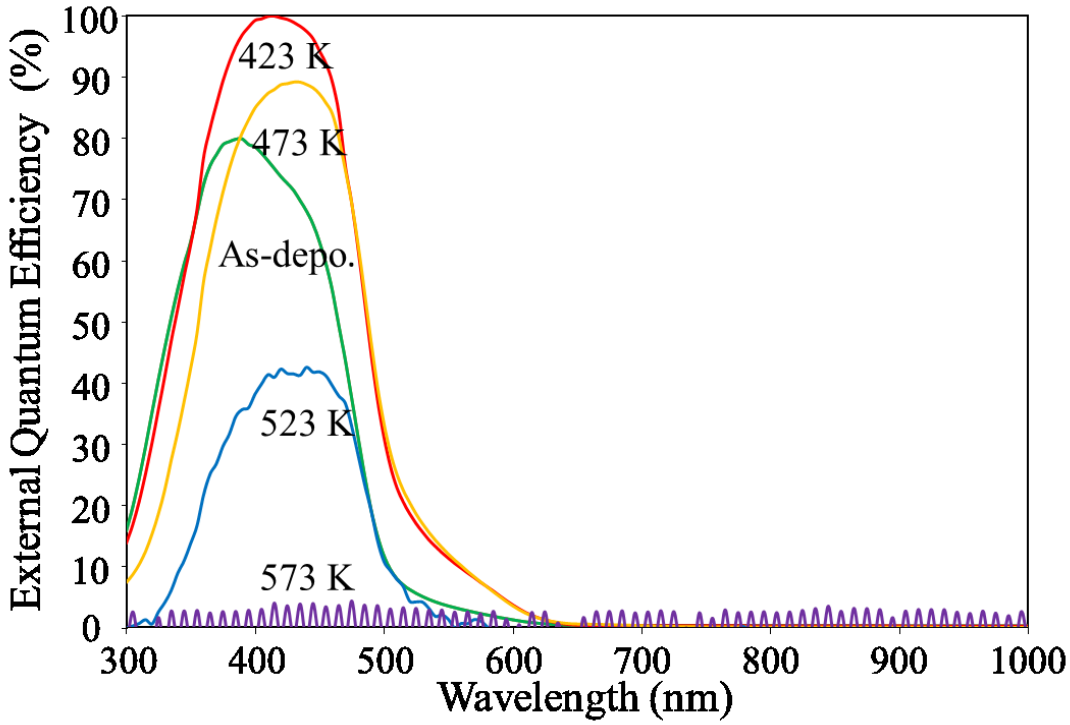

Figure 2.1. External quantum efficiency spectra of ZnO/Cu_2O PVs as-deposited and annealed at 423, 473, 523, and 573 K.

Figure 2.1 shows the EQE spectra of the obtained ZnO/Cu_2O PVs. The spectra generally display gradual inclines at around 650 nm and a steep incline at approximately 500 nm, unique to the absorption edge of Cu_2O, evidencing that the Cu_2O layers indeed act as the light-absorbing layer, and charge was collected. The maximum EQE values for the samples as-

deposited and annealed at 423, 473, and 523 K are 79.9%, 99.9%, 89.2%, and 42.5%, at wavelengths of 390 nm, 415 nm, 430 nm, and 440 nm respectively. The broadening of the EQE

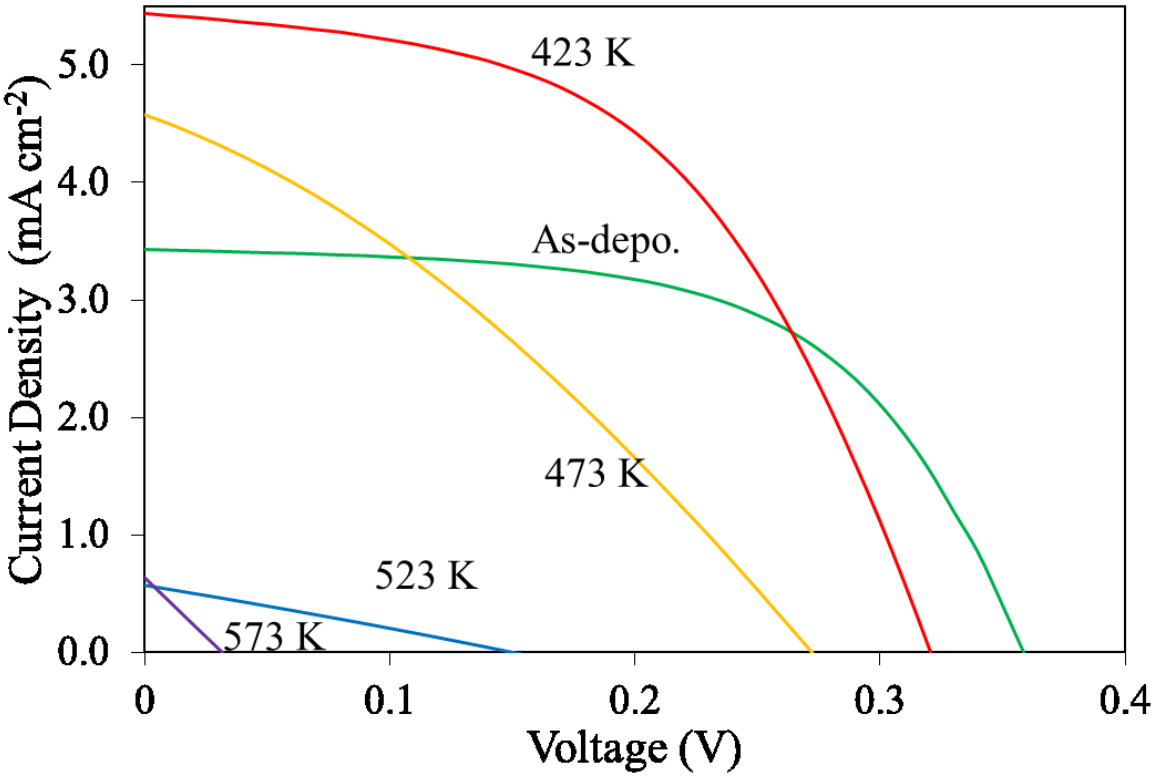

Figure 2.2. *J–V* curves under irradiation (AM 1.5G, 100W cm^{-2}) of ZnO/Cu_2O PVs as-deposited and annealed at 423, 473, 523, and 573 K.

spectrum at wavelengths above 380 nm was observed and that the maximum EQE increases for nearly 20% after annealing at 423 K. The maximum EQE is still 10% higher for the sample annealed at 473 K as compared to the as-deposited sample although the EQE at wavelengths below 390 nm decreases. The EQE spectrum deteriorate when annealed at 523 K and above; the measurement could not be made at 573 K. Assuming that the optical depth for wavelengths below 465 nm in the Cu_2O is less than few hundred nanometers,[19] the dramatic increase in EQE after annealing at 423 K to nearly 100% at the wavelength of 415 nm indicates that the charge collection was improved significantly in the Cu_2O layer near the heterointerface. On the other hand, the lowered EQE spectra at 523 K shows poor charge collection, which is speculated to be caused by charge recombination.

Figure 2.2 shows the *J-V* measurement for the same samples measured for EQE in **Figure 2.1**, and the results are summarized in **Table 2.1**. Compared to the as-deposited sample, RTA annealing at 423 K increases short-circuit current density, J_{sc} by approximately 1.6 times. Samples RTA annealed at temperatures more than 523 K shows deteriorated J_{sc}, which display a corresponding trend as the EQE evaluation in Figure 1. This is natural, given that the relationship between EQE and short-circuit density, J_λ at a given monochromated light irradiation with a wavelength of λ, can be expressed as [20]

$$EQE(\%) = 1240/\lambda \times J_\lambda / E_\lambda \times 100 \quad (2.1)$$

where E_λ(W cm^{-2}) is the intensity of the monochromatic light. On the other hand, the V_{oc} value generally decreases with the increase of annealing temperature.

Table 2.1 refers to the summary of the *J-V* measurement in **Figure 2.2** which shows the clear correspondence between maximum EQE and J_{sc} of the PVs. To elucidate effects of RTA annealing on the ZnO/Cu_2O PVs, the structural and morphological properties were characterized by X-ray diffraction (XRD) and field-effect scanning electron microscopy (FESEM).

Table 2.1. Summary of *J-V* measurement of ZnO/Cu_2O PVs as-deposited and annealed at 423, 473, 523, and 573 K.

Annealing Temperature	Maximum EQE (%)	*J*sc (mA cm^{-5})	*V*oc (V)	FF	η (%)
As-deposited	79.9	3.4	0.36	0.56	0.72
423 K	99.9	5.4	0.32	0.51	0.89
473 K	89.2	4.6	0.27	0.32	0.40
523 K	45.5	0.6	0.15	0.26	0.02
573 K	-	0.6	0.03	0.23	0

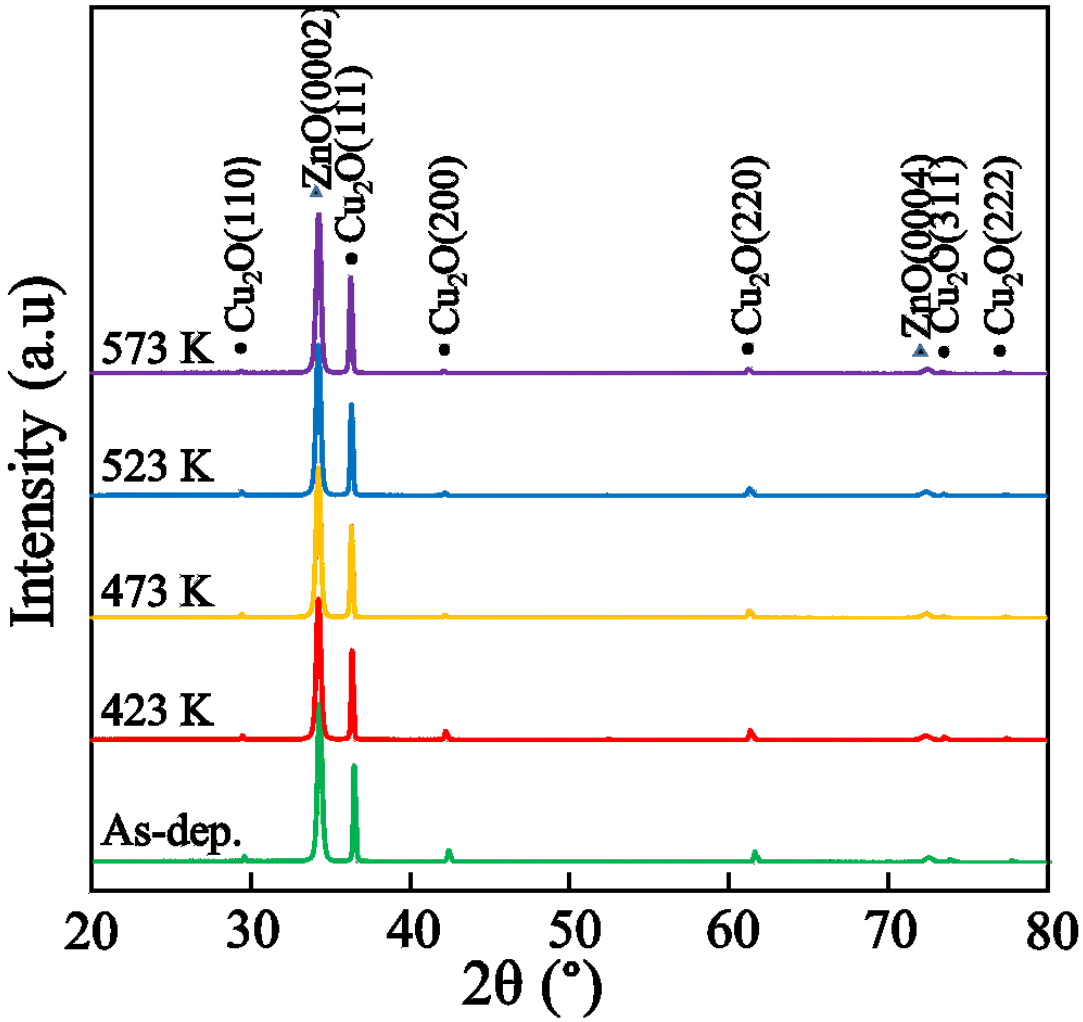

Figure 2.3. X-ray Diffraction of the as-deposited and annealed ZnO/Cu_2O PVs.

Figure 2.3 shows θ-2θ XRD patterns for the ZnO/Cu_2O PVs as-deposited and RTA annealed at 423, 473, 523, and 573 K. under vacuum. All peaks observed were assigned to hexagonal wurtzite ZnO and cubic cuprite Cu_2O, and no significant differences in peak intensity and position were recognized through the samples. The highest peak at 34.3° corresponds to the (0001) plane of the electrodeposited ZnO layer and GZO substrate. The conductive <0001>-oriented GZO substrates were employed to grow ZnO epitaxially and reduce the lattice defects. [21] The electrodeposited Cu_2O layer showed a <111> preferred growth orientation. Because there is a heteroepitaxial relationship between (1×1)ZnO(0001)[11−20] and (1 ×1)Cu_2O(111)[1 −10] with a low lattice mismatch of approximately 7.0 to 7.8%, the (0001) ZnO layer is suitable

to form a lattice matched *p*-*n* junction. Furthermore, since the (111) Cu_2O plane also has a low lattice mismatch of ~4.7% with the (111) Au plane, [22] the GZO/ZnO/Cu_2O/Au PVs fabricated in this study are expected to yield optimal interfaces offering a superior carrier transport property.

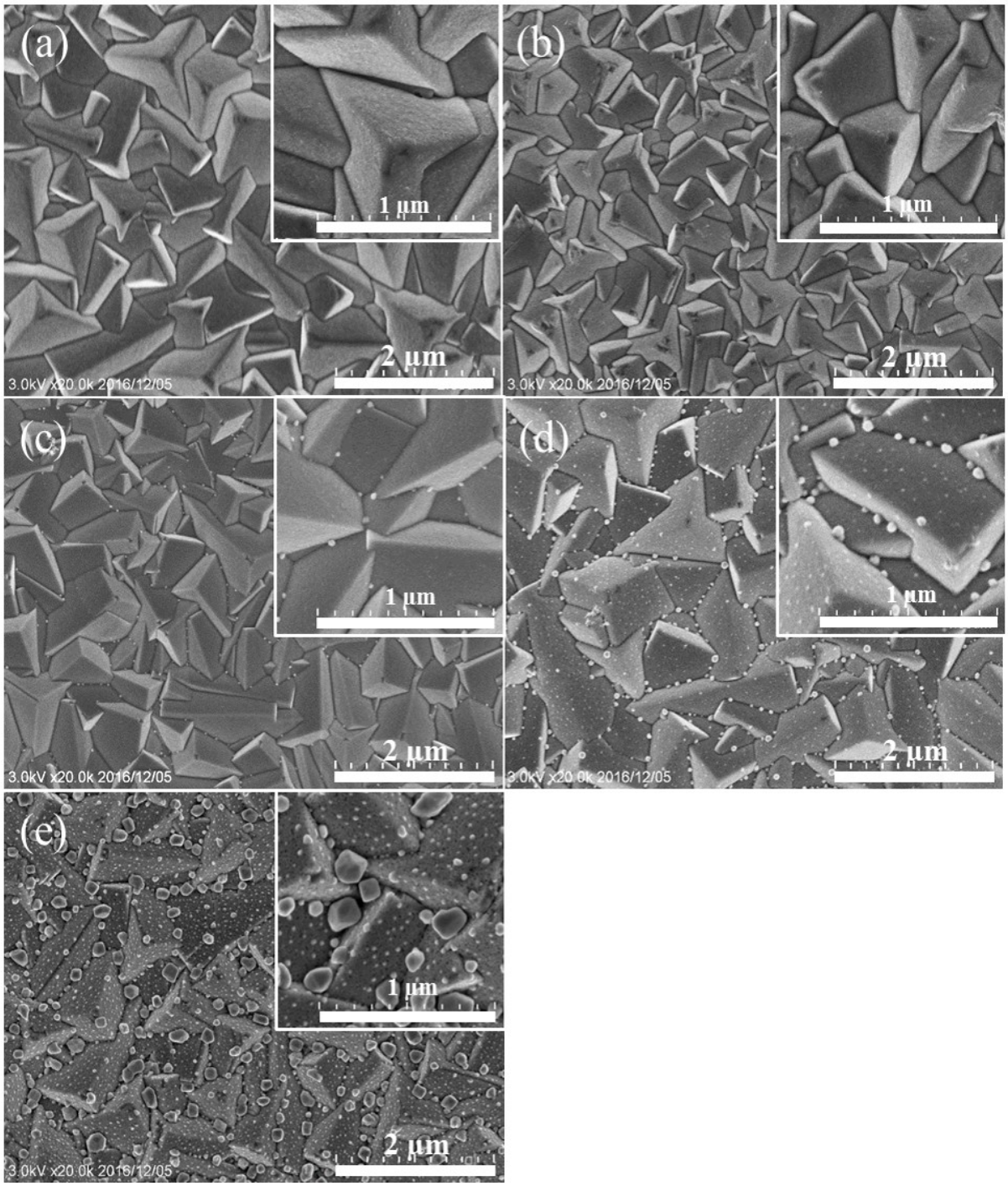

Figure 2.4. FE-SEM surface images of the GZO/ZnO/Cu_2O PVs: (a) as-deposited, annealed at (b) 423, (c) 473, (d) 523, and (e) 573 K. Insets are magnified images.

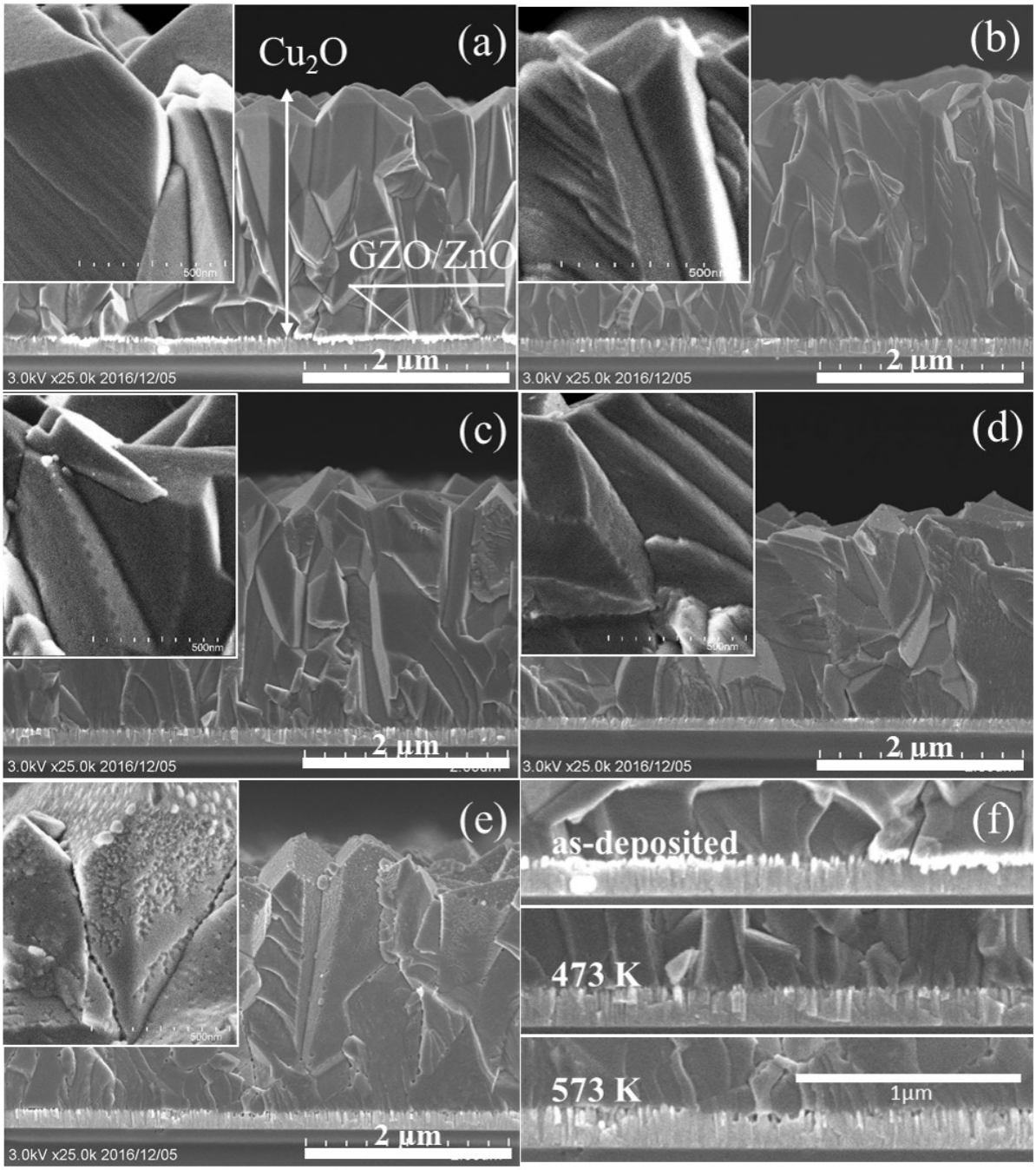

Figure 2.5. Cross-sectional FE-SEM surface images of the GZO/ZnO/Cu_2O PVs: (a) as-deposited, annealed at (b) 423, (c) 473, (d) 523, and (e) 573 K. Insets are magnified images.

Figure 2.4 shows the surface FE-SEM images of the obtained ZnO/Cu_2O PVs. The Cu_2O surface of the as-deposited ZnO/Cu_2O sample is composed of continuous well-faced grains (~477 nm in diameter). The observed three-sided pyramidal grains correspond to the corner of a cubic, indicating that the Cu_2O layer has a <111> preferred orientation, and this is in

agreement with the XRD results. Although the sample annealed at 423 K showed no significant differences in the surface morphology, it can be seen that small particles (30 to 50 nm in diameter) generate mainly on the Cu_2O grain boundaries at 473 K **(Fig. 2.4c).** The size and number of the generated small particles increased with annealing temperature, and larger particles (~130 nm in diameter) were observed over the Cu_2O surface at 573 K **(Fig. 2.4e).**

The cross-sectional FESEM images (**Figure 2.5**) reveals different changes depending on the annealing temperature; nanopores were observed in the cross-section Cu_2O surface along with the generation of the small particles at 473 K. Similar to the small particles, the size and number of the nanopores increased with annealing temperature. These results suggest that the generation of nanopores is related to the formation of small particles. These small particles appearing after annealing at 473 to 573 K are speculated to be grains of copper (Cu) reduced from Cu_2O. Reduction of Cu_2O to Cu, when annealed in vacuum, has been reported by S. Poulston *et al.* using the XPS and XAES method. [23] XPS measurement has been carried out but Cu could not be detected in our case. Further low-incidence angle XRD measurement was carried out at θ=0.5° for samples annealed at 423, 473, 523, and 573 K to investigate the surface of the Cu_2O films but the XRD spectra showed only peaks belonging to Cu_2O. It is concluded that the small particles could not be detected at these annealing temperatures due to inadequate size and distribution. However, analyses at θ=0.5° of the PV samples at higher annealing temperatures of 673, 773 and 873 K, where the said particles grew into layer-like structures showed peaks belonging to metallic copper. **Figure 2.5(f)** shows the heterointerfaces of the PVs of as-deposited and annealed at 473 and 573 K. The heterointerface of the PV annealed at 573 K contains large voids while the heterointerface of the PV annealed at 473 K remains comparatively undamaged. These voids are thought to be coalescences of nanopores, originating from the outward formation of the small particles through the grain boundaries, and are responsible for the disappearance of the p-n rectifying effect of a device. The formation of

voids near the heterointerface is especially significant in reflecting the decrease in V_{oc} due to the deteriorated heterointerface and exposed Cu_2O which severely disrupts the crystal lattice, which also acts as recombination sites. [24] Considering that reduction and oxidation processes being dependent on the transportation or diffusion of ions, [25] this demonstrates the pivotal role of grain boundaries acting as a medium for such movements in low temperature annealing, which affects the formation of nanopores and reduction in oxygen-lean conditions, and possibly explains its dominance in oxidation of Cu_2O in oxygen-rich environment at low temperature as already been reported. [26]

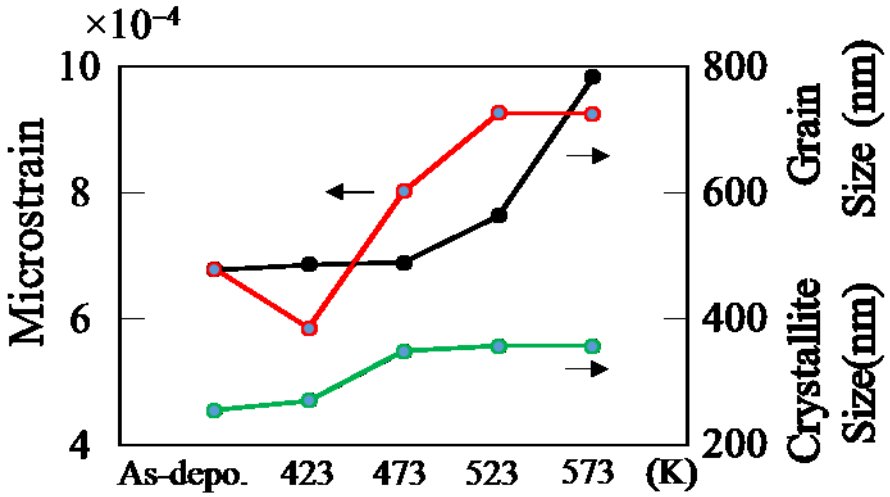

Figure 2.6. Approximated grain size from FE-SEM, microstrain, and crystallite size for as-deposited and annealed samples at 423, 473, 523, and 573 K.

Figure 2.6 shows the average grain size estimated with the conventional intercept method, along with the calculated microstrain (ε) and crystallite size (D) of the samples. The intercept method involved averaging the values of total length of test line drawn on the surface FE-SEM divided by the number of intercepts between the test line and the grain boundaries, while ε and D were calculated from the Size-Strain plot (SSP), described as follows. Since the measured X-ray diffraction peak broadening (β_m) of full width at half maximum (FWHM) of a given

orientation (hkl) includes instrumental broadening (β_i), it can be expressed as the following equation: [27]

$$\beta_m^2 = \beta_{hkl}^2 + \beta_i^2 \quad \textbf{(2.2)}$$

The SSP equation is described as,

$$(d_{hkl}\beta_{hkl}\cos\theta)^2 = k/D\left(d_{hkl}^2\beta_{hkl}\cos\theta\right) + (\varepsilon/2)^2 \quad \textbf{(2.3)}$$

where β_{hkl} and d_{hkl} are the FWHM and interplanar spacing of the Cu_2O at (hkl) orientation, D (nm) is the crystallite size, and k is the Scherrer constant (0.9). [28] D and ε then can be extracted from the y-axis intercept and slope of the graph respectively. The average grain size approximated from the surface FE-SEM images shows a higher value generally as compared to the crystallite size calculated from SSP. It is assumed that these Cu_2O grains consist of several crystallites.[29] Grain boundary migration occurred most dominantly above annealing temperature 523 K, resulting in an approximately 1.6 times larger average grain size at 573 K compared to the as-deposited sample. To further understand the implications of the result, one must first consider the source of strain causing strain broadening. The primary defect type that causes lattice parameter changes or shifts in Bragg reflection is the dislocation-type defect, which among several, includes grain boundaries, lattice dislocations and stacking faults. [30] Since it is generally known that annealing promotes recovery of the crystal structure by removal or rearrangement of dislocations, [31] it is only logical that the strain reduces with the increase of annealing temperature in such small temperature range. However, this does not seem to be the case. Compared to the as-deposited sample, strain decreases after annealing at 423 K, but increases after annealing at temperature 473 K and above. While this indicates the lessening of dislocation defects due to the occurrence of energy release in the Cu_2O layer caused by relaxation after annealing at 423 K, explanation regarding the strain increase aforementioned at higher annealing temperatures is difficult without referring to the microstructural changes observed from the FE-SEM images. It is speculated that at annealing temperature above 473 K,

although the crystallite size increases, the formation of pores in the crystal lattice led to the introduction of new dislocation defects near the boundaries.

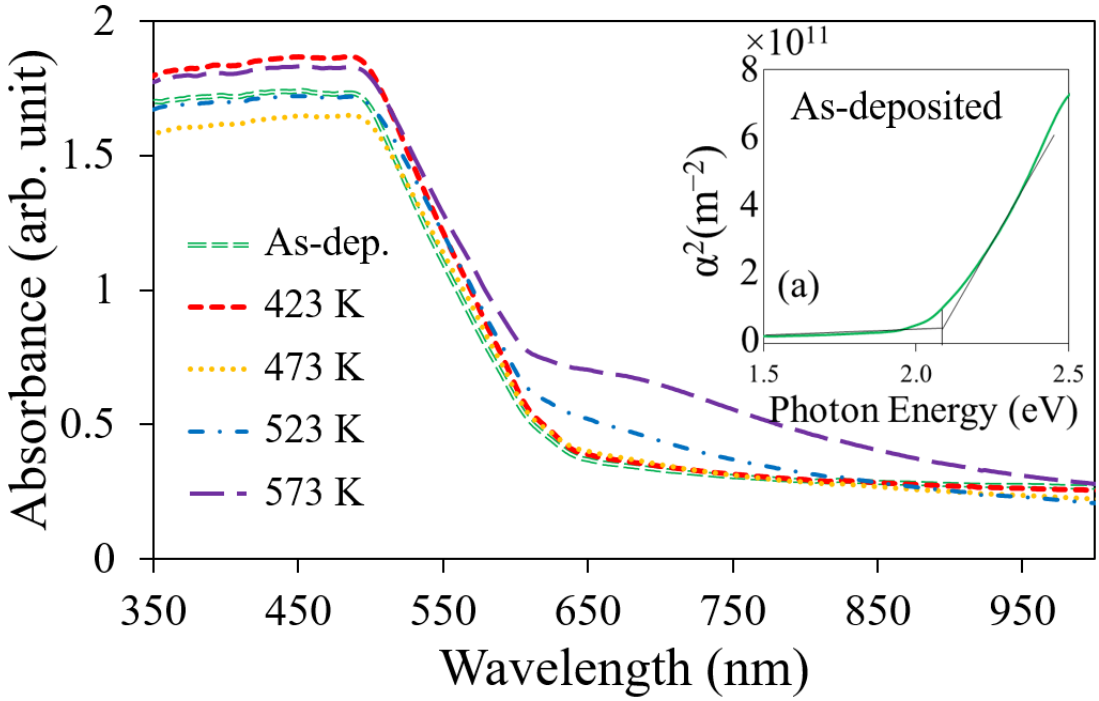

Figure 2.7. UV-vis measurement of the absorbance of GZO/ZnO/Cu_2O layers for as-deposited, 423, 473, 523, and 573 K. Figure 7 (a) as shown inset is the bandgap estimation of the as-deposited films.

Figure 2.7 shows the absorption spectra of as-deposited and annealed samples. All spectrum display the absorption edge of Cu_2O at around 650 nm. Figure 7(a) indicates the corresponding estimated direct bandgap at approximately 2.1 eV. All the samples have a similar absorption edge, which is in good agreement with the constant direct bandgap obtained regardless of annealing as reported by Shinagawa *et al.* [16] and Mahalingam *et al.*[12] While the absorbance intensity varies among the samples for the as-deposited and annealed samples in the wavelength region of the 380 to 650 nm, there is no observable trend dependence on the annealing temperature. The variation in absorbance intensity can be attributed to the slight difference in actual thickness due to the electrodeposition technique. For 523 and 573 K, the

reflection by small particles (Cu) at the surface of the samples not subtracted from the transmittance mode due to technical difficulties might contribute to the increase of absorbance spectra above 650 nm.

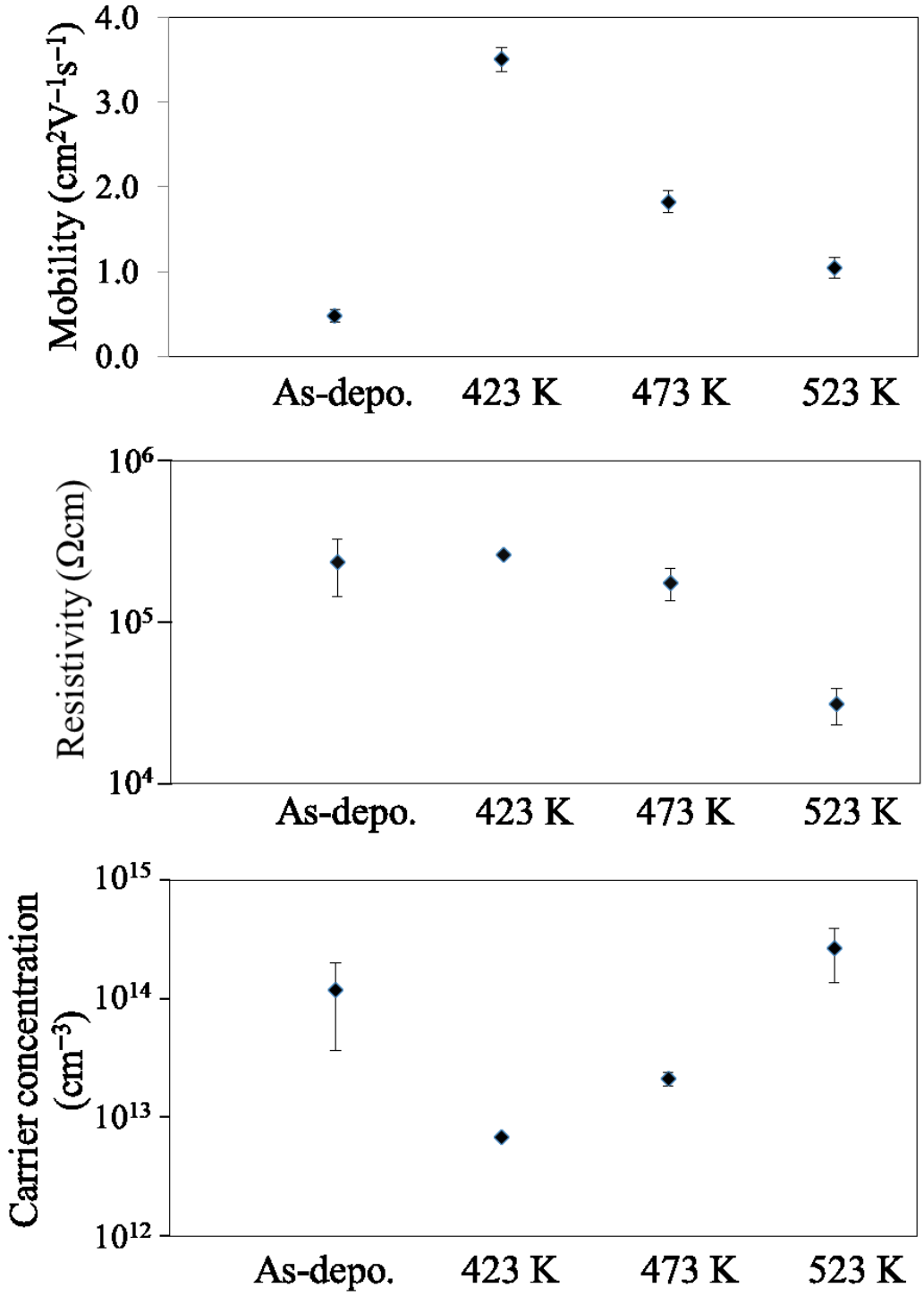

Figure 2.8. Hall measurement regarding the carrier mobility, resistivity, and carrier concentration of as-deposited Cu_2O and annealed in vacuum for 1 hour at 423, 473, and 523 K.

Figure 2.8 is the results of Hall measurement of the free-standing Cu_2O layers removed from GZO substrate by a mechanical splitting method for as-deposited samples and samples annealed at 423, 473, and 523 K. Samples for 573 K could not be measured due to the difficulty in removing the layer due to an increase of adhesion. The resistivity of the samples is within one order of magnitude from 10^4 to 10^5 Ω cm with a slight decrease with the increase of annealing temperature. The lowest resistivity obtained is at 523 K at 3.1×10^4 Ω cm, in agreement with the value previously reported. [16] The carrier concentrations were in the range of 10^{12} to 10^{14}, with the lowest at 423 K at 6.9×10^{12} m^{-3}, more than one order of magnitude decrease from the as-deposited Cu_2O. As it is generally known that the carrier concentration in a p-type Cu_2O originates largely from the Cu vacancies[32], which also are intrinsic point defects. The decrease of carrier concentration would mean a decrease in point defects when annealed at 423 K. Carrier mobility demonstrates 7 times increase from 0.5 $cm^2\ V^{-1}\ s^{-1}$ as-deposited film to 3.5 $cm^2\ V^{-1}\ s^{-1}$ when annealed at 423 K, 3.6 times increase at 473 K to 1.8 $cm^2\ V^{-1}\ s^{-1}$, and 2 times increase at 523 K to 1.0 $cm^2\ V^{-1}\ s^{-1}$. It is generally known that the lessening of scattering defects like grain boundaries and impurities facilitates movements of carriers, leading to the increase of carrier mobility. From the microstructure point of view as discussed earlier, we know that along with the increase of annealing temperature, the number of grain boundaries decreases while the number and size of pores increase. The overall mobility increase can be attributed to the overall decrease in grain boundaries, while the drop after annealing at temperatures higher than 473 K can be attributed to the pores which might act as scattering defects.

$$D=(kT/q)\mu \quad \textbf{(2.4)}$$

$$L=(D\tau)^{1/2} \quad \textbf{(2.5)}$$

As denoted in **equation (2.4),** also known as the Einstein relation, carrier mobility, μ is directly proportional to diffusion coefficient, expressed as D here.[33] k is the Boltzmann constant, T is the temperature, and q represents the magnitude of electric charge of electron. Diffusion coefficient D affects diffusion length L as shown in **equation (2.5)**,[34] where τ is carrier lifetime, and the relation between L and short-circuit current J_{sc} can be expressed as

$$J_{sc}=qG\left(L_p+L_n\right) \quad \textbf{(2.6)}$$

where G is generation rate, L_p is hole diffusion length and L_n is electron diffusion length.[35]

From these equations, an increase in carrier mobility μ leads to the increase of diffusion coefficient, which in turn improves charge collection and consequently the J_{sc}, which is concordant with our results of heightened J_{sc} values relating to the increase of carrier mobility.

2.4. Conclusions

We have demonstrated that annealing is a valid method to improve the performance of an electrochemically prepared Cu_2O-based photovoltaic device, especially in terms of EQE and J_{sc}. An increase is observed in EQE to nearly 100% for the sample annealed at 423 K at the wavelength of 410 nm, showing improved charge collection. This corresponds to the increase of J_{sc} from 3.4 mA cm^{-2} to 5.4 mA cm^{-2} when annealed at 423 K. Both optical evaluation and XRD analysis indicates proper formations of the Cu_2O layers of bandgap energy of 2.0 eV and preferred (111) orientation. FE-SEM observations revealed the appearance of small particles at the surface along the grain boundaries starting at 473 K (speculated to be metallic copper), with the subsequent formation of pores in the bulk. Two main carrier scattering defects, grain boundaries, and pores affecting the PV performances are being discussed. The number of grain boundaries decreases while the number and size of pores increase with the increase of annealing temperature. It is speculated that the coalescences of pores into voids at the heterointerface acted as carrier recombination sites and consequently lowered the V_{oc}. Relaxation occurred when the Cu_2O layer was annealed at 423 K, with no observable pores. The optimal results observed an increase in EQE and J_{sc} at 423 and 473 K, supported by the evidence of increased carrier mobility from Hall effect measurement which showed a lessening of scattering defects at these annealing temperatures. Factors such as annealing atmosphere (oxygen partial pressure), initial grain size, and substrate that affects the resulting microstructural changes proved to be very important in determining the optimum annealing temperature, explaining the discrepancy of past reported results. Nonetheless, annealing proves to be a facile, effective method to increase the PV performance of the electrochemically prepared Cu_2O based PV.

REFERENCES

[1] D. Kang, T.W. Kim, S.R. Kubota, A.C. Cardiel, H.G. Cha, K.S. Choi, Electrochemical Synthesis of Photoelectrodes and Catalysts for Use in Solar Water Splitting, Chem. Rev. 115 (2015) 12839–12887. doi:10.1021/acs.chemrev.5b00498.

[2] G. V. Govindaraju, G.P. Wheeler, D. Lee, K.S. Choi, Methods for electrochemical synthesis and photoelectrochemical characterization for photoelectrodes, Chem. Mater. 29 (2017) 355–370. doi:10.1021/acs.chemmater.6b03469.

[3] G.H.A. Therese, P.V. Kamath, Electrochemical Synthesis of Metal Oxides and Hydroxides, Chem. Mater. 12 (2000) 1195–1204. doi:10.1021/cm990447a.

[4] R. Palitha, Electrodeposited Cu_2O Thin Films for Fabrication of CuO/Cu_2O Heterojunction, in: Sol. Cells - Thin-Film Technol., InTech, 2011. doi:10.5772/19789.

[5] A.E. Rakhshani, Preparation, characteristics and photovoltaic properties of cuprous oxide-a review, Solid State Electron. (1986). doi:10.1016/0038-1101(86)90191-7.

[6] J. Katayama, K. Ito, M. Matsuoka, J. Tamaki, Performance of Cu_2O/ZnO solar cell prepared by two-step electrodeposition, J. Appl. Electrochem. 34 (2004) 687–692. doi:10.1023/B:JACH.0000031166.73660.c1.

[7] M. Izaki, T. Shinagawa, K.-T. Mizuno, Y. Ida, M. Inaba, A. Tasaka, Electrochemically constructed p-Cu 2 O/n-ZnO heterojunction diode for photovoltaic device, J. Phys. D. Appl. Phys. 40 (2007) 3326–3329. doi:10.1088/0022-3727/40/11/010.

[8] S. Bijani, R. Schrebler, E.A. Dalchiele, M. Gabás, L. Martínez, J.R. Ramos-Barrado, Study of the nucleation and growth mechanisms in the electrodeposition of micro- and nanostructured Cu_2O thin films, J. Phys. Chem. C. 115 (2011) 21373–21382. doi:10.1021/jp208535e.

[9] S. Leopold, M. Herranen, J.-O. Carlsson, Spontaneous Potential Oscillations in the Cu(II)/Tartrate and Lactate Systems, Aspects of Mechanisms and Film Deposition, J. Electrochem. Soc. 148 (2001) C513. doi:10.1149/1.1379949.

[10] J. Lee, Y. Tak, Epitaxial Growth of Cu_2O (111) by Electrodeposition, Electrochem. Solid-State Lett. 2 (1999) 559–560. doi:10.1149/1.1390903.

[11] M. Izaki, T. Omi, Transparent zinc oxide films prepared by electrochemical reaction, Appl. Phys. Lett. (1995) 2439. doi:10.1063/1.116160.

[12] T. Mahalingam, J.S.P. Chitra, J.P. Chu, S. Velumani, P.J. Sebastian, Structural and annealing studies of potentiostatically deposited Cu_2O thin films, Sol. Energy Mater. Sol. Cells. 88 (2005) 209–216. doi:10.1016/j.solmat.2004.05.026.

[13] R.-M. Liang, Y.-M. Chang, P.-W. Wu, P. Lin, Effect of annealing on the electrodeposited Cu_2O films for photoelectrochemical hydrogen generation, Thin Solid Films. 518 (2010) 7191–7195. doi:10.1016/j.tsf.2010.04.073.

[14] T. Dimopoulos, A. Peić, S. Abermann, M. Postl, E.J.W. List-Kratochvil, R. Resel, Effect of thermal annealing in vacuum on the photovoltaic properties of electrodeposited Cu_2O-absorber solar cell, EPJ Photovoltaics. 5 (2014) 50301. doi:10.1051/epjpv/2014005.

[15] J.H. Hsieh, P.W. Kuo, K.C. Peng, S.J. Liu, J.D. Hsueh, S.C. Chang, Opto-electronic properties of sputter-deposited Cu_2O films treated with rapid thermal annealing, Thin Solid Films. (2008). doi:10.1016/j.tsf.2007.07.097.

[16] T. Shinagawa, M. Onoda, B.M. Fariza, J. Sasano, M. Izaki, Annealing effects and photoelectric properties of single-oriented Cu_2O films electrodeposited on Au(111)/Si(100) substrates, J. Mater. Chem. A. 1 (2013) 9182. doi:10.1039/c3ta11116d.

[17] L.J. van der Pauw, A METHOD OF MEASURING SPECIFIC RESISTIVITY AND HALL EFFECT OF DISCS OF ARBITRARY SHAPE, in: Semicond. Devices Pioneer. Pap., WORLD SCIENTIFIC, 1991: pp. 174–182. doi:10.1142/9789814503464_0017.

[18] M. Miyake, K. Murase, T. Hirato, Y. Awakura, Hall effect measurements on CdTe layers electrodeposited from acidic aqueous electrolyte, J. Electroanal. Chem. 562 (2004) 247–253. doi:10.1016/j.jelechem.2003.09.008.

[19] K.P. Musselman, A. Wisnet, D.C. Iza, H.C. Hesse, C. Scheu, J.L. MacManus-Driscoll, L. Schmidt-Mende, Strong Efficiency Improvements in Ultra-low-Cost Inorganic Nanowire Solar Cells, Adv. Mater. 22 (2010) E254–E258. doi:10.1002/adma.201001455.

[20] I. Robel, V. Subramanian, M. Kuno, P. V. Kamat, Quantum Dot Solar Cells. Harvesting Light Energy with CdSe Nanocrystals Molecularly Linked to Mesoscopic TiO_2 Films, J. Am. Chem. Soc. 128 (2006) 2385–2393. doi:10.1021/ja056494n.

[21] M. Izaki, J. Komori, K. Shimizu, T. Koyama, T. Shinagawa, Room temperature ultraviolet light-emitting ZnO vertical nanowires prepared by electrochemical growth, Phys. Status Solidi Appl. Mater. Sci. 214 (2017) 1600473. doi:10.1002/pssa.201600473.

[22] B.M. Fariza, J. Sasano, T. Shinagawa, S. Watase, M. Izaki, Light-assisted electrochemical construction of (111)Cu_2O/(0001)ZnO heterojunction, Thin Solid Films. 520 (2012) 2261–2264. doi:10.1016/j.tsf.2011.09.022.

[23] S. Poulston, P.M. Parlett, P. Stone, M. Bowker, Surface Oxidation and Reduction of CuO and Cu_2O Studied Using XPS and XAES, Surf. Interface Anal. 24 (1996) 811–820. doi:10.1002/(SICI)1096-9918(199611)24:12<811::AID-SIA191>3.0.CO;2-Z.

[24] L.E. Black, Surface Recombination Theory, in: 2016: pp. 15–28. doi:10.1007/978-3-319-32521-7_2.

[25] G. Liu, Y. Zhu, K. Mimura, M. Isshiki, Effect of Alloying Element of S, Se or te on Oxidation Resistance of Cu at 573-873 K, Open Corros. J. 3 (2010) 92–98. http://www.benthamscience.com/open/tocorrj/articles/V003/92TOCORRJ.pdf.

[26] K. Mimura, J.-W. Lim, M. Isshiki, Y. Zhu, Q. Jiang, Brief review of oxidation kinetics of copper at 350 °C to 1050 °C, Metall. Mater. Trans. A. 37 (2006) 1231–1237. doi:10.1007/s11661-006-1074-y.

[27] A. Khorsand Zak, W.H. Abd. Majid, M.E. Abrishami, R. Yousefi, X-ray analysis of ZnO nanoparticles by Williamson–Hall and size–strain plot methods, Solid State Sci. 13 (2011) 251–256. doi:10.1016/j.solidstatesciences.2010.11.024.

[28] R. Jenkins, R.L. Snyder, Introduction to X-ray Powder Diffractometry, John Wiley & Sons, Inc., Hoboken, NJ, USA, 1996. doi:10.1002/9781118520994.

[29] J.R. Ares, A. Pascual, I.J. Ferrer, C. Sánchez, Grain and crystallite size in polycrystalline pyrite thin films, Thin Solid Films. 480–481 (2005) 477–481. doi:10.1016/j.tsf.2004.11.064.

[30] T. Ungár, Dislocation model of strain anisotropy, Powder Diffr. 23 (2008) 125–132. doi:10.1154/1.2918549.

[31] R.D. Doherty, D.A. Hughes, F.J. Humphreys, J.J. Jonas, D. Juul Jensen, M.E. Kassner, W.E. King, T.R. McNelley, H.J. McQueen, A.D. Rollett, Current issues in recrystallization: A review, Mater. Today. 1 (1998) 14–15. doi:10.1016/S1369-7021(98)80046-1.

[32] H. Raebiger, S. Lany, A. Zunger, Origins of the p-type nature and cation deficiency in Cu2 O and related materials, Phys. Rev. B - Condens. Matter Mater. Phys. 76 (2007). doi:10.1103/PhysRevB.76.045209.

[33] A.H. Marshak, D. Assaf, A generalized Einstein relation for semiconductors, Solid. State. Electron. 16 (1973) 675–679. doi:10.1016/0038-1101(73)90110-X.

[34] S.M. Sze, K.K. Ng, p - n Junctions, in: Phys. Semicond. Devices, Third Edit, John Wiley & Sons, Inc., Hoboken, NJ, USA, 2006: pp. 77–133. doi:10.1002/9780470068328.ch2.

[35] H.-P. Wang, T.-Y. Lin, M.-L. Tsai, W.-C. Tu, M.-Y. Huang, C.-W. Liu, Y.-L. Chueh, J.-H. He, Toward Efficient and Omnidirectional n-Type Si Solar Cells: Concurrent Improvement in Optical and Electrical Characteristics by Employing Microscale Hierarchical Structures, ACS Nano. 8 (2014) 2959–2969. doi:10.1021/nn500257g.

CHAPTER 3

Fabrication of Basic CuO PV with Polysiloxane as a Buffer Layer

3.1 Introduction

3.1.1 CuO as a light-absorbing layer in PV

Copper (II) oxide, CuO, the second stable form of copper oxides, is a p-type semiconductor[1] and can act as a light-absorbing layer. It has attracted increasing attention as a photovoltaic layer in solar cells due to its 1.4 eV bandgap energy and high optical absorption coefficient, but the performance was limited at a low level irrespective of the CuO preparation

method.[2–5] Kidowaki *et al.*investigated the CuO PV with different structures, such as ITO(indium tin oxide)/CuO/ZnO, ITO/ZnO/CuO, and CuO/C_{60}. Especially, the *Voc* obtained are 2.7×10^{-4}, 8.2×10^{-4}, and 4.5×10^{-2} V respectively, which were poor compared to the Cu_2O based photovoltaics. There are several obstacles in the fabrication of the CuO PV, such as poor condition of the heterojunction, crystal distortion and poor CuO crystal quality.

The CuO layers can be prepared by thermal processes including thermal oxidation[2,6] and chemical solution process such as electrodeposition.[7] The electrodeposition process has been used for the electroplating of metals in the surface finishing industry, and oxide and compound films for electronic and optical applications can be prepared by electroplating in addition to metallic layers. A previous report of a 1.4-eV-bandgap CuO layer by Izaki *et al.* with an improved photoactivity has been prepared by electrodeposition in a basic aqueous solution containing copper acetate hydrate and ammonia.[8] Here we investigate the fabrication of CuO PV based on the method used as reported.

3.1.2 Buffer layer to improve CuO PV

A buffer layer is usually a highly-resistive / large-bandgap layer that is inserted between the light-absorbing layer and the charge collecting layer (window layer) that aims to improve the heterointerface of the PV by suppressing recombination of charge carriers. A buffer layer should form a junction with the light-absorbing layer while allowing light to penetrate the junction region and the absorber layer.[9] It minimizes the interface recombination losses and helps attain a large band-bending. The role of the buffer layer has been reported to benefit the PV performances, especially in improving the $V_{OC,}$ and has been commonly used in the optimization of thin-film PVs.[10] The role of buffer layers has also been reported in silicon PVs[11], polymer PVs[12], CZTS [13]and CIGS[14].

It was also reported by Izaki *et al.*in electrodeposited ZnO(nanowire)/Cu_2O when a highly resistive ZnO intermediate layer was used as the buffer layer, a PCE of 1.26% was obtained.[15]

Zamzuri *et al*. also demonstrated the possibility of increasing the V_{OC} by inserting an intermediate titanium dioxide (TiO_2) as a buffer layer.[16] A huge improvement of V_{OC} was also achieved in the Cu_2O-based PV with a record of 1.2 V when gallium oxide (Ga_2O_3) was used as the buffer layer.[17]

Here, we explore the effects of a well-studied silicon-containing polymer, polysiloxane [18,19], prepared by spin coating as a buffer layer in the CuO PV[20], and investigate the CuO as a light-absorbing layer in PV. Polysiloxane has excellent chemical and physical properties such as thermal stability and high resistivity.[19,21] Polysiloxane is indeed a good insulator film with a reported conductivity of $1.8\times10^{-14}\ \Omega^{-1}\ cm^{-1}$[22], suitable as a buffer layer. Also, it is a unique heat resistant and flexible inorganic polymer, on top of being able to be fabricated by a simple sol-gel method as will be described in the following section.

3.2 Experimental Procedures

An aqueous solution containing 0.05 mol L^{-1} copper (II) nitrate hydrate and 0.05 mol L^{-1} ammonium nitrate was used for the electrodeposition of the 1.3-μm-thick-CuO film. The solution pH was adjusted to pH 9 by adding ammonia water. The solution was prepared with reagent grade chemicals and 15-MΩ cm-resistivity distilled water purified by a Millipore Ellix-UV. A (111)-oriented Au coated Si wafer (KOBELCO Research Institute, Inc.) was used as the substrate. The electrodeposition was potentiostatically carried out without stirring at 297 K by anodic polarization at an electric charge of 1 C cm^{-2} and at a potential of 900 mV versus an Ag/AgCl reference electrode. A Pt sheet was used as the counter electrode. Prior to electrodeposition, the Au/Si substrate was rinsed in acetone and then cathodically polarized in an aqueous solution containing pyrophosphate acid and potassium hydroxide for 30 sec. The polysiloxane layers were prepared on the CuO layer by following processes. (i) Spin-coating the tetrahydrofuran (THF) solution with dissolved 0.5-1.5 mass% polymethylphenylsilane (PMPS) (OGSOL, Osaka Gas Chemical, Co., Ltd.), (ii) ultraviolet light irradiation for 30 sec. using a high-pressure mercury lamp (USHIO, OPTICA MODULEX, 500W), and (iii) baking at 523 K for 15 min.[20] The Al electrode was prepared by vacuum evaporation.

The Fourier-transformed infrared spectra were recorded by an attenuated total reflection (ATR) technique using a Thermo Electron Nicolet 4700 FT-IR Spectrometer and a diamond ATR unit (Smiths, Durasampl*IR*-II^{TM}). The surface and cross-sectional structures were observed using a field emission scanning electron microscope (Hitachi, SU-8000). The surface roughness was measured using laser spectroscopy (Keyence VK-8510). The current density-voltage curves were measured using a Keithley 2400 source meter in dark and under AM1.5 illumination.

3.3 Results and Discussion

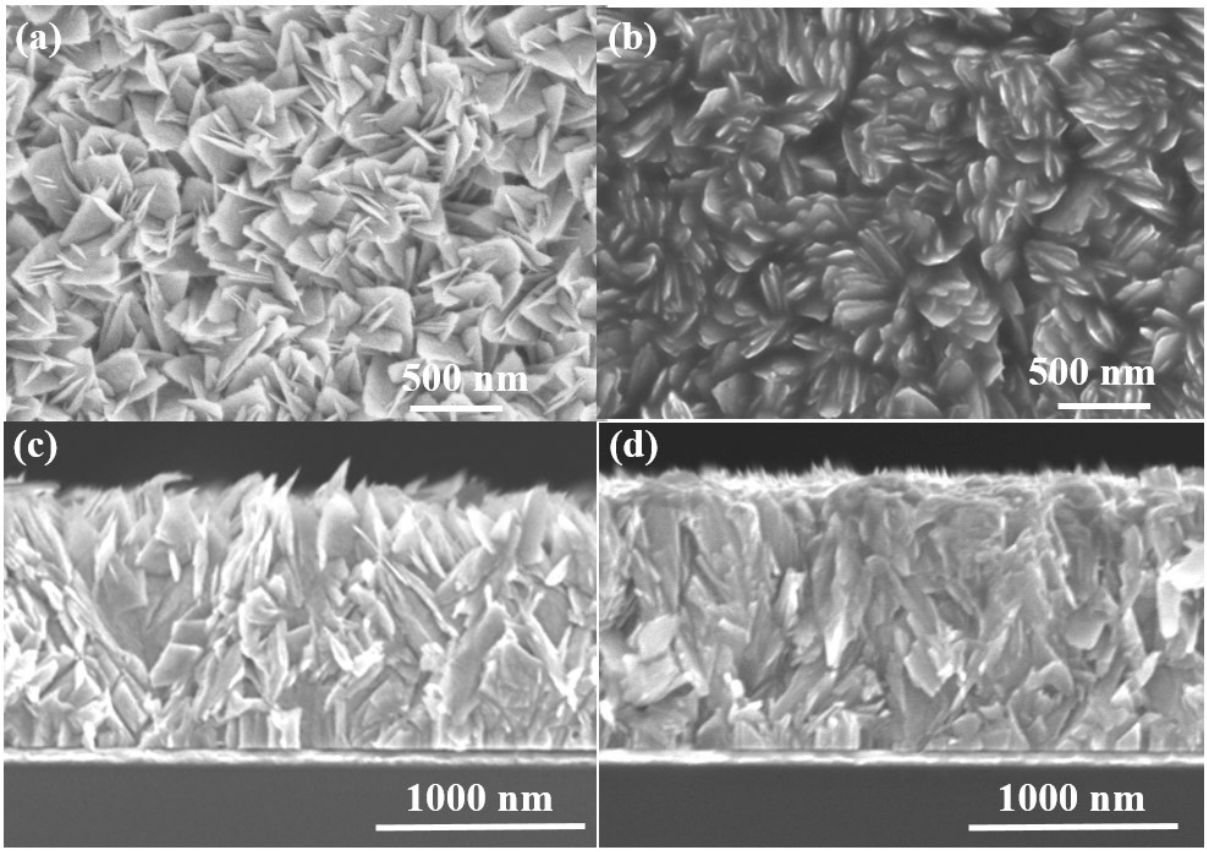

Figure 3.3. The scanning electron microscopy images of surface morphologies and cross-sectional structures for CuO layer (a, c) and polysiloxane/CuO diode (b, d).

Figure 3.1 shows the surface and cross-sectional images of the CuO layers with and without the polysiloxane layer prepared with 1.0% PMPS solutions. The CuO layer possessed the (002)-out-of-plane orientation with random in-plane orientation[8] and was composed of aggregates of fan-shaped grains with the size of approximately 100-150 nm and a thickness of approximately 15 nm. Fan-shaped CuO grains with sharp edges could also be observed near the surface in the cross-sectional image. The surface morphology of the CuO grains rounded slightly after the polysiloxane layer coating, and some pores between the CuO grains were filled with the polysiloxane layer. The polysiloxane layer covered the entire of the CuO surface including the area above the grain boundaries, but the estimation of the thickness of the

polysiloxane layer was difficult due to the large surface roughness as observed from the cross-sectional image.

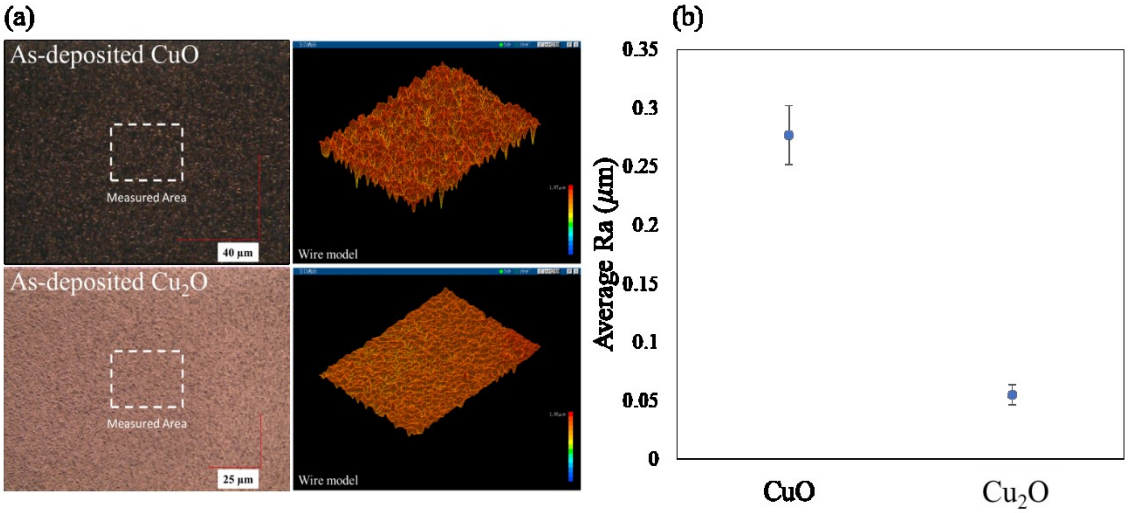

Figure 3.2. The surface roughness (Ra) measurement from laser microscopy of the CuO and Cu_2O layers (a) and the average surface roughness calculated (b).

Figure 3.2 shows the laser microscopy measurement of the surface roughness (Ra) of CuO with Cu_2O as a comparison. The Ra calculated averaged at 0.28 and 0.06 µm respectively. **Figure 3.2 (b)** shows an approximately 5 times larger Ra value of the CuO layer compared to that of the Cu_2O layer. This indicates a very high irregularity of the CuO surface with large surface roughness.

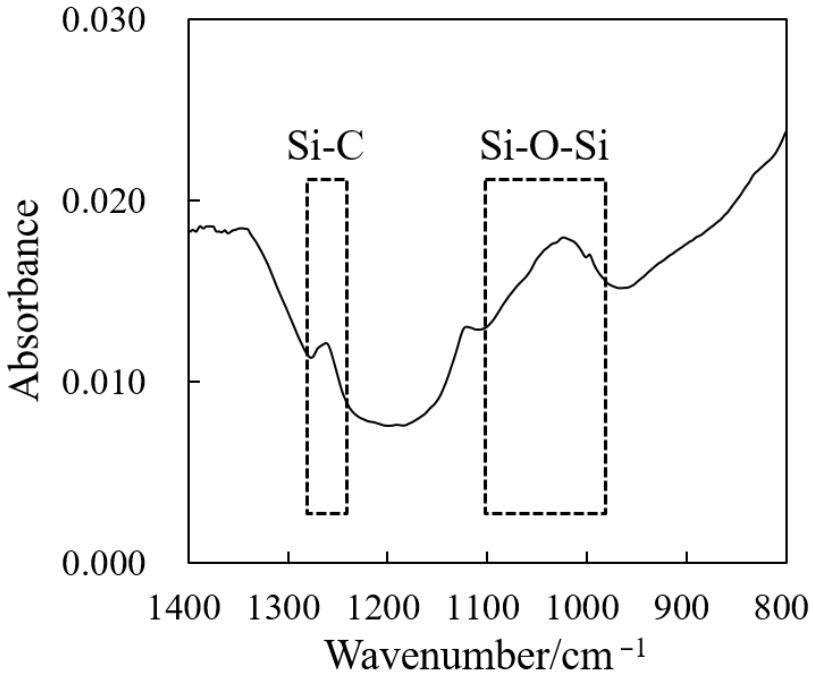

Figure 3.3. The Fourier-transformed infra-red (FT-IR) spectrum for polysiloxane/CuO layers.

Figure 3.3 shows the FT-IR spectra for the polysiloxane layer-stacked CuO layer prepared from 1.0% PMPS solutions. It was confirmed that the CuO layer did not possess an absorption band at the wave number ranging from 800 to 1400 cm^{-1}. The strong absorption band at wavenumber around 1070 cm^{-1} was identified as the stretching vibration of Si-O and Si-O-Si bonding.[20,23] The weak absorption band at around 1260 cm^{-1} was identified as the stretching vibration of Si-C bonding. Polysiloxane is represented by the chemical formula of $[(CH_3)_2\text{-Si-O}]_n$, formed by ultraviolet-light induced decomposition of the polymethylphenylsilane (PMPS), and involved both Si-O and Si-C bonding.[24,25] The detection of both Si-C and Si-O-Si bonding by FT-IR measurements indicated the formation of the polysiloxane layer on the CuO layer.

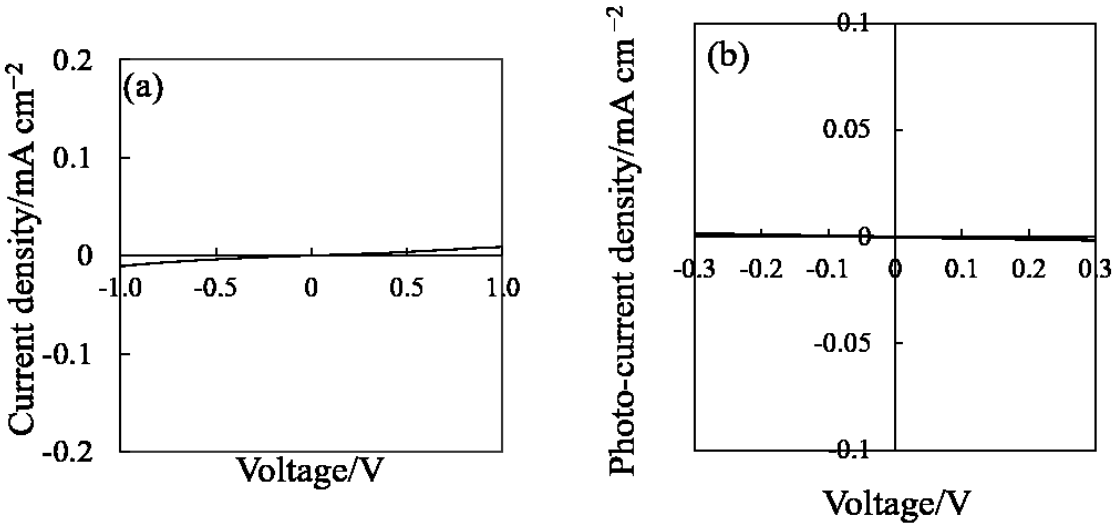

Figure 3.4. The current density-voltage curves recorded for Al/CuO/Au heterostructure in (a) dark and under (b) AM1.5G illumination.

Figure 3.4 shows the current density-voltage curves recorded for Al/CuO/Au heterostructures without the polysiloxane layer in the (a) dark and (b) under AM1.5G illumination. An almost linear proportionality was observed for the polysiloxane-free-Al/CuO/Au heterostructure. Since it was predicted that the ohmic and Schottky contacts were formed between the Au/CuO and CuO/Al heterointerfaces from the energy states as already reported,[26] the ohmic behavior could be due to the electrical contact between the Au and Al metal layers through the pores of the CuO layer. The polysiloxane-free-Al/CuO/Au heterostructure showed an ohmic behavior even under AM1.5 illumination, and no photocurrent density was observed.

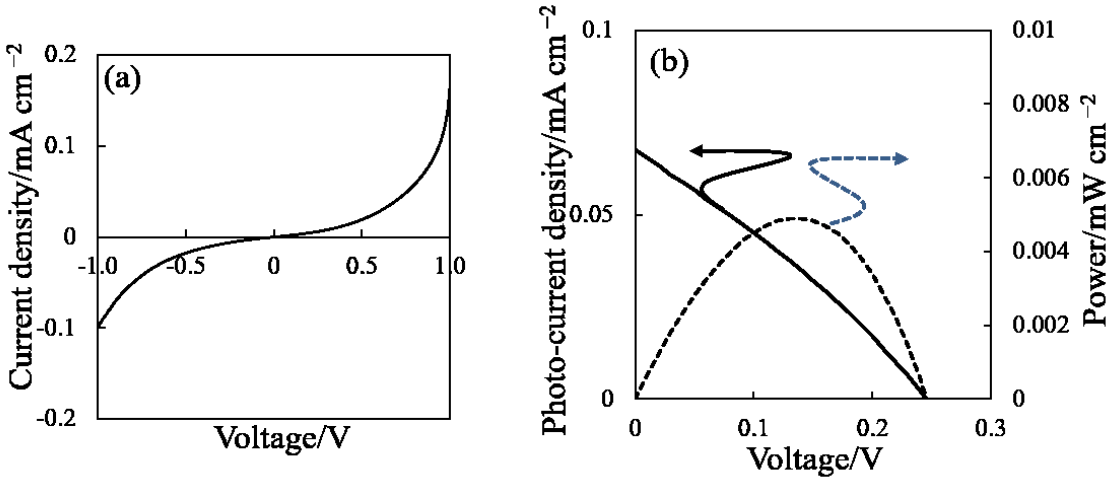

Figure 3.5. The current density-voltage curves recorded for Al/polysiloxane/CuO/Au diodes in (a) dark and (b) under AM1.5G illumination.

Figure 3.5 shows the current density-voltage curves recorded for Al/polysiloxane/CuO/Au diodes in (a) dark and (b) under AM1.5G illumination. The rectification feature in dark was improved by the insertion of the polysiloxane layer, and the rectification ratio of the current densities at +1V and −1V was estimated to be 1.7, although a large leakage current density remained. The polysiloxane layer prepared on a quartz glass substrate, in the same manner, showed bandgap energy of 3.7 eV from the optical absorption spectrum.

Figure 3.6 shows the schematic diagram of the device before (a) and after (b) the insertion of the polysiloxane buffer layer. Although the exact location of the Fermi level is not clear at present, the polysiloxane/Al interface could be an ohmic contact because polysiloxane is not a p-type semiconductor. The polysiloxane layer could partly make contact under the Au layer through the pores in the CuO layer like the Au/CuO/Al heterostructure, and the carrier could be transported through the polysiloxane layer by tunneling effect. The electrical characteristics observed for the Al/polysiloxane/CuO/Au diode originated from the polysiloxane/CuO and polysiloxane/Au interfaces.

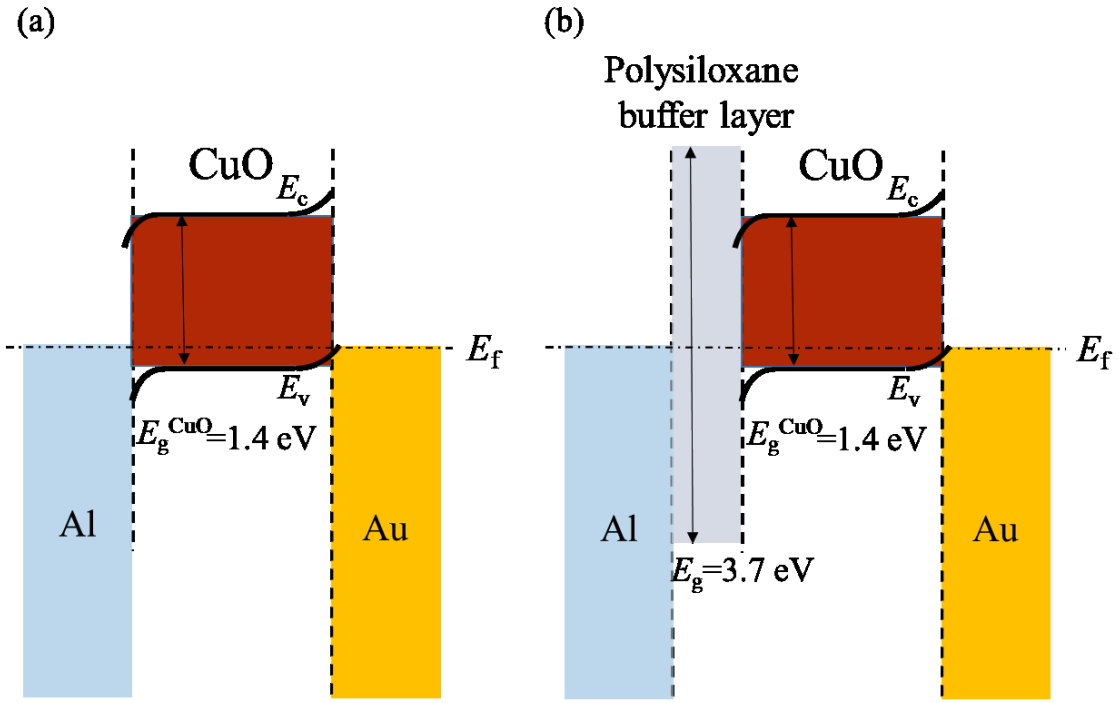

Figure 3.6. The schematic diagram of before and after the polysiloxane buffer layer insertion, (a) Al/CuO/Au and (b) Al/Polysiloxane/CuO/Au.

The Al/Polysiloxane/CuO/Au diode showed photovoltaic performance under AM1.5 irradiation as shown in **Figure 3.5 (b)**. The open-circuit voltage (V_{OC}), short-circuit current density (J_{SC}), and Fill factor (FF) were estimated to be 0.24 V, 0.067 μA cm^{-2}, and 0.29, respectively. The conversion efficiency was calculated to be 4.6x10^{-7}%. The V_{OC} value was much larger than 0.28 mV reported for the electrodeposited CuO-PV-device[3] and slightly lower than 0.37 V for the thermally-prepared CuO/ZnO-PV-device.[2] The conversion efficiency was much lower than 0.05 % for the thermally prepared CuO/ZnO-PV-device.[2] Since the CuO layer was reduced to metallic Cu during the preparation of Ga: ZnO window by sputtering, the Al/polysiloxane/CuO/Au diode did not possess a transparent conductive window and this hindered the collection of carriers generated by photons. The CuO and polysiloxane layers showed very high resistivities of 2.2x10^5 Ω cm [27] and over 10^8 Ω cm, respectively. Since the carriers collected by the Al electrode originated from the part in the vicinity of the Al

electrode, the practical J_{SC} value would be higher than that measured in this study in the case of possessing a transparent conductive window. Thus, the insertion of the transparent conductive window, optimization of the device structure, and improvements of the qualities of the CuO and polysiloxane layers are necessary to improve the overall photovoltaic performance.

3.4 Conclusions

The polysiloxane/CuO diodes were constructed by electrodeposition of the (002)-oriented CuO layer followed by the preparation of polysiloxane layer using polymethylphenylsilane (PMPS) which showed a rectification feature in dark, along with the photovoltaic performance of 0.24 V in V_{OC} under AM1.5 illumination. This demonstrates the viability of CuO as the light-absorbing layer in a PV, but a continuous and smooth CuO layer is needed in order to utilize its photovoltaic ability.

REFERENCES

[1] F.P. Koffyberg, F.A. Benko, A photoelectrochemical determination of the position of the conduction and valence band edges of p-type CuO, J. Appl. Phys. 53 (1982) 1173–1177. doi:10.1063/1.330567.

[2] P. Wang, X. Zhao, B. Li, ZnO-coated CuO nanowire arrays: fabrications, optoelectronic properties, and photovoltaic applications, Opt. Express. 19 (2011) 11271. doi:10.1364/OE.19.011271.

[3] H. Kidowaki, T. Oku, T. Akiyama, Fabrication and characterization of CuO/ZnO solar cells, J. Phys. Conf. Ser. 352 (2012) 012022. doi:10.1088/1742-6596/352/1/012022.

[4] H. Kidowaki, T. Oku, T. Akiyama, Fabrication and evaluation of CuO / ZnO heterostructures for photoelectric conversion, Ijrras. 13 (2012) 67–72.

[5] R. Motoyoshi, T. Oku, H. Kidowaki, A. Suzuki, K. Kikuchi, S. Kikuchi, B. Jeyadevan, Structure and photovoltaic activity of cupric oxide-based thin film solar cells, J. Ceram. Soc. Japan. 118 (2010) 1021–1023. doi:10.2109/jcersj2.118.1021.

[6] X. Zhao, P. Wang, Z. Yan, N. Ren, Room temperature photoluminescence properties of CuO nanowire arrays, Opt. Mater. (Amst). 42 (2015) 544–547. doi:10.1016/j.optmat.2014.12.032.

[7] J.A. Switzer, H.M. Kothari, P. Poizot, S. Nakanishi, E.W. Bohannan, Enantiospecific electrodeposition of a chiral catalyst, Nature. 425 (2003) 490–493. doi:10.1038/nature01990.

[8] M. Izaki, M. Nagai, K. Maeda, F.B. Mohamad, K. Motomura, J. Sasano, T. Shinagawa, S. Watase, Electrodeposition of 1.4-eV-Bandgap p-Copper (II) Oxide Film With Excellent Photoactivity, J. Electrochem. Soc. (2011). doi:10.1149/1.3614408.

[9] B.E. McCandless, S.S. Hegedus, Influence of CdS window layers on thin film CdS/CdTe solar cell performance, in: Conf. Rec. Twenty-Second IEEE Photovolt. Spec. Conf. - 1991, 1991: pp. 967–972 vol.2. doi:10.1109/PVSC.1991.169352.

[10] B. von Roedern, How do buffer layers affect solar cell performance and solar cell stability?, Mater. Res. Soc. Symp. Proc. 668 (2001) 6–6. doi:10.1557/PROC-668-H6.9.

[11] B. Samanta, D. Das, A.K. Barua, Role of buffer layer at the p/i interface on the stabilized efficiency of a-Si solar cells, Sol. Energy Mater. Sol. Cells. 46 (1997) 233–237. doi:10.1016/S0927-0248(97)80001-3.

[12] V. Shrotriya, G. Li, Y. Yao, C.W. Chu, Y. Yang, Transition metal oxides as the buffer layer for polymer photovoltaic cells, Appl. Phys. Lett. 88 (2006). doi:10.1063/1.2174093.

[13] C. Mebarkia, D. Dib, H. Zerfaoui, R. Belghit, The role of buffer layers and double windows layers in a solar cell CZTS performances, in: AIP Conf. Proc., 2016. doi:10.1063/1.4959430.

[14] N. Naghavi, S. Spiering, M. Powalla, B. Cavana, D. Lincot, High-Efficiency Copper Indium Gallium Diselenide (CIGS) Solar Cells with Indium Sulfide Buffer Layers Deposited by Atomic Layer Chemical Vapor Deposition (ALCVD), Prog. Photovoltaics Res. Appl. 11 (2003) 437–443. doi:10.1002/pip.508.

[15] M. Izaki, T. Ohta, M. Kondo, T. Takahashi, F.B. Mohamad, M. Zamzuri, J. Sasano, T. Shinagawa, T. Pauporté, Electrodeposited ZnO-nanowire/Cu_2O photovoltaic device with highly resistive ZnO intermediate layer, ACS Appl. Mater. Interfaces. (2014). doi:10.1021/am502246j.

[16] M.Z. Mohd Zamzuri, J. Sasano, F. Binti Mohamad, M. Izaki, Photon-Assisted Electrochemical Construction of <0001>-n-ZnO/<111>-p-Cu_2O Photovoltaic Devices with Intermediate TiO2 Layer, ECS Trans. 64 (2014) 21–26. doi:10.1149/06415.0021ecst.

[17] Y.S. Lee, D. Chua, R.E. Brandt, S.C. Siah, J. V. Li, J.P. Mailoa, S.W. Lee, R.G. Gordon, T. Buonassisi, Atomic layer deposited gallium oxide buffer layer enables 1.2 v open-

circuit voltage in cuprous oxide solar cells, Adv. Mater. 26 (2014) 4704–4710. doi:10.1002/adma.201401054.

[18] A. Mitra, D.A. Atwood, Polysiloxanes & Polysilanes, in: Encycl. Inorg. Chem., 2006. doi:doi:10.1002/0470862106.ia201.

[19] B. Rieger, M. Grübel, S.U.H. Heidsieck, Polysilanes, Polycarbosilanes, Dioxadisilacyclohexane, and Polysiloxanes, in: Effic. Methods Prep. Silicon Compd., 2016: pp. 275–293. doi:10.1016/B978-0-12-803530-6.00023-8.

[20] R.D. Miller, J. Michl, Polysilane High Polymers, Chem. Rev. 89 (1989) 1359–1410. doi:10.1021/cr00096a006.

[21] M.A. Brook, Silicon in organic, organometallic, and polymer chemistry, 2000. doi:10.1002/1097-0126(200102)50:2<256::AID-PI619>3.0.CO;2-3.

[22] F. Ebisawa, T. Kurokawa, S. Nara, Electrical properties of polyacetylene/polysiloxane interface, J. Appl. Phys. 54 (1983) 3255–3259. doi:10.1063/1.332488.

[23] D. Cai, A. Neyer, R. Kuckuk, H.M. Heise, Raman, mid-infrared, near-infrared and ultraviolet-visible spectroscopy of PDMS silicone rubber for characterization of polymer optical waveguide materials, J. Mol. Struct. 976 (2010) 274–281. doi:10.1016/j.molstruc.2010.03.054.

[24] Y. Nakayama, S. Nonoyama, T. Dohmaru, L. Han, Photoluminescence study in photooxidation of poly(phenymethylsilane) films, Solid State Commun. 92 (1994) 591–593. doi:10.1016/0038-1098(94)90149-X.

[25] P. Trefonas, R. West, R.D. Miller, Polysilane High Polymers: Mechanism of Photodegradation, J. Am. Chem. Soc. 107 (1985) 2737–2742. doi:10.1021/ja00295a028.

[26] P.D. James Speight, ELECTRON AFFINITY, in: Lange's Handb. Chem. Sixt. Ed., McGraw Hill Professional, Access Engineering, 2005.

https://www.accessengineeringlibrary.com:443/browse/langes-handbook-of-chemistry-sixteenth-edition/ch01lev1sec06.

[27] M. Izaki, Effects of annealing on optical and electrical characteristics of p-type semiconductor copper (II) oxide electrodeposits, Thin Solid Films. 520 (2012) 2434–2437. doi:10.1016/j.tsf.2011.10.018.

CHAPTER 4

Characterization of Directly Stacked (GZO/Cu_2O/CuO) Prepared by Electrodeposition and Low-Temperature Annealing in Air

4.1 Introduction

In the previous Chapter 2 and Chapter 3, Cu_2O PV and CuO PV have been discussed. Here, integrating both copper oxide layers simultaneously as the light-absorbing layer as a strategy to realize high-performance PV is investigated and characterized. The Cu_2O and CuO are p-type-semiconductors with the bandgap energies of 2.0 eV and 1.4 eV, and they both have been employed as photoactive layer of the photovoltaic layers with n-ZnO in oxide solar cells

and photocathodes in photo-electrochemical water splitting system[1], due to the large light-absorption coefficient, high abundance, low cost, and low toxicity.

Nonetheless, to realize a high-power-conversion-efficiency photoactive layer, a light-absorbing layer consisting of only Cu_2O is inadequate, since its bandgap energy indicates its inability to absorb the infrared range of the light spectrum, as discussed in Chapter One. The relatively simplistic and energy-saving fabrication of this internally-stacked structure can be achieved by electrodeposition followed by partial surface oxidation by low-temperature annealing in air as patented by Izaki *et al.*[2], and such structure of Cu_2O/CuO has been reported to be superior in hydrogen evolution reaction compared to single Cu_2O or CuO layer.[3]

We have reported the importance of microstructural changes in relation to defects when heated in vacuum which affects phase transition and the photovoltaic performance, especially the external quantum efficiency (EQE) and short-circuit current density (J_{sc}) in Chapter One. General improvements in both EQE and J_{sc} were observed in Cu_2O photovoltaic devices under optimum annealing temperature of around 423 K while annealing at higher temperatures in vacuum resulted in the reduction of Cu_2O to metallic Cu at the surface near the grain boundaries accompanied by the formation of defects (nanopores) in the bulk. We also reported the ability to CuO layer to function as the light-absorbing layer in Chapter 3. On the other hand, when heated in air, the formation of internally-stacked Cu_2O/CuO with retaining lattice relationship naturally prompts a different occurrence in the EQE spectrum. Here, we prepare the internally-stacked CuO/Cu_2O photoactive layers by the electrodeposition of Cu_2O layer followed by heating in air and characterize the structure, optical property, and electrical properties including the external quantum efficiency with a change in biased voltages for the internally-stacked CuO/Cu_2O photoactive layers.

4.2 Experimental Procedures

4.2.1 Electrodeposition of GZO/Cu_2O

Conductive gallium-doped zinc oxide (GZO)-coated glass (Geomatech) were used as the substrates due to its capability to demonstrate the EQE behavior of the Cu_2O without any intermediary layer. Electrodeposition of Cu_2O layers from an alkaline aqueous solution (pH = 12.5) containing 0.4 mol L^{-1} copper (II) acetate monohydrate ($Cu(CH_3COO)_2 \cdot H_2O$, Nacalai Tesque, Inc.) 3 mol L^{-1} lactic acid (Kanto Chemical, Co., Inc.). A standard 3-electrode-cell was used similarly to the ZnO electrodeposition method discussed in Chapter 2, with a Pt plate as a counter electrode and Ag/AgCl in saturated KCl as a reference electrode.[4] The electrodeposition potential was set at −0.4 V and at an electric charge of 1.5 C cm^{-2} in a water bath temperature of 336 K.

4.2.2 Fabrication of GZO/Cu_2O/CuO

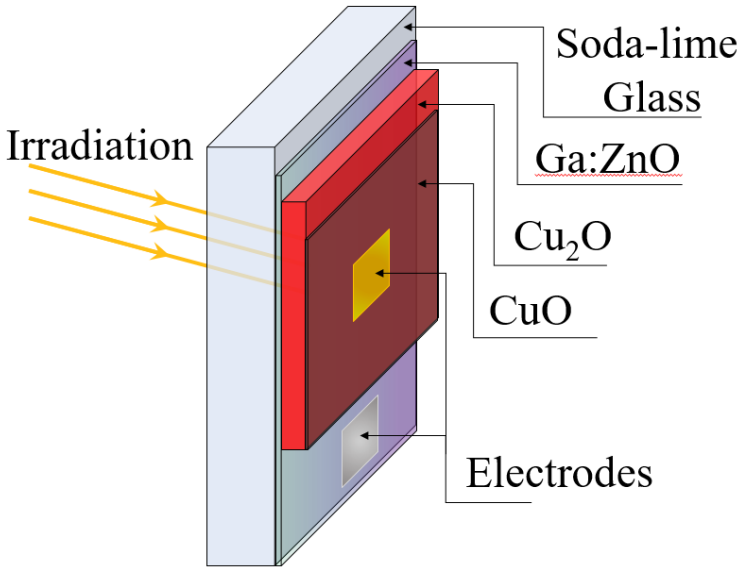

Figure 4.2.1. Schematics of the electrodeposited and annealed GZO/Cu_2O/CuO photoactive diode.

A representative schematics of the GZO/Cu_2O/CuO layer is shown in **Fig 4.2.1**. Electrodeposited Cu_2O layers were placed on an alumina plate in a quartz holder, then annealed to temperatures of 473, 523, 573, and 673 K in a rapid thermal annealing furnace (MILA

5000).[2] Annealing rate was set at 10 K s^{-1}, and the heating time was set at 60 min when target temperature had been reached. The devices were then let to cool to room temperature before further evaluation.

4.2.2 Characterization of Cu_2O/CuO directly-stacked photoactive layer

An x-ray Diffractometer (XRD, Rigaku RINT 2500) was used to measure the XRD spectra and was operated at 20 kV and 10 mA using Cu Kα radiation. A field emission scanning electron microscope (FE-SEM, Hitachi High Technology SU8000) was used for observation of surface and cross-sectional morphology. UV-Vis measurement was carried out by a UV-Vis-NIR spectrophotometer (Hitachi High-Technology UV-4100) with an integrating sphere. Calibration was carried out on standard test cells before the measurements. The external quantum efficiencies were evaluated using a monochromator (Bunko Keiki, SM-250KB). The electrodes used by the photovoltaic devices used for the EQE measurements were fabricated by thermal evaporation. A light mask was used to define the active areas of 4 mm^2 during irradiation for measurements. Low reversed biased voltages of -0.001 to -0.01V were applied to the 523-K-device for further investigation of its EQE behavior.

4.3 Results and Discussion

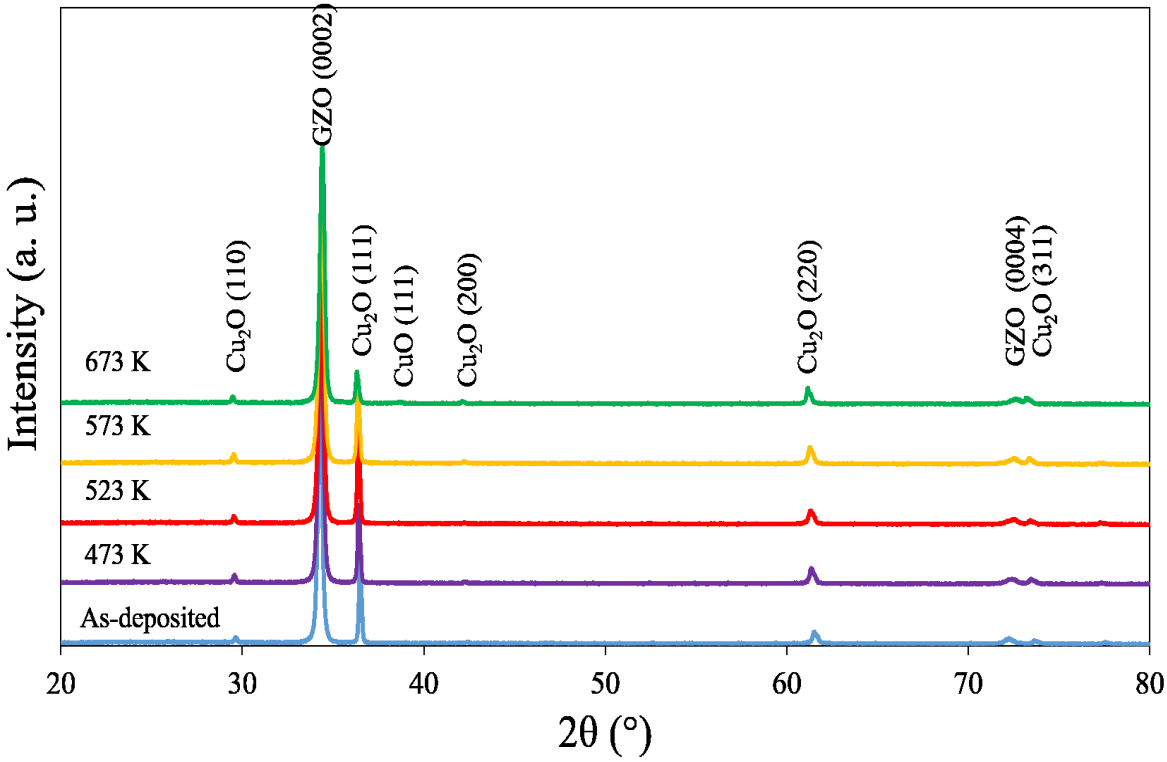

Figure 4.3.1. X-ray diffraction patterns for the Cu_2O layer before and after annealed at 523, 573 and 673 K

Fig. 4.3.1 shows the X-ray diffraction patterns for the Cu_2O layer before and after annealed at 473, 523, 573 and 673 K. All peaks observed were assigned to the hexagonal wurtzite GZO substrate and the deposited cubic cuprite Cu_2O, except for the 673K-annealed Cu_2O layer which showed an extra faint peak that was assigned to the (111) plane of CuO at 38.7°. The highest peaks shown here were assigned to the (0001) planes of the GZO substrates. All Cu_2O layer possessed a <111>-out-of-plane orientation which could be observed from the peaks at 36.4°, irrespective of the annealing temperature. The lattice constant of the Cu_2O phase was estimated to be 0.428 nm and was close to the standard value of 0.427 nm. Although for the 673 K-annealing, its belonging peak appeared weakened. The appearance of (111) CuO is

thought to be somehow related to the weakening of the (111) Cu_2O peak. It was impossible to calculate the lattice constants of the CuO phase, because of the monoclinic lattice.

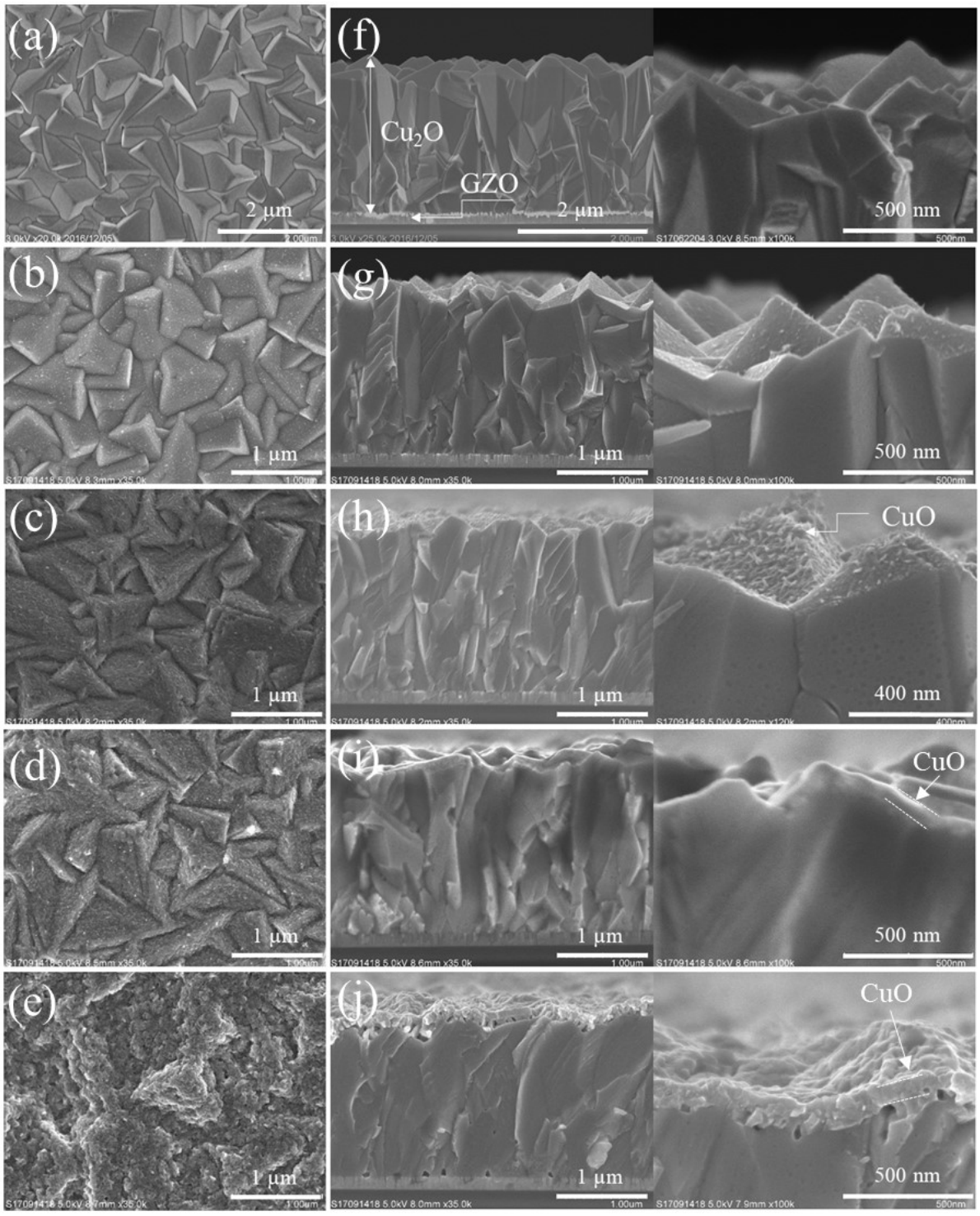

Figure 4.3.2. FE-SEM images of surface and cross-sectional images: (a)(f) as-deposited, annealed at (b)(g) 473, (c)(h) 523, (d)(i) 573, (e)(j) 673 K. Images on the right are magnified cross-sectional images near the surface.

Fig. 4.3.2 shows the FE-SEM images of the Cu_2O layer (as-deposited) and Cu_2O/CuO layers prepared by annealing temperatures of 473, 523, 573 and 673 K. The total thickness was almost constant at approximately 2 μm for the Cu_2O layer before and after annealing. The Cu_2O layer was composed of aggregates of three-sided pyramids grains with the smooth top surface and approximately 1.5 μm in size, and from the cross-sectional images, continuous Cu_2O columnar grain aggregates can be seen forming on the GZO substrate. The 473-K-device possessed a similar morphology and structure with the as-deposited device. However, small CuO granular grains with the size of approximately 13 nm were formed on the three-sided pyramids grains of the 523 K-annealed Cu_2O layer, and the continuous CuO layer was formed on the grain surface and grain boundary. The CuO grain size increased to 23 nm and 62 nm, with the increase in the annealing temperature to 573K and 673K. The 673 K-annealed Cu_2O layer showed fine CuO grains with diminishing pyramidal shape. Magnified images shown in the middle column indicated the close relationship between CuO thickness and the annealing temperature. The thicknesses of the CuO layer were averaged to be approximately 23, 44 and 278 nm at annealing temperatures of 523, 573 and 673 K respectively. For 523 and 573 K, nanopores and voids along the Cu_2O grain boundaries could also be observed along with the formation of CuO at the surface. The surface roughness (Ra) of the CuO was measured using laser microscopy. The CuO surface Ra values measured are 0.07, 0.04 and 0.05 μm for CuO prepared at 523, 573 and 673 K respectively. These values were similar to that of the as-deposited Cu_2O layer of 0.06 μm as reported in the previous Chapter. This shows that annealed CuO layers were much smoother and contained lesser surface irregularities compared to the electrodeposited CuO, which Ra value was 0.28 μm.

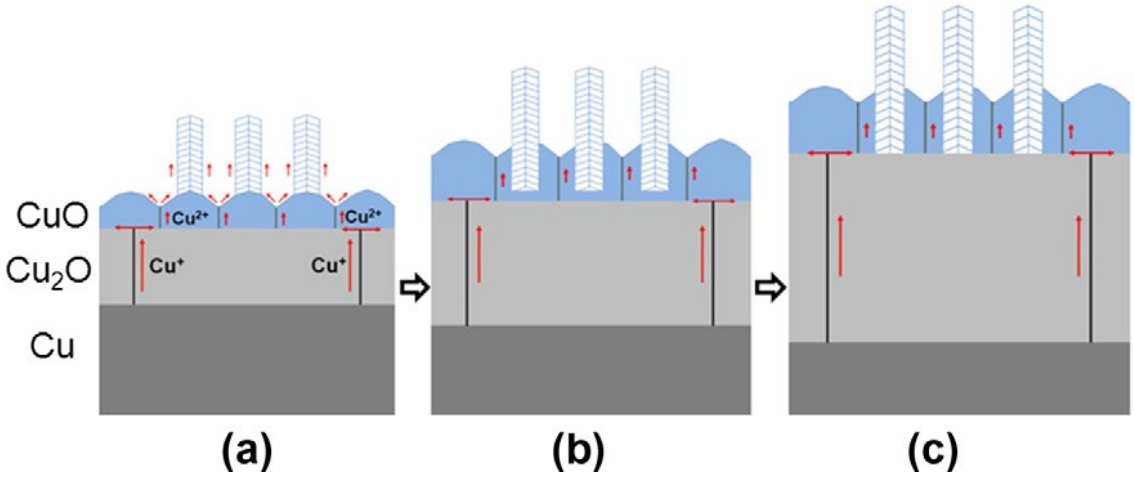

Figure 4.3.3. (a) Initial growth of CuO nanowires (NWs) on the outer surface of CuO grains; (b) growth of the CuO substrate gradually buries the root of the NWs; (c) continued decomposition of the CuO layer at the CuO/Cu_2O interface leading to the direct contact between the NW roots and the Cu_2O layer.[5]

The mechanism of CuO growth is important to understand the resulting morphology observed. Yuan *et al.* described the driving force and growth mechanism for the CuO formation, as shown in **Figure 4.3.3**.[5] At low oxidation temperature of 523~573 K, the observed nanopores along the grain boundaries were attributed to the outward diffusion of Cu cations along the grain boundaries, which contributed to the formation of CuO at the surface. In an oxygen-poor atmosphere, the formation of metallic Cu occurs instead, as reported in Chapter 2, which corresponded to this growth mechanism. This is similar to the mechanism as described in the Kirkendall effect during metal oxidation.[6–8] At a higher annealing temperature of 673 K, the dramatically increased CuO thickness was accompanied by a multitude of voids in the CuO layer and the magnified cross-sectional image in **Fig. 4.3.2 (e)** indicates formation akin to the roots of CuO whiskers (nanowires) as reported by Yuan *et al.* and Zhu *et al*, [5,9] although the annealing condition of the CuO did not yet favor the growth and formation of CuO NWs and thus not observed in **Fig. 4.3.2.**

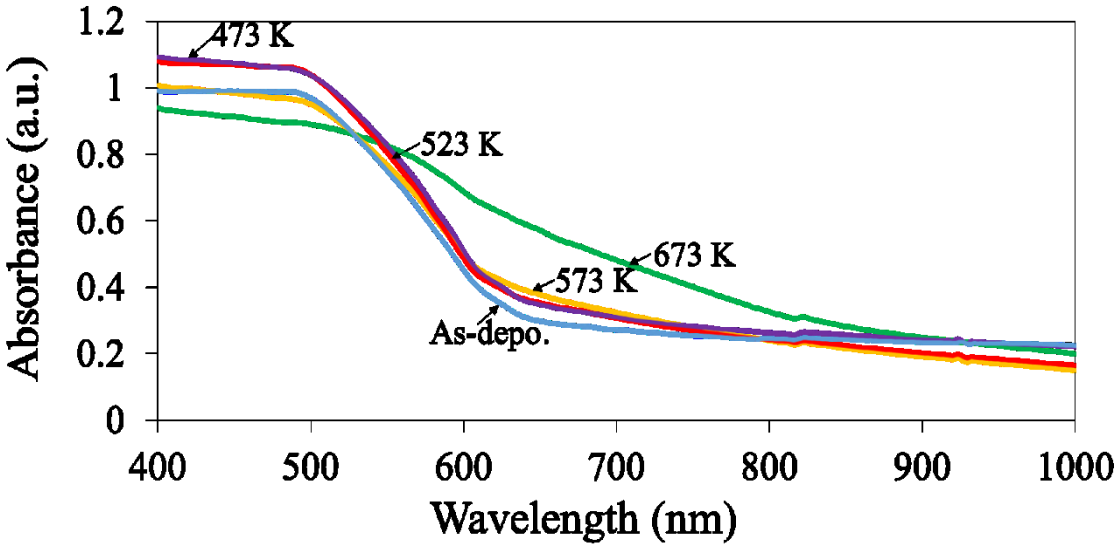

Figure 4.3.4. UV-Vis measurement of the absorbance of layers as-deposited, and annealed at 473, 523, 573, and 673 K.

Optical absorption spectra for the Cu_2O layer before and after annealing at 523 K, 573 K, and 673 K were shown in **Figure 4.3.4**. The Cu_2O possesses a characteristic absorption edge at 650 nm with a corresponding bandgap energy of 2.1 eV, which grants its brownish-red appearance, which can be observed in the as-deposited Cu_2O layer. The increase in absorbance in the range from 530 to 800 nm can also be observed clearly with the increase in annealing temperature. This is in agreement with the formation and thickening of CuO formed on the surface of Cu_2O layer, which can be related to the higher-wavelength absorption edge and the change of color of the layers into blackish-brown after annealing. At 673 K, the appearance of an absorption edge at approximately 850 nm was attributed to the absorption edge of CuO.

. **Figure 4.3.5** shows the Tauc plots of $(\alpha h\nu)^2$ and $(\alpha h\nu)^{1/2}$ versus $h\nu$ for the 673 K-annealed device. The relationship between optical bandgap energy, E_g and the absorption coefficient α calculated from the absorbance and thickness can be represented by Eq. 1 as follows[10]:

$$\alpha h\upsilon = A(h\upsilon - E_g)^{n/2} \quad (1)$$

A is a constant, *h*υ is photon energy, for thin films n=1 for a direct transition, and n=4 for an indirect allowed transition. The direct bandgap estimated from this figure is 1.56 eV, while the indirect bandgap is 1.47 eV which are close to reported CuO direct bandgap values by Nakaoka *et al*. of 1.56 eV and 1.45 eV which were heat-treated at 573 and 773 K respectively.[10] However, the actual type of bandgap energy of CuO remains controversial.[11–16]

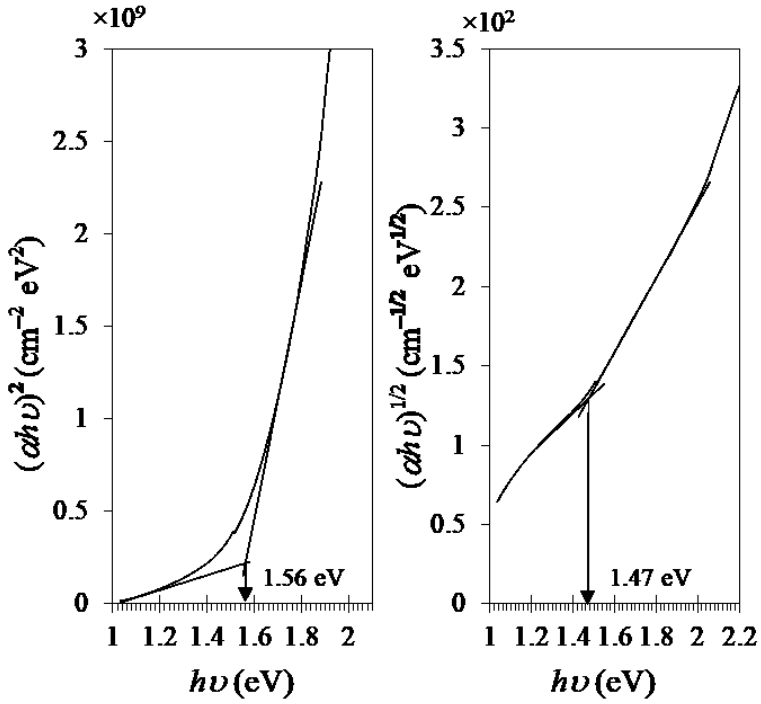

Figure 4.3.5. Tauc plots of $(\alpha h\nu)^2$ and $(\alpha h\nu)^{1/2}$ versus $h\nu$, for direct and indirect calculation of the bandgap energy of the 673 K device

External quantum efficiency (EQE) is an important evaluation that shows the ratio of the number of charge carriers collected by the photovoltaic to the number of photons in the photoactive layer. **Figure 4.3.6** shows the EQE of devices: as-deposited, annealed at 473, 523, 573, and 673 K. Both devices for as-deposited and annealed at 473 K both display charge collection originated from Cu_2O layers which shows the characteristic absorption edge at around 650 nm and peaks at 44% and 43% at around 400 nm, corresponding to the UV-Vis

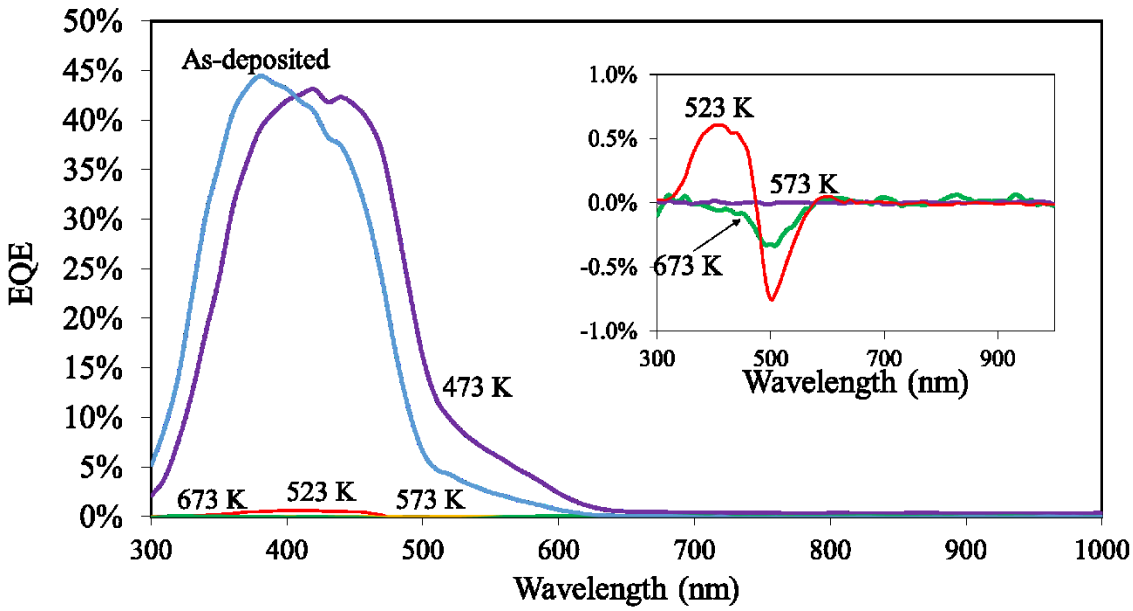

Figure 4.3.6. External quantum efficiency spectra of devices: as-deposited, and annealed at 473, 523, 573, and 673 K. Shown inset is the same spectra of devices annealed at 523, 573 and 673 K, with a magnified scale on the EQE values.

results in **Figure 4.3.4**. The EQE values were low compared with that of GZO/n-ZnO/Cu_2O structure shown in Chapter 2, so the insertion of the n-ZnO was proved effective to enhance the photovoltaic performance. Starting at the annealing temperature of 523 K, the EQE deteriorates significantly. However, at the same time, peculiar EQE behaviors were also observed in devices prepared in 523, 573 and 673 K, as shown in the inset of **Figure 4.3.6**.

By definition, the quantum efficiency is the probability of an incident photon of energy delivering one electron to the external circuit. The total area below the EQE curve then represents the total photocurrent density delivered to the external circuit and the relationship between the short-circuit current density, J_{SC} and the quantum efficiency, $QE(E)$ can be written as **Eq.4.2** as shown below, where q is the electron charge, and $b_s(E)$ the incident spectral photon flux density.[17]

$$J_{SC}=q\int b_s(E)QE(E)dE \qquad \textbf{(4.2)}$$

The deterioration of overall EQE is understandable, given that the increase of annealing temperature in devices fabricated with this method can be attributed to the decrease in carrier mobility, due to the formation of defect structures such as nanopores observed in the FE-SEM. This apparently occurred both when annealed in vacuum and in air, which includes the diffusion of Cu cations during oxidation and reduction from Cu_2O as reported in Chapter 2. As such, the overall decrease of EQE was natural when annealed in air at 523, 573 and 673 K as compared to the single layer Cu_2O. Another contributing factor that led to the diminishing EQE performances when annealed at these temperatures is the intolerance of the GZO substrate layer, which showed increased resistance when annealed at temperatures above 473 K as shown in **Figure 4.3.7.**

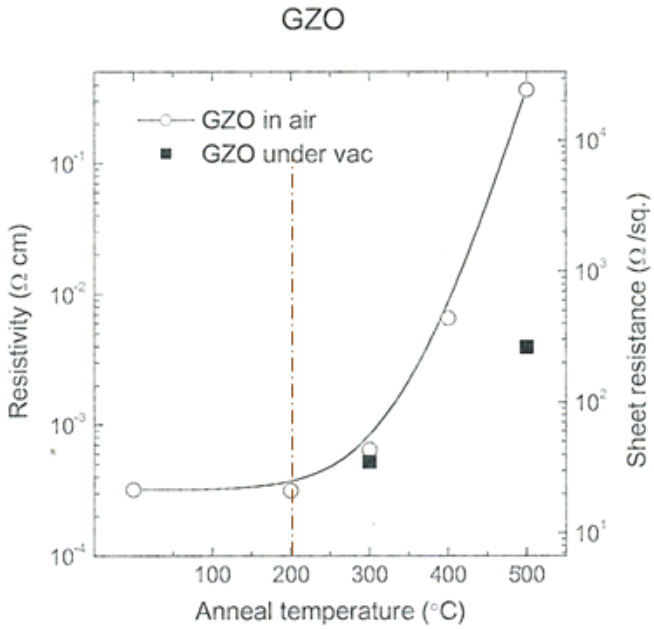

Figure 4.3.7. GZO substrate electrical properties under different annealing temperatures

However, the negative region of EQE demonstrated especially by the 523-K-device would mean the charge carrier generated in this region flowed in an opposite way compared to the charge carriers generated in devices prepared at lower temperatures or as-deposited. Thus, to

clarify the mechanism of the strange EQE behavior, further investigations were made by applying low reversed biased voltages.

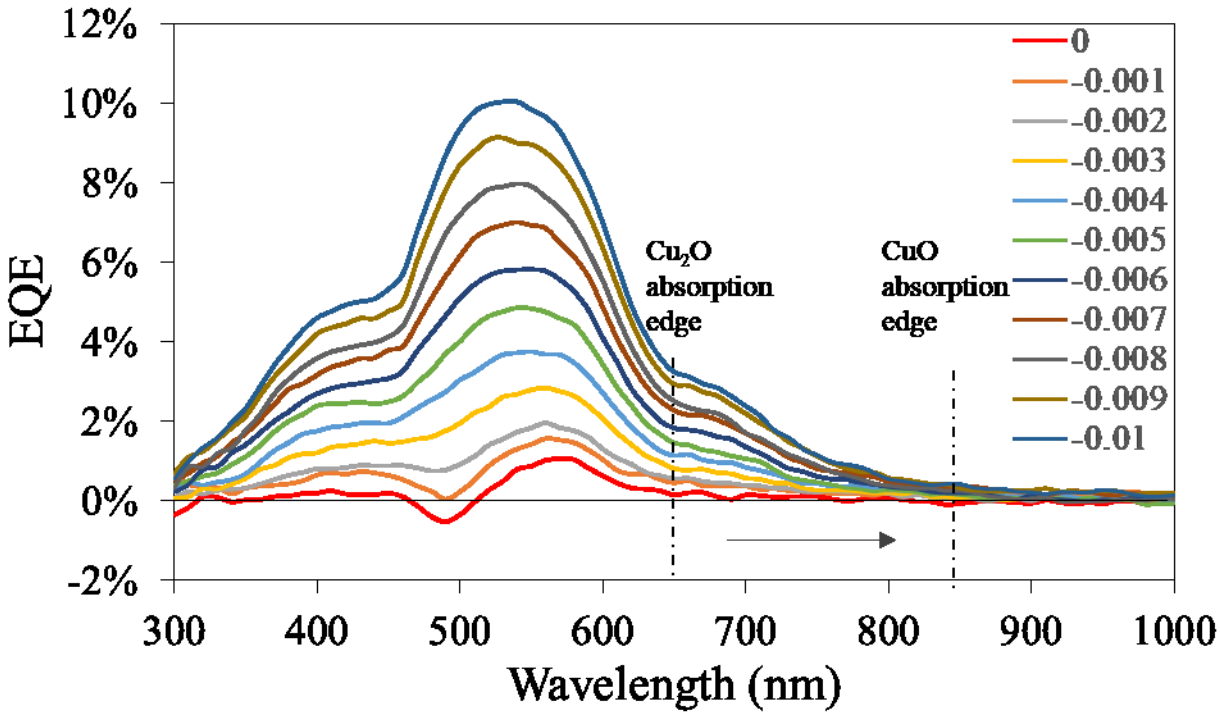

Figure 4.3.8. EQE spectra of devicess annealed at 523 K under biased voltage of 0 to 0.1 V.

Figure 4.3.8 shows the EQE spectra for devices annealed at 523 K under biased voltages of 0 V to -0.01 V with increments of -0.001 V. The negative regions were suppressed, and instead, EQE values increased. Also, a new absorption edge for the 523 K appeared around 850 nm. Without any biased voltage applied (0 V), the 523-K-prepared internally-stacked photoactive layer showed a peak at approximately 410 nm and a dip in the spectra towards the negative region around 500 nm, indicating two distinct charge transportations from different light-absorbing layers. The peak at 410 nm can be attributed to the characteristic EQE peak of electrodeposited Cu_2O as already reported in Chapter 2. Based on the as-deposited EQE curve, we assume that prior to annealing, all charge collected can be attributed to the flow from photo-induced (starting from 650 nm) electrons from the Cu_2O layer towards the direction of the source of irradiation and extracted via the GZO layer. For the 523-K-device, the dip towards

the negative region in the EQE spectra within 470 and 580 nm then reveals the presence of photo-induced electrons moving in the opposite direction. The increment of reverse biased voltages by 0.001 V towards −0.01 V caused a dramatic increase in the 550-nm-peak, while the increase in the peak at around 410 nm was gradual in comparison. This also indicates that the charge collection as represented by these peaks were constituted by charges originating from more than one light-absorbing layer, which were the Cu_2O and CuO layer. Also, a distinct absorption edge for the peak of 550 nm at around 850 nm emerged. This absorption edge can be attributed to the characteristic absorption edge of CuO, as can clearly be seen from the absorption spectra (**Figure 4.3.4**) of the 673 K device, which among the devices, possesses the thickest layer of CuO at the surface as observed in **Figure 4.3.2.** This behavior of dipping of the EQE curve towards the negative region was not observed when annealed in vacuum in the same temperature, even though the Cu_2O was prepared in a similar manner, as described in Chapter 2. This means that the EQE behavior is specific to devices annealed in air which can be attributed to the appearance of Cu_2O/CuO internally-stacked layer.

This is significant due to the observed absorption edge of Cu_2O at 650 nm and the absorption edge of CuO which extends towards higher wavelengths at approximately 850 nm. This shows that despite the presence of defects and the thinness of the CuO, carrier charge was generated and collected from the CuO layer under illumination. The expansion of absorption demonstrates that with careful fabrication, the directly-stacked Cu_2O/CuO photoactive layers can act in tandem as light-absorbing layers. The electric field was formed at the heterointerface of GZO/Cu_2O due to the ohmic contact between the Cu_2O/Au interface. And the penetration depth of light irradiated from the GZO side increased with the wavelength, and the electron generated in the deep part of the Cu_2O layer could be taken out by applying the biased voltage. It was speculated at this point that for annealed Cu_2O layer, electric fields were formed at both

heterointerfaces of GZO/Cu_2O and Cu_2O/CuO, causing the appearance of positive and negative regions as shown in **Figure 4.3.6.**

4.4 Summary

The EQE of the internally-stacked Cu_2O/CuO layers and their changes under different low reversed biased voltage was shown. The EQE result clearly demonstrates that both oxide layers acted as the light-absorbing layer, and showed the validity of copper-oxide-based photoactive layer in terms of augmented absorption span. For the 523 K device, more photo-induced electrons produced in the CuO layer were being swept towards the source of irradiation under low reverse biased voltage, which resulted in a dramatic increase in the 550-nm-peak and the appearance of the CuO absorption edge at 840 nm. The results also highlight the importance of the semiconductor condition of the layers with minimal defects to realize a high-performing photoactive layer. The EQE behavior shows the need to investigate the band alignment, and the band profiles should be optimized, based on the band alignment.

REFERENCES

[1] M.G. Walter, E.L. Warren, J.R. McKone, S.W. Boettcher, Q. Mi, E.A. Santori, N.S. Lewis, Solar water splitting cells, Chem. Rev. 110 (2010) 6446–6473. doi:10.1021/cr1002326.

[2] M. Izaki, K. Fukuzawa, Photovoltaic layer and the preparation process, 2017–54917, n.d.

[3] Y. Yang, D. Xu, Q. Wu, P. Diao, Cu_2O/CuO Bilayered Composite as a High-Efficiency Photocathode for Photoelectrochemical Hydrogen Evolution Reaction, Sci. Rep. 6 (2016) 35158. doi:10.1038/srep35158.

[4] M. Izaki, T. Omi, Transparent zinc oxide films prepared by electrochemical reaction, Appl. Phys. Lett. (1995) 2439. doi:10.1063/1.116160.

[5] L. Yuan, Y. Wang, R. Mema, G. Zhou, Driving force and growth mechanism for spontaneous oxide nanowire formation during the thermal oxidation of metals, Acta Mater. 59 (2011) 2491–2500. doi:10.1016/j.actamat.2010.12.052.

[6] A.A. El Mel, R. Nakamura, C. Bittencourt, The Kirkendall effect and nanoscience: Hollow nanospheres and nanotubes, Beilstein J. Nanotechnol. (2015). doi:10.3762/bjnano.6.139.

[7] J. Liu, D. Xue, Thermal oxidation strategy towards porous metal oxide hollow architectures, Adv. Mater. 20 (2008) 2622–2627. doi:10.1002/adma.200800208.

[8] S. Choopun, N. Hongsith, E. Wongrat, Metal-Oxide Nanowires by Thermal Oxidation Reaction Technique, in: Nanowires, InTech, 2010. doi:10.5772/39506.

[9] Y. Zhu, K. Mimura, M. Isshiki, Oxidation Mechanism of Copper at 623-1073 K, Mater. Trans. 43 (2002) 2173–2176. doi:10.2320/matertrans.43.2173.

[10] K. Nakaoka, J. Ueyama, K. Ogura, Photoelectrochemical Behavior of Electrodeposited CuO and Cu_2O Thin Films on Conducting Substrates, J. Electrochem. Soc. 151 (2004) C661. doi:10.1149/1.1789155.

[11] F.P. Koffyberg, F.A. Benko, A photoelectrochemical determination of the position of the conduction and valence band edges of p-type CuO, J. Appl. Phys. 53 (1982) 1173–1177. doi:10.1063/1.330567.

[12] M. Heinemann, B. Eifert, C. Heiliger, Band structure and phase stability of the copper oxides Cu_2O, CuO, and Cu_4O_3, Phys. Rev. B - Condens. Matter Mater. Phys. 87 (2013) 3–7. doi:10.1103/PhysRevB.87.115111.

[13] C. Rödl, F. Sottile, L. Reining, Quasiparticle excitations in the photoemission spectrum of CuO from first principles: A GW study, Phys. Rev. B - Condens. Matter Mater. Phys. 91 (2015). doi:10.1103/PhysRevB.91.045102.

[14] Q. Zhang, K. Zhang, D. Xu, G. Yang, H. Huang, F. Nie, C. Liu, S. Yang, CuO nanostructures: Synthesis, characterization, growth mechanisms, fundamental properties, and applications, Prog. Mater. Sci. 60 (2014) 208–237. doi:10.1016/j.pmatsci.2013.09.003.

[15] C.E. Ekuma, V.I. Anisimov, J. Moreno, M. Jarrell, Electronic structure and spectra of CuO, Eur. Phys. J. B. 87 (2014) 1–6. doi:10.1140/epjb/e2013-40949-5.

[16] D. Wu, Q. Zhang, M. Tao, LSDA+U study of cupric oxide: Electronic structure and native point defects, Phys. Rev. B - Condens. Matter Mater. Phys. 73 (2006). doi:10.1103/PhysRevB.73.235206.

[17] S.M. Sze, K.K. Ng, Physics of Semiconductor Devices, 3rd ed., John Wiley & Sons, Inc., Hoboken, NJ, USA, 2006. doi:https://doi.org/10.1002/9780470068328.ch13.

CHAPTER 5

The X-ray Photoelectron Spectroscopic Analysis and the Band Alignment Study of Directly Stacked Copper Oxide PV (GZO/Cu_2O/CuO)

5.1 Introduction

In the previous Chapter, successfully fabricated directly stacked GZO/Cu_2O/CuO was described, and the EQE performances were discussed. The light-absorbing layer properties of Cu_2O and CuO were demonstrated. EQE in the negative region was demonstrated especially

by the 523-K-device without any biased voltage, along with the positive region, which indicated that there might be two distinct charge transportation and that electric fields were formed at the heterointerfaces of GZO/Cu_2O and Cu_2O/CuO. The charge transportation was controlled by somehow unifying them when low reversed biased voltages were applied, which also showed the emergence of an absorption edge characteristic to the properties of a CuO layer. While the photoactivity of the CuO layer was demonstrated, it was concluded that it was necessary to further investigate the band alignment, which can be done by using X-ray photoelectron spectroscopy (XPS) to elucidate the EQE behavior. This might prove useful in understanding the energy state and proposing an ideal band profile. It has been deployed in many reports describing Cu_2O-based heterostructures.[1–5] The valence band maximum of the light absorbing layers can be directly measured, and the band alignment schematics can be drawn based on the optical bandgap calculated from the Uv-vis measurement. Additionally, XPS is a useful characterization tool that can supplement extra information such as chemical state determination, and accurate identification of the fabricated copper oxides, which were difficult to evaluate using XRD such as shown in Chapter 2 and Chapter 4, due to the thinness of the CuO. These are essential for the characterization of the chemistries involved with thin oxide film growth.[6] However, it is known that the analysis of copper species is challenging because of the complexity and overlapping binding energies for different species.[7]

Here, the XPS analysis is carried out and the chemical state of the layers will be investigated to give further information of the Cu species, deploying methods such as the Auger parameter and the Wagner plot to accurately characterize the Cu_2O and CuO films.[8] And mainly, an attempt to calculate and construct the schematics of the band alignments of the GZO/Cu_2O/CuO will be made, which will be used to further explain its EQE behavior as described in Chapter 4, and an ideal band alignment will be proposed based on the study.

5.2 Experimental Procedures

A similar fabrication technique mentioned in the previous chapter was used. Conductive gallium-doped zinc oxide (GZO)-coated glass (Geomatech) were used as the substrates due to its capability to demonstrate the EQE behavior of the Cu_2O without any intermediary layer. Electrodeposition of Cu_2O layers from an alkaline aqueous solution (pH = 12.5) containing 0.4 mol L^{-1} copper (II) acetate monohydrate ($Cu(CH_3COO)_2 \cdot H_2O$, Nacalai Tesque, Inc.) 3 mol L^{-1} lactic acid (Kanto Chemical, Co., Inc.). A standard 3-electrode-cell was used, with a Pt plate as a counter electrode and Ag/AgCl in saturated KCl as a reference electrode. The electrodeposition potential was set at −0.4 V and at an electric charge of 1.5 C cm^{-2} in a water bath temperature of 336 K. Electrodeposited Cu_2O layer were placed on an alumina plate in a quartz holder, then annealed to temperature of 523, 573, and 673 K in a rapid thermal annealing furnace (MILA 5000). Annealing rate was set at 10 K s^{-1}, and the heating time was set at 60 min when target temperature had been reached.

The devices were then let to cool to room temperature before the X-ray photoelectron spectroscopy (XPS) measurement was carried out. The XPS measurement was made with a scanning X-ray microprobe (Quantera SXM-CI) made by ULVAC-PHI Inc, with a 24.8 W monochrome Al $K\alpha$ (1486.6 eV) with beam diameter of 100 μm. Neutralizer was operated at 1.0 V of 20.0 μA at all measurements, to lessen the drift caused by charge-up. A conventional peak shift correction of C 1s to the binding energy of 284.8 eV was carried out. For the band-alignment calculation, measurement using the depth profile mode was made with an interval of 18 seconds for 3 minutes.

The software used for the analyses is CasaXPS (Casa Software Ltd.). For fitting, Gaussian-Lorentzian profiles defined in CasaXPS as GL(x) were used. It should be noted that the varying GL(x) does not constitute to large peak area changes, and such profiles used are to compare with reported values in past literature.[7,9]

5.3 Results and Discussion

5.3.1 X-ray Photoelectron Spectroscopy

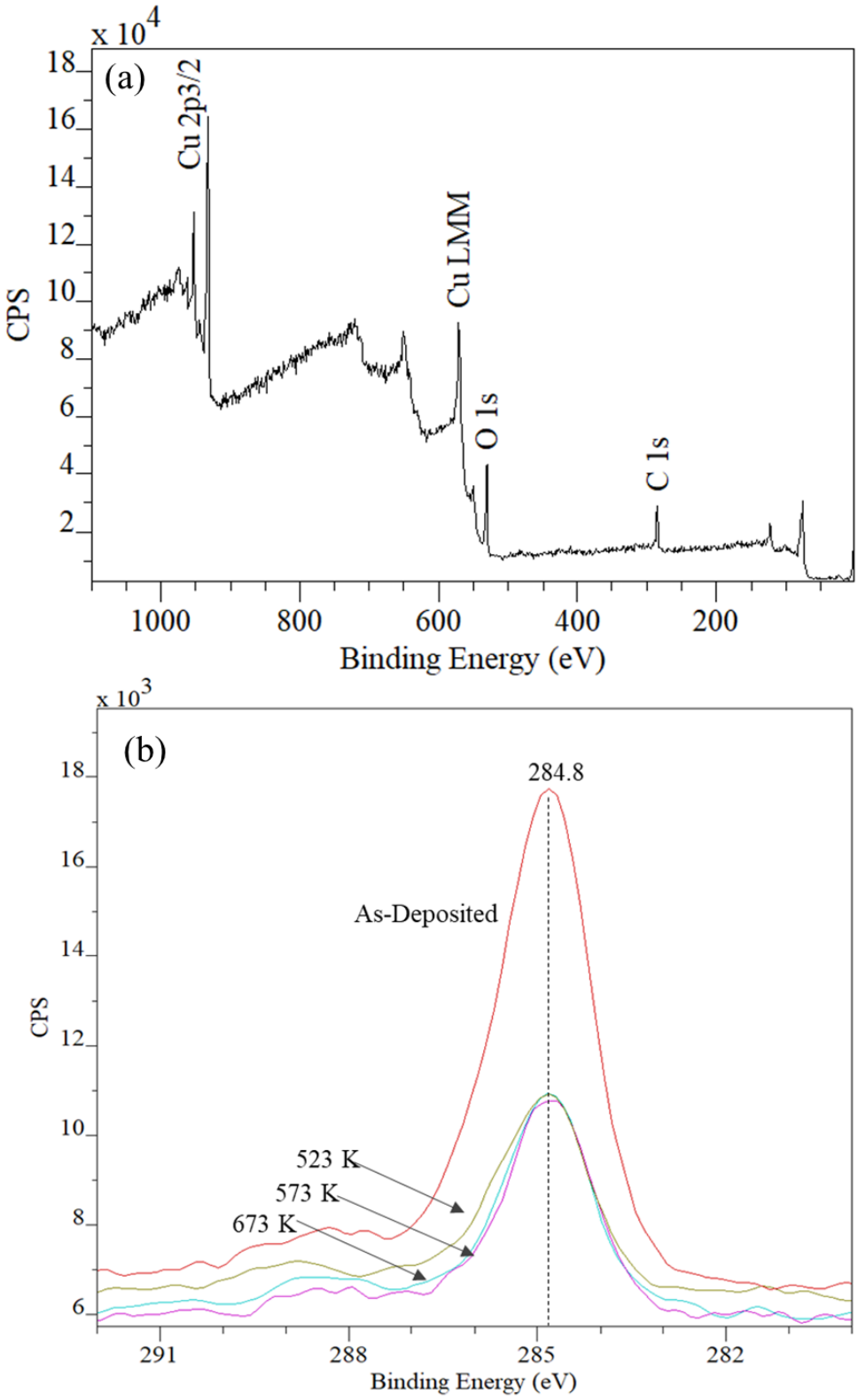

Figure 5.3.1. XPS spectra for (a) representative spectra showing surveyed

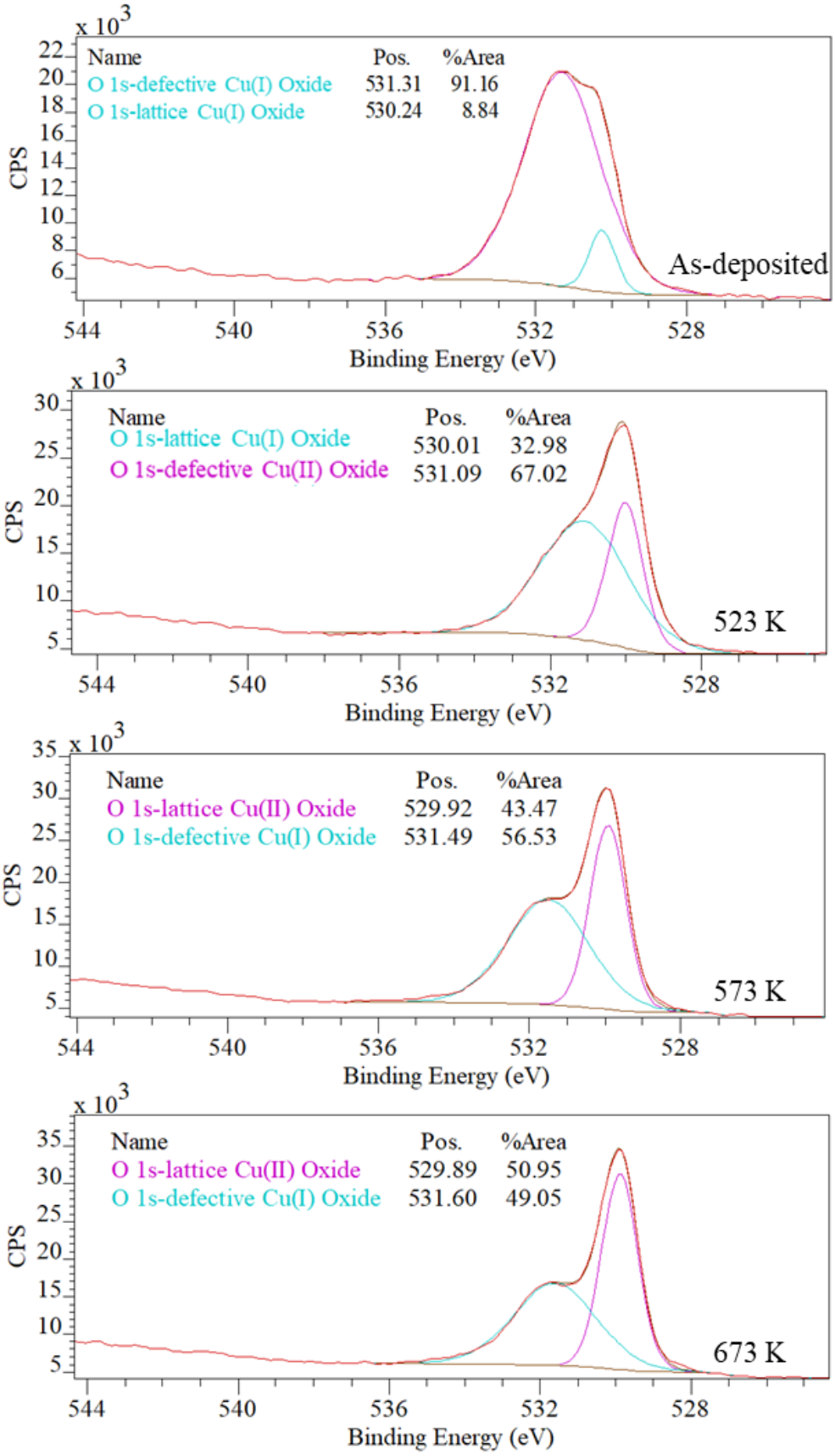

Figure 5.3.2. Fitting of O 1s spectra of as-deposited, 523 K, 573 K, and 673 K.

Figure 5.3.1 shows a surface XPS spectra surveyed for C 1s, O 1s, Cu $2p_{3/2}$ and Cu $L_3M_{4,5}M_{4,5}$ for the as-deposited device. No pre-sputtering was carried out to retain surface information. Peak shifts were corrected to 284.8 eV of adventitious C 1s spectral component (C-C, C-H) as shown in (b).[10] However, the intensity of the C 1s peaks reduces after annealing as can be seen, which caused complexity in the C 1s peak shift. All the peaks could be identified as photoelectron and Auger electron peaks originated from Cu, O, and C.

Figure 5.3.2 shows the O 1s spectra and the convoluted peaks fitted to the spectra. The as-deposited O 1s spectra consist of two peaks at 530.2 eV and 531.3 eV. The first peak can be attributed to the O 1s lattice oxide for Cu_2O at the reported peak of 530.2 eV. However, the second peak is ambiguous as it is near and can be assigned to the Cu(II) hydroxide ($Cu(OH)_2$) at a reported value of 531.2 eV. Another possibility is that this higher peak belongs to defective Cu_2O components at a reported value of 531.6 eV.[9,11,12] The peaks of 523 K are 530 and 531.1 eV, while peaks of 573 K are 529.9 and 531.5 eV. Lastly, the peaks of 673 K are 529.9 and 531.6 eV. All these peaks are very close to each other and may be ascribed to either lattice oxide of CuO at a reported value of 529.7 eV, defective Cu_2O at 531.6 eV, or the defective CuO value of 531 eV.

Figure 5.3.3 shows the Cu $2p_{3/2}$ spectra where two significant changes can be observed. One is the overall shifts of the main $2p_{3/2}$ peak from 932.3 eV (as-deposited) to 933.1 eV (523 K), 933.4 eV (573 K) and 933.6 eV (673 K), which also showed broaden peaks. These values seem to increase from reported literature average values of the binding energies of 932.4 eV belonging to Cu_2O to 933.6 eV of CuO, based on the NIST Database [13] as compiled by Biesinger[7]. However, the measured values might not be strictly accurate due to the possible erroneous correction of C 1s peaks. Another significant change is the emergence of the satellite peaks at approximately 941.5 eV and 944 eV for the annealed devices. These evident peaks are

well-known and belong to the characteristic shake-up satellites which indicate the presence of Cu(II) species, originating from the surface CuO layer.[14–20]

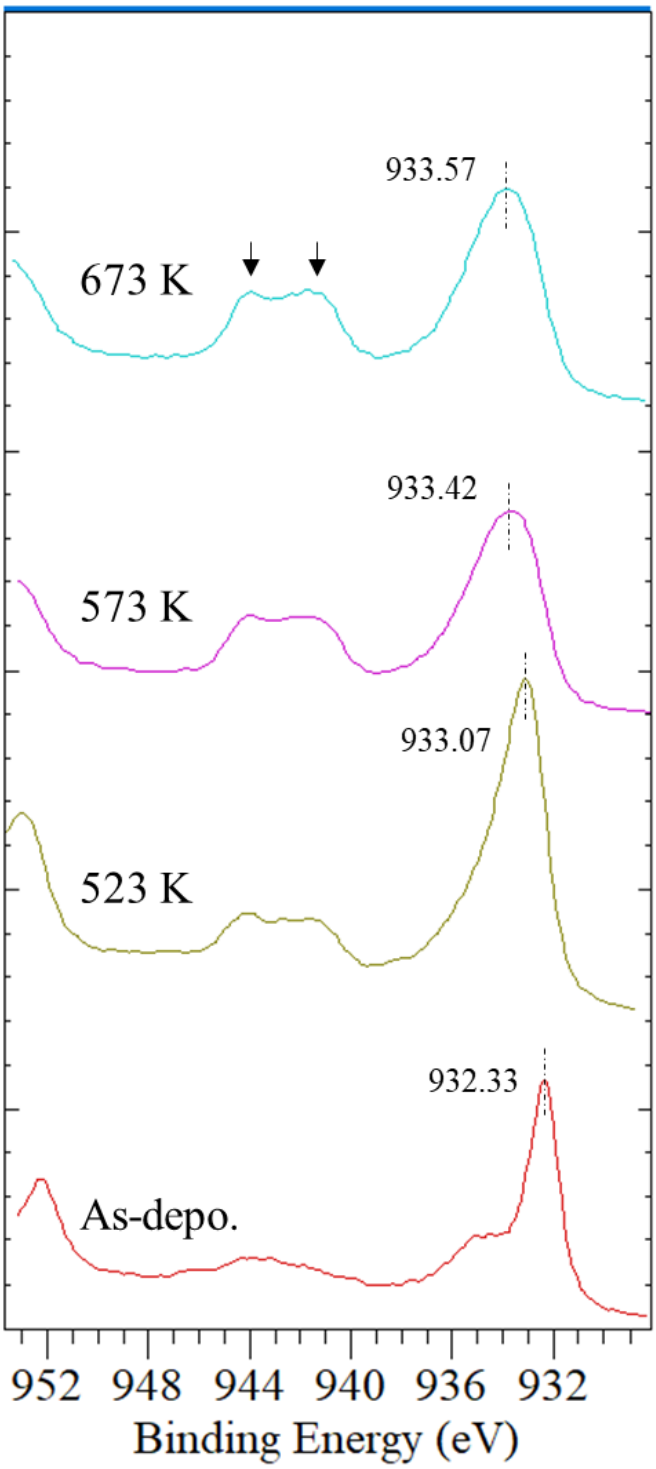

Figure 5.3.3. Cu $2p_{3/2}$ of as-deposited, 523 K, 573 K, and 673 K.

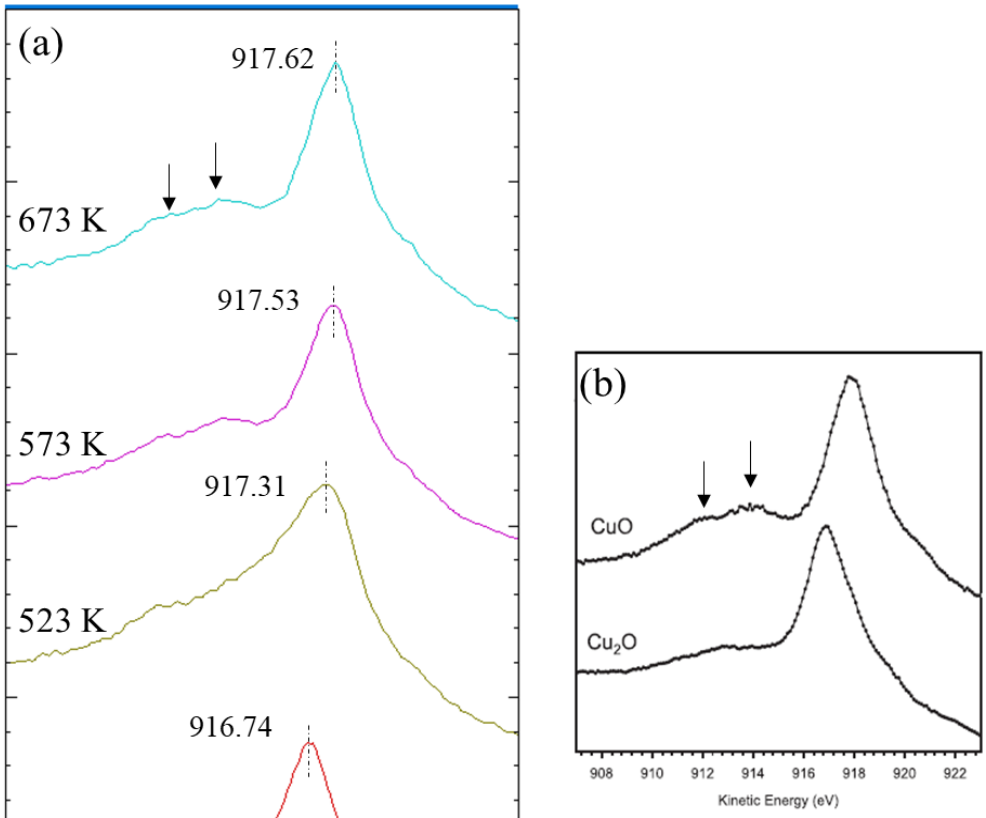

Figure 5.3.4. The Cu $L_3M_{4,5}M_{4,5}$ spectra of as-deposited, 523 K, 573 K, and 673 K and (b) reported line-shapes Cu $L_3M_{4,5}M_{4,5}$ spectra for Cu_2O and CuO.

Differentiation of species can also be made using the Cu $L_3M_{4,5}M_{4,5}$ Auger spectral line-shapes.[21] Although the Cu $L_3M_{4,5}M_{4,5}$ Auger main peaks of Cu(I) and Cu(II) species are close to each other, the shoulder peak at around 912-914 eV as shown as arrows in **Figure 5.3.4** are usually observed for the spectra of a CuO. For clarity, the reported spectral line shapes[7] was also shown in **Figure 5.3.4 (b)** as a comparison**.** The shift of the Cu $L_3M_{4,5}M_{4,5}$ Auger main peak can also be observed gradually shifting from 916.7 eV to 917.6 eV. The distinctive peak

in this spectra at 916.5 eV belonging to the Cu_2O was reported[22], corresponding to the as-deposited peak with 916.7 eV.

The results thus far have shown the XPS characteristics leaning to Cu_2O for the as-deposited layers and CuO for annealed layers, as expected. However, due to a possible error in the charge correction even after neutralizing, some measured values slightly differ from reported values.

Wagner has shown the chemical shifts for Auger transitions involving electrons in the atomic core and changing of the line shape for Auger transition involving valence electrons. He also introduced the concept of Auger parameter that was based on the ideas that the two line energies (Auger and photoelectron) of the same element in the same measurement is fixed, and charge corrections to individual peak measurements are unnecessary which can be canceled off, and the work function corrections are also not necessary, where vacuum level data can be compared to Fermi level data.[8,23,24] The Auger parameter α is defined as,

$$\alpha = E_k(C'C''C''') - E_k(C) \quad \textbf{(5.1)}$$

where $E_k(C'C''C''')$ is the kinetic energy of the Auger transition involving electrons from the C', C'' and C''' core levels, and $E_k(C)$ is the kinetic energy of the photoelectron from core level C. However, this equation might produce negative values, so a modified Auger parameter was redefined, with addition of the photon energy $h\upsilon$ to α, thus defining the modified Auger parameter α' as[25],

$$\alpha' = \alpha + h\upsilon = E_k(C'C''C''') + E_b(C) \quad \textbf{(5.2)}$$

Applying this method to assign the species was effective, as reported by Goh *et al.* in assigning Cu_2S and CuS[22], besides Poulston *et al.* who have used CuLMM and the Auger parameter to distinguish Cu(0), Cu(I) and Cu(II)[14].

In short, the Cu $2p_{3/2}$-$CuL_3M_{4,5}M_{4,5}$ respective values in binding energy and kinetic energy are summed up, which gives the value of the modified Auger parameter. The calculated values are summarized as **Table 5.1** below.

Table 5.1. Auger Parameter calculation of As deposited, 523 K, 573 K and 673 K layers

Sample	Binding energy Cu $2p_{3/2}$	Kinetic Energy (Cu $L_3M_{4,5}M_{4,5}$)	Auger Parameter
As-deposited	932.33	916.74	1849.07
523 K	933.07	917.31	1850.38
573 K	933.42	917.53	1850.95
673 K	933.57	917.62	1851.19

The literature average compiled values from the NIST database [13] are 1849.2 for Cu_2O and 1851.5 for CuO,[7,9] near to calculated Auger Parameter values of 1849.1 of as-deposited and 1851.2 of 673 K. A plot of the Cu $2p_{3/2}$-$CuL_3M_{4,5}M_{4,5}$ would then give the Wagner Plot (chemical state diagram) as shown in **Figure 5.3.5**.

Figure 5.3.5 (a) shows the Wagner Plot of literature and standard compounds of different Cu chemical states as reported by Biesinger,[7] and **(b)** the calculated values from this work of as-deposited, 523, 573 and 673 K-annealed layers. The horizontal axis is the binding energy (abscissa, oriented in the negative direction) and the vertical axis is the kinetic energy position of the sharpest core-core-core Auger peak, which in this case is the Cu $L_3M_{4,5}M_{4,5}$. The diagonal lines on the Wagner Plot are constant Auger Parameters α, which means values on the same line with having the same modified Auger Parameters α' as can be seen between the literature values and standard values reported by Biesinger in the CuO and Cu_2O ovals in **Figure 5.3.5(a)**. Positions of compounds on these plots indicate both relaxation energy and initial state effects,[8] and can give additional insight into the shift in electronic states between metal compounds. However, the topic is behind the scope of this investigation. Here, the distinguishability of chemical states of core-ionized atoms is discussed. As reported by Morreti

and Biesinger,[23,26] two distinct trends can be seen for compounds of different Cu chemical states, shown as two dotted ovals in **Figure 5.3.5(a)**. Compounds with a +2 oxidation number follow the slope of 1 (left dotted oval), while compounds with a +1 oxidation number are closer to the line with slope of 3 with similar binding energy values (right dotted oval). These are the respective distinct areas for the Cu(II) and Cu(I) compounds while metallic copper or Cu(0) is above these areas. [27] Comparison between **Figure 5.3.5(a)** and **(b)** then shows the chemical states of the experimental results. Clearly, the as-deposited layer (denoted with number 1) falls within the Cu(I) area, which in fact is very close to the literature and standard Cu_2O values. On the other hand, layers annealed at 523, 573 and 673 K fall within the Cu(II) area, which approaches the position of the reported CuO values with an increase of annealing temperature as seen in **(a)**. As such, from the Auger Parameters and Wagner Plot, it is concluded that while the as-deposited layer consists of purely Cu_2O, all annealed layers consist of topmost CuO layer, which agrees to results of the O 1s, Cu $2p_{3/2}$, and $CuL_3M_{4,5}M_{4,5}$ spectra.

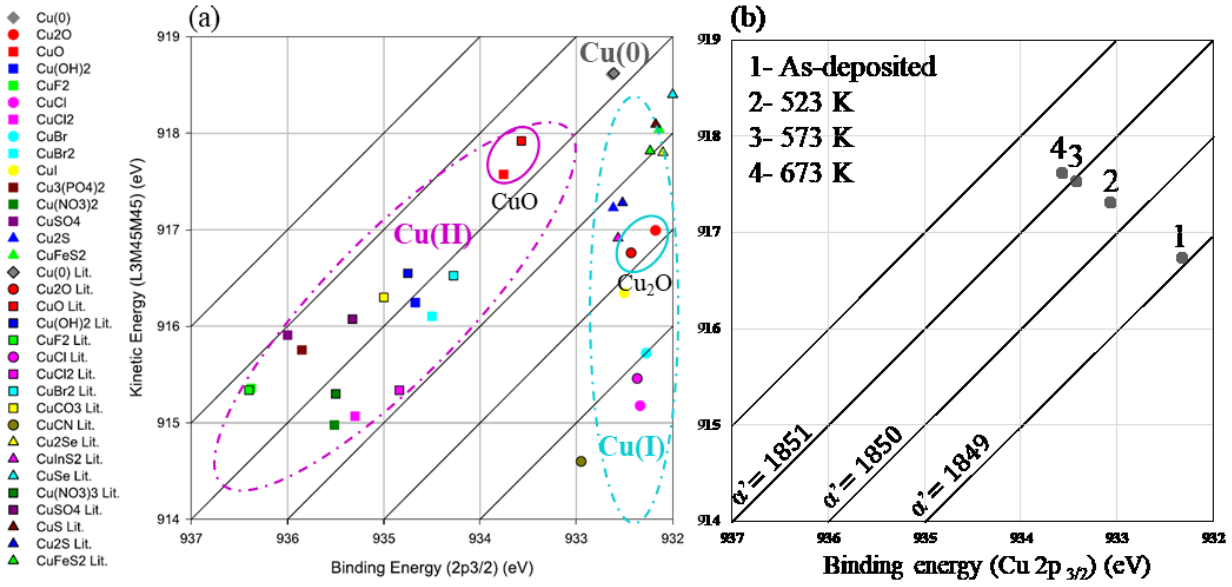

Figure 5.3.5. (a) The Wagner Plot of literature and standard compounds of different Cu chemical states as reported by Biesinger and (b) the as-deposited, 523 K, 573 K, and 673 K-annealed layers.

5.3.2 Band-alignment Calculation of Cu_2O/CuO

Valence band offset or VBO (denoted as ΔE_V) as shown in the following equation, is the difference in valence band maximums (VBM) of the Cu_2O and CuO layer, is crucial for drawing the band-alignment of the heterojunction.

$$\Delta E_V = E_{VBM}^{CuO} - E_{VBM}^{Cu2O} \quad \textbf{(5.3.1)}$$

However, the direct extraction of measurement of the VBM values may be inaccurate and can highly be affected by drifts and shift corrections. Kraut *et al.* proposed a method [5,28] that uses the core-level alignment and can prevent some measurement errors, giving an accurate band offsets measurements, since it does not rely on the shift correction. For our Cu_2O/CuO calculation, VBO (ΔE_V) is as shown in the following equation,

$$\Delta E_V = \left(E_{Cu\ 2p}^{CuO} - E_{Cu\ 2p}^{Cu2O}\right) + \left(E_{Cu\ 2p}^{Cu2O} - E_{VBM}^{Cu2O}\right) - \left(E_{Cu\ 2p}^{CuO} - E_{VBM}^{CuO}\right) \quad \textbf{(5.3.2)}$$

where $E_{Cu\ 2p}^{CuO}$ is the 2p main peak value of the surface CuO, $E_{Cu\ 2p}^{Cu2O}$ is the 2p main peak value of the underlying Cu_2O, $E_{Cu\ 2p}^{Cu2O}$ is the Cu 2p main peak value of the underlying Cu_2O, E_{VBM}^{Cu2O} is the measured VBM of the underlying Cu_2O, and E_{VBM}^{CuO} is the measured VBM of the surface CuO.

For this calculation, XPS measurements of the layers were made with sputtering every 18 seconds from the top surface until 180 seconds. The Cu 2p values are summarized in the following **Table 5.2.** If we observe the values after 18 seconds of sputtering for annealed layers and compare it to the surface values (0 seconds) or as-deposited values, we can observe that most of the CuO layer is sputtered away, since as reference, the reported Cu 2p main peak values of CuO is 933.6 and 932.4 eV[7]. Thus for the bandgap calculation of Cu_2O/CuO, the respective average values after 18 seconds are used as the $E_{Cu\ 2p}^{Cu2O}$ (Cu 2p main peak of the Cu_2O) values, which are 932.6, 932.4, and 932.6 eV for 523, 573, and 673 K respectively.

Table 5.2. The measured values for the Cu 2p main peaks binding energy for layers as-deposited, 523, 573, and 673 K.

	Sputter Time (s)	Cu 2p main peak Binding energy (eV)	
As Deposited	0	932.33	Cu_2O
	18	932.33	
	36	932.31	
	54	932.30	
	72	932.27	
	90	932.26	
	108	932.24	
	126	932.25	
	144	932.22	
	162	932.20	
	180	932.20	

	Sputter Time (s)	Cu 2p main peak Binding energy (eV)	
523 K	0	933.07	CuO
	18	932.57	Cu_2O
	36	932.59	
	54	932.60	
	72	932.61	
	90	932.60	
	108	932.60	
	126	932.61	
	144	932.61	
	162	932.62	
	180	932.64	

	Sputter Time (s)	Cu 2p main peak Binding energy (eV)	
573 K	0	933.54	CuO
	18	932.43	Cu_2O
	36	932.33	
	54	932.34	
	72	932.35	
	90	932.37	
	108	932.37	
	126	932.38	
	144	932.43	
	162	932.40	
	180	932.41	

	Sputter Time (s)	Cu 2p main peak Binding energy (eV)	
673 K	0	933.69	CuO
	18	932.66	Cu_2O
	36	932.64	
	54	932.65	
	72	932.67	
	90	932.72	
	108	932.62	
	126	932.62	
	144	932.57	
	162	932.55	
	180	932.54	

Also, the E_{VBM}^{Cu2O} values can be extracted from the measurement of VBM starting from 18 seconds onwards, as shown in **Figure 5.3.6.** Here, the E_{VBM}^{CuO} values are also shown at measurement ofthe 0 sec for the layers annealed at 523, 573 and 673 K, which are 0.47, 0.38, and 0.38 eV respectively. The E_{VBM}^{Cu2O} values are shown to be approximately 0.25 eV for 523 K while for 573 and 673 K the values are close to 0 eV.

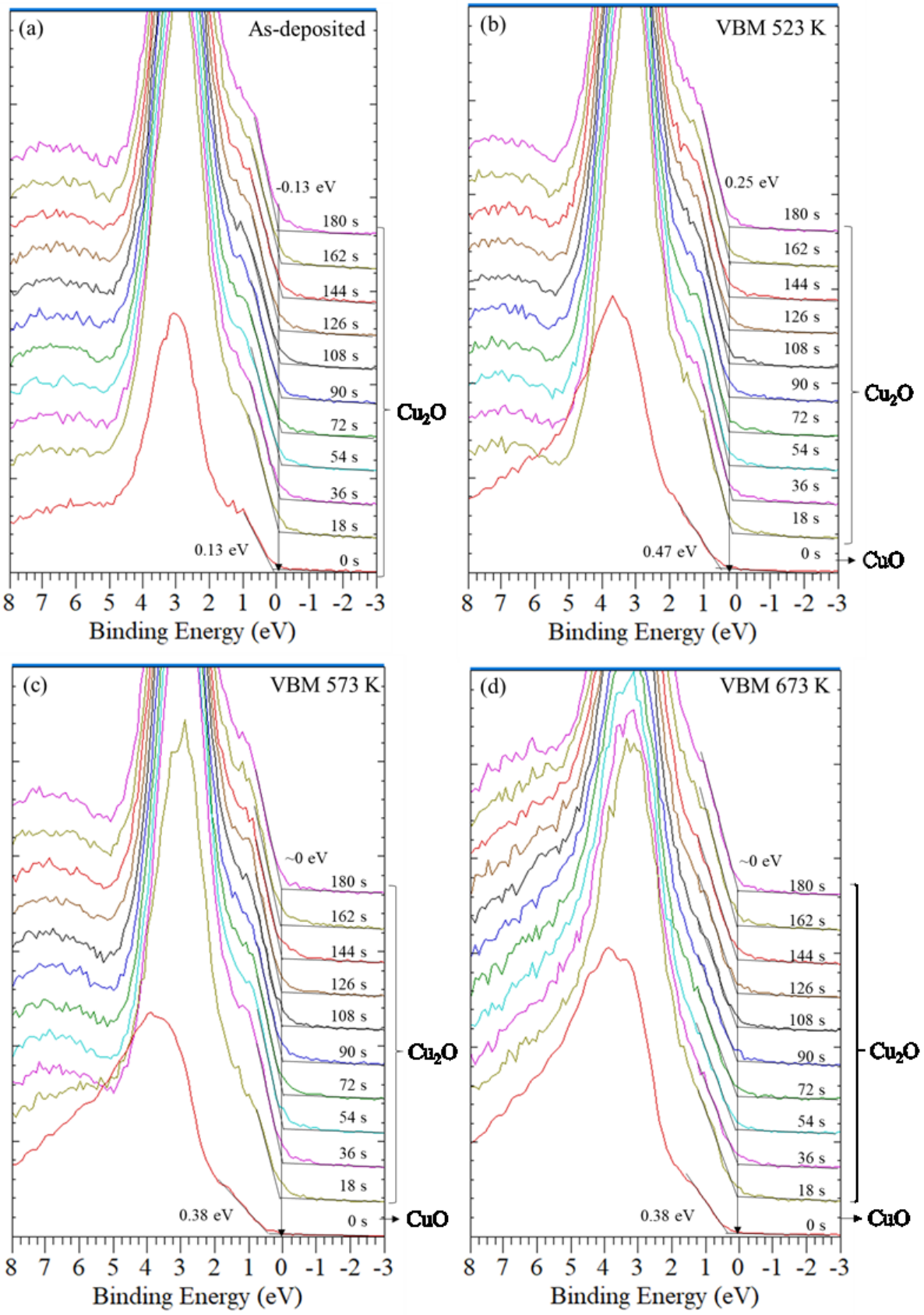

Figure 5.3.6 The measured values for the E_{VBM}^{Cu2O} and E_{VBM}^{CuO} values for 523, 573 and 673 K in (b), (c) and (d). The as-deposited values in (a) are for Cu_2O reference.

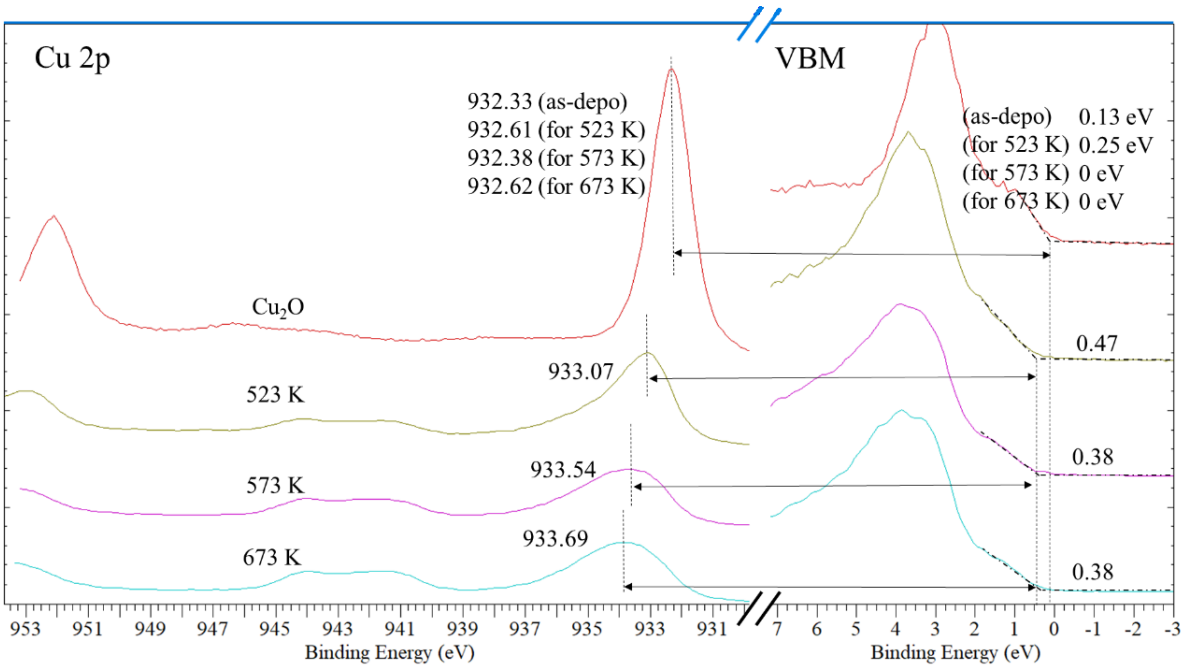

Figure 5.3.7. The XPS spectra showing all measurements needed to determine VBO for the layers as-deposited, 523 K, 573 K, and 673 K.

Finally, the summarized values needed for the VBO calculation are as shown in **Figure 5.3.7**. The VBO value for 523, 573 and 673 K are calculated to be 0.72, 0.38, and 0.38 eV according to **Equation 5.3.2**. To draw the schematic diagram, the estimated bandgap energies for Cu_2O and CuO from the Tauc plots are needed. The estimated direct bandgap of 2.1 eV for Cu_2O and the indirect bandgap of 1.47 eV for 637 K CuO are taken from Chapter 2 and 4, arriving at values of CBO of -0.09, 0.29 and 0.38 eV.

The schematic band alignment for Cu_2O/CuO based on the XPS data, VBO calculation and assuming the 673 K CuO indirect bandgap energy is as shown in **Figure 5.3.8** The CuO conduction band of 523 K-layer is 0.09 eV higher than the conduction band of Cu_2O, but this calculation is based on the bandgap energy of 1.47 eV calculated from the 637 K CuO layer, because the CuO layer of 523 K and 573 K were too thin and the absorbance was impossible to be detected. Here, we assume that the 673 K band alignment is most accurate.

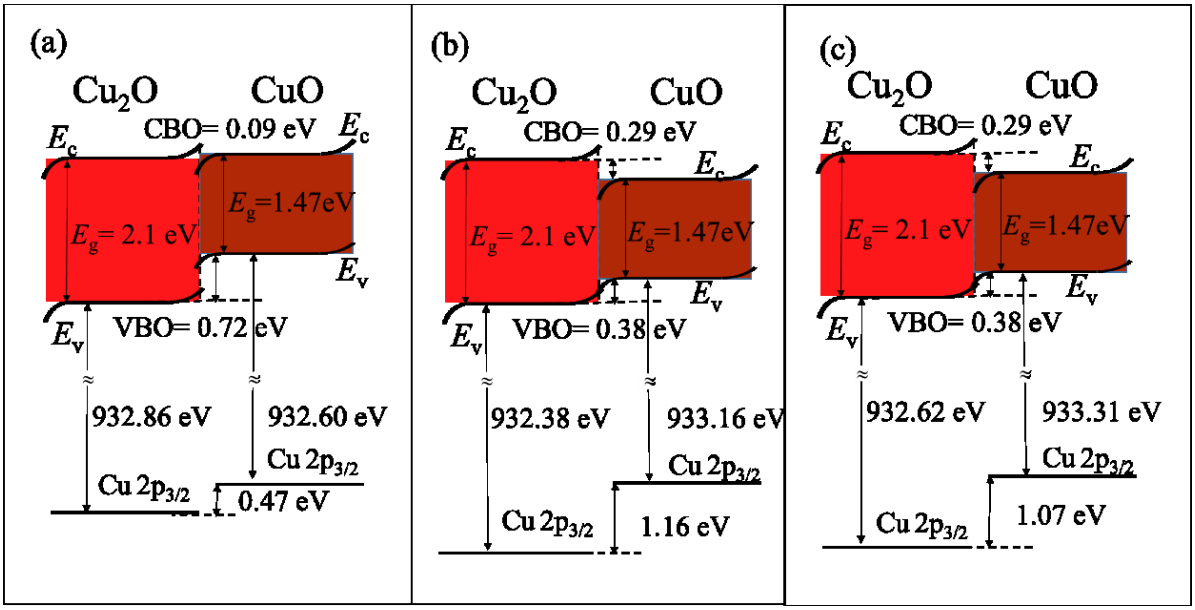

Figure 5.3.8. The schematic band alignment Cu_2O/CuO based on the calculated VBO and bandgap energy estimated from the Tauc plots. (a) is 523 K,(b) is 573 K and (c) 673 K.

As such, the EQE behavior for the Cu_2O/CuO layer prepared by heating at 523 K shown in Chapter 4 can be explained. A schematic band profile of the photoactive layers based on **Figure 5.3.8** is shown in **Figure 5.3.9** as reference diagram in an attempt to further comprehend the charge collection mechanism of the GZO/Cu_2O/CuO layer under reversed biased voltage.

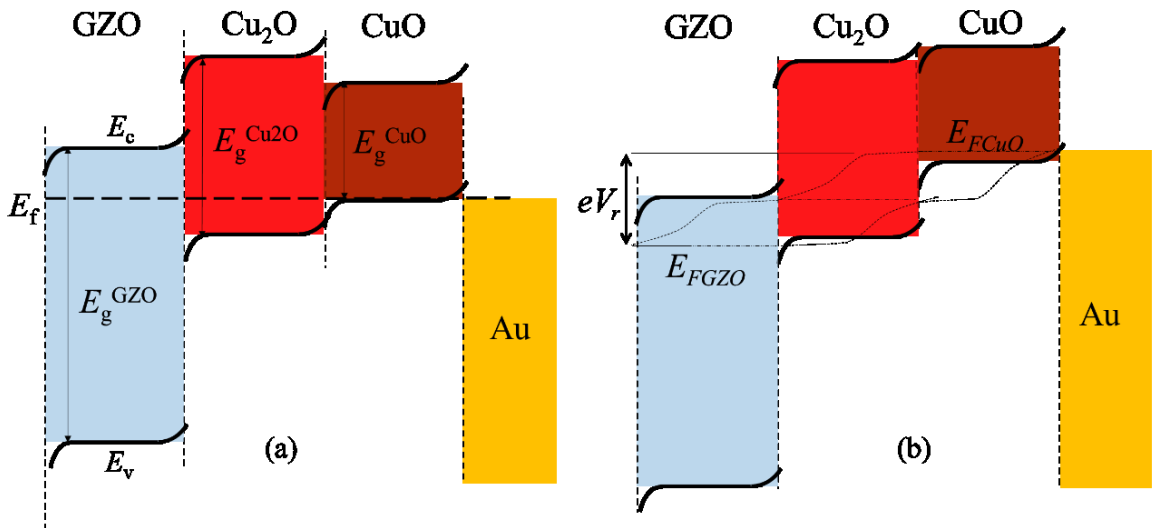

Figure 5.3.9. The schematic band alignment of GZO/Cu_2O/CuO based on the band-alignment calculations at equilibrium (a) and under reversed biased voltage (b).

Based on the schematic illustration in **Figure 5.3.9** the conduction band of the Cu_2O at equilibrium should appear elevated against both the GZO and CuO layers. Here, the flow of charge originating from the CuO layer towards the Au electrode is favorable instead of the opposite direction, which explains the behavior of dipping in EQE in the 500-nm region. However, under reversed biased, the potential across the heterojunction was increased, as denoted by eV_r, which exaggerated depiction is as shown in **Figure 5.3.9 (b)**. The depletion width and the peak electric field at the junction were also increased under this condition.[29] Consequently, along with the formation of quasi-Fermi levels, the band energy at the CuO side was relatively raised, facilitating movements of photo-induced electrons in the CuO layer towards the Cu_2O when irradiated and this should enable more charge collection via the GZO layer, which agrees with the EQE measurement.

The EQE spectrum is represented by the net effect of the charge collection by wavelengths. And it is known that the absorption edge of both Cu_2O and CuO layers are approximately 650 nm and 850 nm respectively in this photoactive device. Since the negative region of EQE measurement without biased voltage between 470 and 580 nm is within the overlapping region of absorption range for both light-absorbing layers, we can conclude that in this particular device annealed at 523K, the number of photo-induced electrons produced by the thin layer of CuO was more than that of the Cu_2O layer in this particular wavelength region. The appearance of the negative region is then largely dependent on the band alignment and condition of the Cu_2O thin film which affects the carrier mobility which further affects the charge collection. Thus, if the formation of CuO does not produce defect structures like pores that act as scattering defects in the Cu_2O layer, the overall EQE performances might be able to increase.

Also, according to this band diagram, a band alignment of GZO/CuO/Cu_2O might be more favorable for charge collection regarding this type of superstrate internally-stacked

photoactive layer, which might be able to collect charge even without reversed biased voltage applied. One other strategy to improve charge collection is to increase the bandgap energy of CuO to improve the CBO of the Cu_2O/CuO so that the conduction bands are properly aligned to facilitate the excited electrons' transportation towards the cathode. This, however, requires the need to be capable of fine-tuning the bandgap energy of the copper oxide semiconductors. Another strategy is to reduce the intermediate Cu_2O thickness to allow the possibility of tunneling effect of the photo-generated charge carriers in the CuO to flow through the Cu_2O bulk towards the cathode. However, reducing the Cu_2O thickness may lead to a decrease in light absorbance, and further study is needed.

5.4 Summary

The XPS evaluation was carried out in detail for chemical state determination of the layer surface for as-deposited Cu_2O, and CuO prepared by annealing at 523, 573 and 673 K. The characterization includes both the Cu(I) and Cu(II) species investigated through the O 1s, Cu $2p_{2/3}$, and the Cu $L_3M_{4,5}M_{4,5}$ spectras. The Auger parameters were also calculated, which showed a clear sign of the Cu species. The Wagner plot offered another clear picture of the distinction between the Cu species on the surface of as-deposited and annealed surfaces, and the results correspond to the XPS spectra measured. The fabrication of Cu_2O/CuO was reconfirmed by the XPS characterization, and the VBO for the 523, 573, and 673 K directly-stacked layers were calculated to be 0.72, 0.38 and 0.38 eV respectively. The band-alignment diagram shows the reason for the EQE behavior demonstrated in the previous chapter. The Cu_2O/CuO band alignment belongs to the straddling gap (type I), which explains the negative regions in EQE when charge originating from the CuO layer flow towards the electrode. Under reversed biased voltages, the increase in potential across the heterojunction facilitates movements of photo-induced electrons originating from the CuO layer towards the Cu_2O layer when irradiated, thus controlling the charge transport, resulting in an increase in the EQE and emergence of the CuO absorption edge at 850 nm. Strategies to improve charge collection was discussed and a more favorable alignment of GZO/CuO/Cu_2O was proposed.

REFERENCES

[1] J.P. Kim, E.S. Pak, T.E. Hong, J.S. Bae, M.G. Ha, J.S. Jin, E.D. Jeong, K.S. Hong, Electric properties and chemical bonding states of pn-junction p-CuO/n-Si by sol-gel method, J. Ceram. Process. Res. 13 (2012).

[2] R.E. Brandt, M. Young, H.H. Park, A. Dameron, D. Chua, Y.S. Lee, G. Teeter, R.G. Gordon, T. Buonassisi, Band offsets of n-type electron-selective contacts on cuprous oxide (Cu_2O) for photovoltaics, Appl. Phys. Lett. 105 (2014). doi:10.1063/1.4905180.

[3] I.J.T. Jensen, S. Gorantla, O.M. Løvvik, J. Gan, P.D. Nguyen, E. Monakhov, B.G. Svensson, A.E. Gunnæs, S. Diplas, Interface phenomena in magnetron sputtered Cu_2O/ZnO heterostructures, J. Phys. Condens. Matter. (2017). doi:10.1088/1361-648X/aa8799.

[4] M. Ichimura, Y. Song, Band alignment at the Cu_2O/ZnO heterojunction, Jpn. J. Appl. Phys. 50 (2011). doi:10.1143/JJAP.50.051002.

[5] L.M. Wong, S.Y. Chiam, J.Q. Huang, S.J. Wang, J.S. Pan, W.K. Chim, Growth of Cu_2O on Ga-doped ZnO and their interface energy alignment for thin film solar cells, J. Appl. Phys. 108 (2010). doi:10.1063/1.3465445.

[6] P.G. Keech, P. Vo, S. Ramamurthy, J. Chen, R. Jacklin, D.W. Shoesmith, Design and development of copper coatings for long term storage of used nuclear fuel, Corros. Eng. Sci. Technol. 49 (2014) 425–430. doi:10.1179/1743278214Y.0000000206.

[7] M.C. Biesinger, Advanced analysis of copper X-ray photoelectron spectra, Surf. Interface Anal. 49 (2017) 1325–1334. doi:10.1002/sia.6239.

[8] G. Moretti, Auger parameter and Wagner plot in the characterization of chemical states by X-ray photoelectron spectroscopy: A review, J. Electron Spectros. Relat. Phenomena. 95 (1998) 95–144. doi:10.1016/S0368-2048(98)00249-7.

[9] M.C. Biesinger, L.W.M. Lau, A.R. Gerson, R.S.C. Smart, Resolving surface chemical states in XPS analysis of first row transition metals, oxides and hydroxides: Sc, Ti, V, Cu and Zn, Appl. Surf. Sci. 257 (2010). doi:10.1016/j.apsusc.2010.10.051.

[10] D.J. Miller, M.C. Biesinger, N.S. McIntyre, Interactions of CO2and CO at fractional atmosphere pressures with iron and iron oxide surfaces: One possible mechanism for surface contamination?, Surf. Interface Anal. 33 (2002) 299–305. doi:10.1002/sia.1188.

[11] M.C. Biesinger, B.P. Payne, L.W.M. Lau, A. Gerson, R.S.C. Smart, X-ray photoelectron spectroscopic chemical state Quantification of mixed nickel metal, oxide and hydroxide systems, Surf. Interface Anal. 41 (2009) 324–332. doi:10.1002/sia.3026.

[12] H.A.. Hagelin-Weaver, J.F. Weaver, G.B. Hoflund, G.N. Salaita, Electron energy loss spectroscopic investigation of Ni metal and NiO before and after surface reduction by Ar+ bombardment, J. Electron Spectros. Relat. Phenomena. 134 (2004) 139–171. doi:10.1016/j.elspec.2003.10.002.

[13] C.D. Wagner, A.V. Naumkin, A. Kraut-Vass, J.W. Allison, C.J. Powell, J.R.J. Rumble, NIST Standard Reference Database 20 version 3.4, 2004. doi:Http:/Srdata.Nist.Gov/Xps/. Accessed February 17, 2016.

[14] S. Poulston, P.M. Parlett, P. Stone, M. Bowker, Surface Oxidation and Reduction of CuO and Cu_2O Studied Using XPS and XAES, Surf. Interface Anal. 24 (1996) 811–820. doi:10.1002/(SICI)1096-9918(199611)24:12<811::AID-SIA191>3.0.CO;2-Z.

[15] P. Velásquez, D. Leinen, J. Pascual, J.R. Ramos-Barrado, P. Grez, H. Gómez, R. Schrebler, R. Del Río, R. Córdova, A Chemical, Morphological, and Electrochemical (XPS, SEM/EDX, CV, and EIS) Analysis of Electrochemically Modified Electrode Surfaces of Natural Chalcopyrite (CuFeS 2) and Pyrite (FeS 2) in Alkaline Solutions, J. Phys. Chem. B. 109 (2005) 4977–4988. doi:10.1021/jp048273u.

[16] J.C. Otamiri, S.L.T. Andersson, A. Andersson, Ammoxidation of toluene by YBa2Cu3O6+xand copper oxides. Activity and XPS studies, Appl. Catal. 65 (1990) 159–174. doi:10.1016/S0166-9834(00)81595-X.

[17] P. Salvador, J.L.G. Fierro, J. Amador, C. Cascales, I. Rasines, XPS study of the dependence on stoichiometry and interaction with water of copper and oxygen valence states in the YBa2Cu3O7-xcompound, J. Solid State Chem. 81 (1989) 240–249. doi:10.1016/0022-4596(89)90011-X.

[18] F. Li, L. Zhang, D.G. Evans, X. Duan, Structure and surface chemistry of manganese-doped copper-based mixed metal oxides derived from layered double hydroxides, Colloids Surfaces A Physicochem. Eng. Asp. 244 (2004) 169–177. doi:10.1016/j.colsurfa.2004.06.022.

[19] L. Meda, G.F. Cerofolini, A decomposition procedure for the determination of copper oxidation states in Cu-zeolites by XPS, in: Surf. Interface Anal., 2004: pp. 756–759. doi:10.1002/sia.1757.

[20] D.N. Wang, A.C. Miller, M.R. Notis, XPS study of the oxidation behavior of the Cu3Sn intermetallic compound at low temperatures, Surf. Interface Anal. 24 (1996) 127–132. doi:10.1002/(SICI)1096-9918(199602)24:2<127::AID-SIA110>3.0.CO;2-Z.

[21] G. Deroubaix, P. Marcus, X-ray photoelectron spectroscopy analysis of copper and zinc oxides and sulphides, Surf. Interface Anal. 18 (1992) 39–46. doi:10.1002/sia.740180107.

[22] S.W. Goh, A.N. Buckley, R.N. Lamb, R.A. Rosenberg, D. Moran, The oxidation states of copper and iron in mineral sulfides, and the oxides formed on initial exposure of chalcopyrite and bornite to air, Geochim. Cosmochim. Acta. 70 (2006) 2210–2228. doi:10.1016/j.gca.2006.02.007.

[23] M. Satta, G. Moretti, Auger parameters and Wagner plots, J. Electron Spectros. Relat. Phenomena. 178–179 (2010) 123–127. doi:10.1016/j.elspec.2009.07.008.

[24] C.D. Wagner, X-ray photoelectron spectroscopy with x-ray photons of higher energy, J. Vac. Sci. Technol. 15 (1978) 518. doi:10.1116/1.569459.

[25] C.D. Wagner, L.H. Gale, R.H. Raymond, Two-dimesional Chemical State Plots: A Standardized Data Set For Use in Identifying Chemical States by X-ray Photoelectron Spectroscopy., Anal Chem. 51 (1979) 466–482. doi:10.1021/ac50040a005.

[26] G. Moretti, The Wagner plot and the Auger parameter as tools to separate initial- and final-state contributions in X-ray photoemission spectroscopy, Surf. Sci. 618 (2013) 3–11. doi:10.1016/j.susc.2013.09.009.

[27] M.W. Majeski, I.L. Bolotin, L. Hanley, Cluster beam deposition of Cu2-XS nanoparticles into organic thin films, ACS Appl. Mater. Interfaces. 6 (2014) 12901–12908. doi:10.1021/am5028428.

[28] E.A. Kraut, R.W. Grant, J.R. Waldrop, S.P. Kowalczyk, Precise determination of the valence-band edge in X-Ray photoemission spectra: Application to measurement of semiconductor interface potentials, Phys. Rev. Lett. 44 (1980) 1620–1623. doi:10.1103/PhysRevLett.44.1620.

[29] U.K. Mishra, J. Singh, Semiconductor device physics and design, 2008. doi:10.1007/978-1-4020-6481-4.

CHAPTER 6

Summary

6.1 Research Summary

This thesis is devoted to the studies on the copper oxides-based photovoltaic devices (PVs), which includes the Cu_2O, CuO and Cu_2O/CuO PVs prepared by electrochemical and low-temperature annealing. The main objectives of improving the PV by approaching from the EQE performances aspects was investigated thoroughly and reported.

In **Chapter 2**, the fabrication of Cu_2O-PV (GZO/ZnO/Cu_2O) was carried out, based on past reports, and the effects of annealing the device in vacuum were investigated.

Characterization includes external quantum efficiency (EQE) measurement, *J-V* measurement, X-ray diffraction analysis, FESEM observation, UV-vis measurement, and Hall measurement. The successful fabrication showed approximately 80% EQE and PV performances of 0.72% power conversion efficiency (PCE). A significant increase in maximum EQE values of to nearly 100% was reported for the sample annealed at 423 K in vacuum, which led to a dramatic increase in short-circuit current density (J_{SC}) to 5.4 mA cm^{-2} and the PCE to 0.89%. The mechanism of the improvement by annealing in vacuum was further investigated and elucidated. When annealed below 473 K., higher carrier mobility was achieved due to the lessened scattering defects that hinder carrier transportation. The increased carrier mobility, as evidenced by the Hall measurement, meant increased diffusion coefficient and consequently led to a longer diffusion length. A long diffusion length is directly related to the heightened J_{SC}, which is also reflected in the improved EQE evaluation. The microstructural evidence observed in the FESEM showed the formation of pores at excessive temperatures higher than 473 K, which led to the deterioration of the evaluations. Factors such as annealing atmosphere (oxygen partial pressure), initial grain size, and substrate that affects the resulting microstructural changes proved to be very important in determining the optimum annealing temperature, explaining the discrepancy of past reported results. Nonetheless, annealing proves to be a facile, effective method to increase the PV performance of the electrochemically prepared Cu_2O-based PV.

In **Chapter 3**, the fabrication of CuO-PV (Al/polysiloxane/CuO/Au) was investigated to demonstrate the capabilities of CuO to perform as a light-absorbing layer and a photovoltaic device. A comparison was made with and without the buffer layer of polysiloxane, which showed that without it, the device showed ohmic behavior without any photocurrent density observed. With the polysiloxane, the electrical characteristics were demonstrated when the carrier was transported through the polysiloxane by tunneling effect. The PV performance showed open-circuit voltage (V_{OC}), J_{SC}, and Fill factor (*FF*) estimated to be 0.24 V, 0.067 μA

cm^{-2}, and 0.29, respectively. The conversion efficiency was calculated to be $4.6x10^{-7}$%. The V_{OC} value was much larger than 0.28 mV reported for the electrodeposited CuO-PV-device and slightly lower than 0.37 V for the thermally-prepared CuO/ZnO-PV-device. This demonstrates that the CuO layer, although the performance has rooms to be improved, can function as a light-absorbing layer in photovoltaics and photoelectrochemical applications.

In **Chapter 4**, the fabrication of directly stacked Cu_2O/CuO photoactive layer (GZO/Cu_2O/CuO) was investigated as a strategy to combine both copper oxide as a light-absorbing layer, and the PV performance was evaluated by EQE. The EQE of the internally-stacked Cu_2O/CuO layers and their changes under different low reversed biased voltage was demonstrated. The EQE result clearly demonstrates that both oxide layers acted as the light-absorbing layer, and showed the validity of copper-oxide-based photoactive layer in terms of augmented absorption span due to the incorporation of different bandgap energies of the copper oxides. For the 673 K sample, more photo-induced electrons produced in the CuO layer were being swept towards the source of irradiation under low reversed biased voltage, which resulted in a dramatic increase in the 550-nm-peak and the appearance of the CuO absorption edge at 840 nm. The results also highlight the importance of the semiconductor condition of the layers with minimal defects to realize a high-performing photoactive layer.

In **Chapter 5**, the need to further investigate the characterization of the directly stacked Cu_2O/CuO arose with the reported EQE behavior in the previous chapter. XPS evaluation was carried out in detail, and the characterization including both the Cu(I) and Cu(II) species investigated through the O 1s, Cu $2p_{2/3}$, and the Cu $L_3M_{4,5}M_{4,5}$ spectras which was impossible with XRD alone. The Auger parameter was also calculated and the Wagner plot offered a clear picture of the changes and distinction between the Cu species on the surface of as-deposited and annealed surfaces. The fabrication of Cu_2O/CuO was reconfirmed by the XPS characterization, and the VBO for the 673 K sample was calculated to be 0.38 eV and the CBO

to be 0.29 eV. The band-alignment diagram showed the reason for the EQE behavior demonstrated in the previous chapter, and a preferable alignment of GZO/CuO/Cu_2O was proposed.

This work has demonstrated the viability of incorporating both Cu_2O and CuO as the light absorbing layer to enhance EQE performance. This work also has demonstrated that low-temperature annealing treatment can improve electrochemically-prepared Cu_2O-based PV, as long as phase transition does not occur which can lead to the formation of defects such as pores in the lattice. The performances of CuO-based PV can be further improved by the insertion of the buffer layer, and also it is important to limit the surface irregularities of the heterojunction. With reversed biased voltage is applied, the directly stacked Cu_2O/CuO showed EQE performances with an extended absorption edge. The importance of the biased voltage and the effect of the biased voltage on the directly-stacked Cu_2O/CuO was explained by the band-alignment investigated in detail. By implementing the preferable band alignment proposed, and an improved PV performance can be anticipated, which give insights in designing future copper oxide based PVs. In short, this study contributes to identifying the important elements of fabricating a high-quality Cu_2O-layer such as elucidating the mechanism low-temperature annealing, demonstrated the viability of a buffer layer and importance of the heterointerface condition for CuO-PV, and showed the mechanism and implications of applied biased voltage on Cu_2O/CuO layer. These will ease and facilitate further improvements towards realizing a next-generation ultra-low cost and environment-friendly thin film copper oxide PV applications in future researches.

6.2 Acknowledgement

This thesis is the outcome of my research from April 2016 until March 2019 at Thin Film Laboratory, Department of Mechanical Engineering, Toyohashi University of Technology, Japan under the supervision of Prof. Dr. Masanobu Izaki.

This thesis would not have been possible without, first and foremost, the guidance of my supervisor Prof. Dr. Masanobu Izaki. He is not only an excellent supervisor but is also always very compassionate and kind towards us. Under influence of his vast knowledge, I was taught about material science, semiconductors, and its solid state physics. Not only that, I am truly grateful that he trained me to conduct research and write academic papers. Anybody would be impressed by his visions and thinking, which deep enthusiasm highly affected me. One would expect the life of a Ph.D. student to be low-keyed and restrained, which is not at all the case under the supervision of Prof. Izaki. He gives freedom to explore and attempt new ideas, at the same time give appropriate pushes on the back. I would like to also express my utmost appreciation for the many given invaluable chances to experience meaningful international conferences and experiment sessions in Spring-8, Japan.

I would also give my special thanks to my examiners, Prof. Dr. Masahiro Fukumoto, Prof. Dr. Yoshikazu Todaka, Prof. Dr. Masakazu Kobayashi who took time off their busy schedules.

Next, I would like to express my gratitude to Assc. Prof. Dr. Seiji Yokoyama and Dr. Junji Sasano for their kind comments and ideas especially during discussion sessions in the laboratory seminars, which helped to shape the reasoning of my researches. I would also like to express a special thanks to Prof. Dr. Tsutomu Shinagawa from Osaka Municipal Technical Research Institute, for his guidance in the measurements of my first FESEM observations and the Hall measurement, and finally the writing of my first published paper.

Another thing I feel deep gratitude for is that Thin Film Laboratory boasts exceptional students as lab members. Mr. Koyama, Mr. Satou, Mr. Fukuzawa, Mr. Kikkawa, Mr. Nozaki,

and Ms. Aye were extremely helpful in discussions, and when conducting experiments together. Without them, it was impossible to gain progress on the research. Their cooperation was a great motivation for me.

I would like to thank the Toyohashi University of Technology for offering the scholarship and research assistant post which provided me more time with my research.

I would also like to thank my family and all my relatives in Malaysia, and especially my parents who still works diligently after the retiring age to support my studies here in Japan, who gave full support to me to continue the PhD course, and who from time to time gave me the mental supports when I needed them most. I would also convey my gratitude to Ms. Jocelyn for her support throughout the preparation and writing of my thesis for her kindness and patience.

Finally, I would like to thank everybody who played an important part in realizing this thesis, and at the same time express my apology for not being to mention personally name by name.

Toyohashi, Japan

March 2019

Pei Loon Khoo

6.3 Research Achievements

6.3.1 List of Publications

[1] Pei Loon Khoo, Yuuki Kikkawa, Kenta Satou, Tsutomu Shinagawa, and Masanobu Izaki. "Improvements in External Quantum Efficiency of Electrochemically constructed n-ZnO/p-Cu_2O Photovoltaic Devices by Rapid Thermal Annealing", Thin Solid Films, 653, 158-164, 2018.

[2] Pei Loon Khoo, Miho Nagai, Mitsuru Watanabe, and Masanobu Izaki. "Electrodeposited CuO Photovoltaic Device with Polysiloxane Layer", J. Surf. Finish. Soc. Jpn. 69, 469-471, 2018.

[3] Pei Loon Khoo, Yuuki Kikkawa, Tsutomu Shinagawa, and Masanobu Izaki. "Effects on external quantum efficiency of electrochemically constructed n-ZnO/p-Cu_2O photovoltaic device by annealing", AIP Conference Proceedings **1865**, 050005 (2017)

[4] Pei Loon Khoo, Kenta Satou, Kota Nozaki and Masanobu Izaki. "External Quantum Efficiency of Electrochemically Prepared and Annealed Directly Stacked SLG/GZO/Cu_2O/CuO Photoactive Layer", J. Phys. Conf. Ser. 1083, 12030 (2018)

6.3.2 List of Conferences

[1] Internally Stacked Cu_2O/CuO Photovoltaic Layer with Expanded Absorption Band, Pei Loon Khoo, Kazuma Fukasawa, Naoki Yamashiro, Masakazu Kobayashi, and Masanobu Izaki., Presentation No: E.IX.3 European Materials Research Society International Conference, Strasbourg, France, 2017.

[2] Effects on external quantum efficiency of electrochemically constructed n-ZnO/p-Cu_2O photovoltaic device by annealing. Pei Loon Khoo, Yuuki Kikkawa, Tsutomu Shinagawa, and Masanobu Izaki, 3rd International Conference of Global Network For Innovative Technology 2016 (IGNITE 2016), Penang, Malaysia.

[3] External Quantum Efficiency of Electrochemically Prepared and Annealed Directly Stacked Cu_2O/CuO Photoactive Layer, Pei Loon Khoo, Kenta Satou, Kota Nozaki, and Masanobu Izaki, 6th International Conference On Solid State Science And Technology (ICSSST2017), Penang, Malaysia.